Faculdade De Engenharia Da Universidade Do Porto

A wearable mechanism to assist the knee during the loading response

Luís Rodrigues de Castro

Dissertation

MSc in Mechanical Engineering

Supervisor: Dr. Vito Monaco, SSSA (Pisa, Italy)

Co-Supervisor: Prof. Mário Vaz, FEUP (Porto, Portugal)

October 1, 2018

Abstract

Exoskeletons are assistive devices that have been evolving in the last years, being mostly applied in the military, rehabilitation and ergonomics fields. In addition, they are also being used to increase the human endurance capabilities, by reducing the muscle fatigue and metabolic rate. The aim of this thesis was, in fact, to study a new design for a wearable and passive mechanism that solves those last aspects. In particular, the mechanism is intended to assist the knee during the loading phase of the human gait cycle. The state of art of such passive assistance is typically based on the use of springs (that store and release energy), while, here, a damping-based device was designed, being the damper mechanism responsible for dissipating energy. Moreover, the spring approach does not allow for an easy individual adaptability, as springs must be replaced. In contrast, the damper solution includes a regulator screw, facilitating customization.

Two different solutions were thought and analyzed: a pneumatic one, and another based on a commercial damper. Only the last was further studied due to its higher potential of success.

Before conceptualizing any device, it was necessary to analyze kinetic and kinematic data of the human gait, available in the literature. This data was used to estimate the required damping coefficient of the system, so it could mimic the human knee joint.

Regarding the pneumatic solution, it was, first, designed as a pneumatic spring (stroke of 100mm and initial pressure of 6.9bar) and, afterwards, a simulation using *Simulink* was used to test the influence of the flow control valve. The simulation showed that the system provided a similar torque to the one produced by the muscles which support the knee. Although these results were promising, the system was not further investigated, due to possible leaks of air and overweight.

For the other solution, a commercial rotary damper was selected, with 40Nm of maximum torque and low weight (352g). However, its damping characteristics had to be determined experimentally, as no complete datasheet was available. From the mathematical model obtained (damping coefficient as a negative exponential function of the angular velocity), it was concluded that the damper does not provide a similar torque to the knee one. Nevertheless, it can bring energetic reductions, only evaluated with future additional tests. Moreover, the mechanical components, and relevant electronic components, were selected. A 3D model was built in *Solidworks* and used to explain the device operation.

Acknowledgments

I would like to thank Dr. Vito Monaco not only for giving me the opportunity to work in such a prestige university and interesting project, but also for the enormous support given throughout my work. I also thank prof. Mário Vaz for his guidance in spite of the distance imposed by the project location. Finally, I have to give my best thanks to my family and girlfriend, Débora Pereira, for their constant support, both intellectually and emotionally, throughout the thesis.

Contents

List of Figures

List of Tables

Abbreviations and Symbols

Dof	Degrees of freedom
P_{Knee}	Knee power
M_{Knee}	Knee Moment
ω_{Knee}	Knee angular velocity
GC	Gait cycle
MIT	Massachusetts Institute of Technology
L	Flow control Valve
R	Flow control Valve
R^2	Coefficient of determination
$\dot{\theta}_i$	Knee angular velocity at time i
θ_{i+1}	Knee angle at time *i+1*
θ_i	Knee angle at time i
t_{i+1}	Time sample *i+1*
t_i	Time sample i
C_i	Knee damping coefficient at time i
τ_i	Knee moment of force at time i
P_{begin}	Point when K1 begins
$P_{inversion}$	Point of inversion of motion during K1
P_{ending}	Point when K1 ends
E_{K1}	Energy of knee joint in K1
W_{Knee}	Knee power profile
C_{Damper}	Damping coefficient estimation
UFRV	Unidirectional flow restrictor valve
NC	Normally closed
P_2	Pressure in the compression chamber
P_i	Initial pressure in the compression chamber
Lic	Initial length of compression chamber
Lc	Length of compression chamber
Lie	Initial length of expansion chamber
Le Le	Length of expansion chamber
γ	Adiabatic constant

XK	Distance from the fixation point in the thigh to the knee joint
Xs	Distance from the fixation point in the shank to the knee joint
La	length between the two fixation points of the device
θ_k	Generic knee angle
$\theta_k Max$	Considered maximum knee angle
St_A	Actuator stroke
D_{ext}	Outer diameter of the actuator's chamber
D_{rod}	Inner diameter of the actuator's chamber
B_j	Lever arm of pneumatic actuator
A_{eft}	Effective chamber area
D_{rod}	Rod diameter of the actuator
A_{max}	Maximum area of the flow control valve
A_{def}	Default area of the flow control valve
D_{Max}	Actuator hole port diameter
C_d	Coefficient of discharge
Ma	Mach number
T_0	Initial chamber temperature
A_{val}	Flow control valve area
R	Gas constant of air
D	Flow valve control diameter
$S_d MT$	Safety coefficient of the maximum damper holding torque
E_{reso}	Encoder angular resolution
G_{ratio}	Planetary gear ratio
V_{out}	motor output velocity
C_{damp}	Calculated damping coefficient
T_{sens}	Torque obtained by the sensor
N_t	Number of turns of the damper regulator
V	damper angular velocity
η	Clutch engagement fraction
w_c	Tooth width
d_c	Tooth depth
h_c	Tooth height
n_c	Number of teeth
$r_{i,c}$	Clutch inner radius
$\sigma_{y,AL}$	yield strength of AA2011 T3 aluminum allow
$T_{c,max}$	Maximum clutch holding torque
T_{DMAx}	Solution 2 maximum damper holding
d_{ber}	Inner diameter of bearing

C_{ber}	Dynamic basic load rating
B_{ber}	Bearing width
D_{ber}	Outer diameter of bearing
$C0$	Static basic load rating
Pu	Fatigue load limit
F_{Fbolt}	Tangential force on the bolts
n_{Bolt}	Number of bolts
B_{bolt}	Distance from the bolt hole to the shaft's axis
F_{Nbolt}	Normal bolt force
μ_{Al}	Static friction coefficient of Al-Al contant
σ_{Bolt}	Traction tension in the bolt
A_{Rbolt}	Bolt resistance area
D_{Bolt}	Bolt nominal diameter
P_{Bolt}	Bolt pitch
M_{bolt}	Applied torque to the bolt
S_{Fbolt}	Bolt safety factor
$\dot{\theta_{enc}}$	Encoder's angular velocity
θ_{enc}	angle reed from the encoder
θ_{MAX}	threshold angle
t_{act}	activation time of the solenoid
t_{state}	maximum time one state can be activated
θ_k	knee angle at time sample k
$Clutch_{Resolution}$	Clutch angular resolution
t_{cross}	timing for the solenoid activation
Δ	time interval between the predicted hell strike and the actual event
K_{damp}	Return spring stifness
J	Damper moment of inertia
C_{ret}	Damping coefficient in passive direction
T_{ext}	Exterior torque applied to the damper
T_{reset}	Reset time for return spring
T	Constante of time
T_{TorMax}	Maximum torque held by the torsional spring
K_b	stress concentration factor of spring wire
D_{spr}	Mean spring diameter
d_{spr}	Spring diamter
N_{tSpr}	NUmber of spring turns
E_{spr}	Spring Modulus of young

$S_{bending}$	Maximum bending stress
K_{ts}	Stress concentration factor of grooved shaft
t	Groove depth
$D_{S,Out}$	Outer shaft diameter
R^*	Groove fillet radius
$\tau_{y,Al}$	Aluminum shear strength
τ_{nom}	Nominal shear stress
$\tau_{ins,Es}$	Installed shear stress
$S_{f,Es}$	Safety coefficient of the return spring grooves
K1	Negative region during loading response
K2	Positive region during mid stance
K3	Negative region during initial and mid swing
K4	Negative region during late swing

1. Introduction

1.1 Context and Motivation

Walking is an everyday action that most of us execute without much thought. However, much of the underlying knowledge is still not well understood especially when it comes to energy expenditures and efficiency. Such losses occur mainly due to muscle contraction, responsible for both dissipating and inserting mechanical energy into the walking motion. In particular, while walking, the loading response requires a high muscle activation and, consequently, a great metabolic cost. In that line of thought, it would be interesting/useful to investigate the application of a passive device for the knee, capable of dissipating the energy during the loading response. Other big step regarding this topic is, then, to transpose this concept to a modular device that can be implemented not only in the knee, but other joints (mainly ankle and hip).

1.2 Thesis Goals

The main goal of this thesis is to design a device able to actuate during the loading phase of the gait cycle and dissipate part of the energy that, otherwise, would be wasted by the extensor knee muscles. This decrease of the extensor muscles' activity will reduce the energy activation and, consequently, lower the metabolic cost of locomotion.

The device shall:

1. Recognize the normal gait cycle events and actuate according to it;
2. Have some adaptability according to the weight and leg length of each user (main variables responsible for inter-subject variability);
3. Have a low power consumption;
4. Be as cheap as possible;
5. Be as light as possible (preferably less than 500g).

An iterative process was adopted, and two solutions were thought: first, a pneumatic solution, which was then abandoned due to reasons explained in chapter 6; the second uses a rotary damper as the dissipating element, and, as it had a higher potential of success, it was further developed - see chapter 7. Characterizing both solution in terms of the technology readiness level, the first concept is in the first level and the last one on the second level. [31]

2. Physiology of human walking

2.1 Degrees of freedom of the human lower limb

The human leg can be thought as a structure with 7 Degrees of Freedom (Dof), three in the hip, one in the knee and other three in the ankle. In figure 2.1 a) and b) the human anatomic planes and a kinematic model of the human leg in the sagital plane (dominant one during locomotion) are shown respectively. Only the Knee joint DoF is of interest being characterized by extension (Shank moves away from thigh) and flexion (Shank gets closer to the thigh).

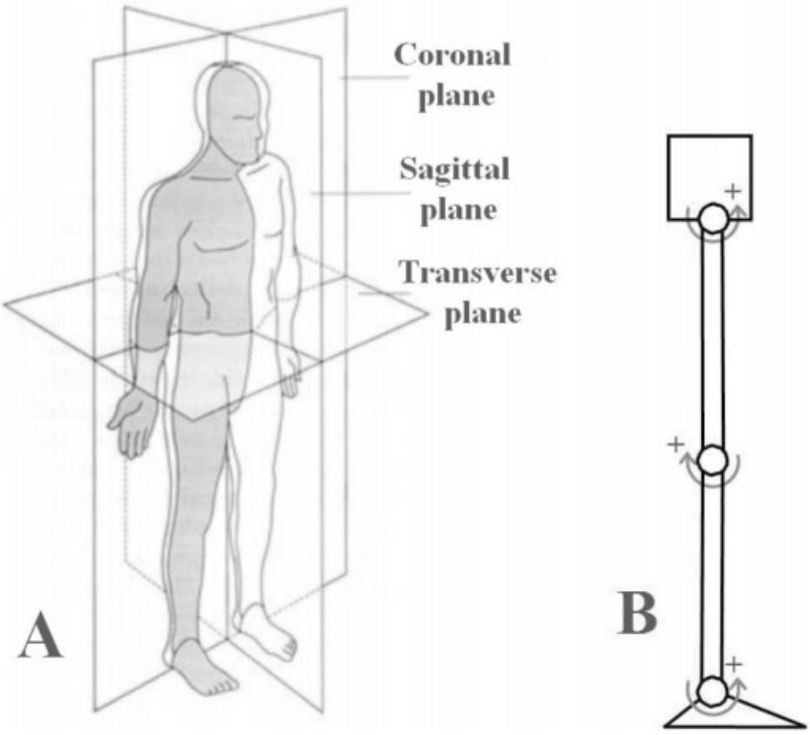

Figure 2.1: A) Anatomical planes description. B) Leg diagram in the rest position (0 deg at all joints) with the positive direction indicated. [6]

2.2 The Gait Cycle

Gait cycle can be defined as a sequence of lower-limb events occurring during normal walking (on flat, level surface) and made up of alternating stance phase (where all or part of foot contacts the support surface) and swing phase (when limb swings forward between the end of one ground contact and start of next). [34]

For a better understanding of the gait cycle and his division some definitions must be given first: [34]

- Step: Sequence of movements that starts with the initial contact of one foot and end with initial contact of the contralateral foot.
- Stride: Sequence of movements that starts and finishes with consecutives initial contacts of the same foot. So a stride is made of two subsequent steps.
- Stance phase: Represent the total period during which the foot is in contact with the ground and begins with the initial contact (generally by the heel). Accounts for 60% of the gait cycle.
- Swing phase: The swing in the other end begins as the foot is lifted from the ground (toe-off) and finishes right before initial contact. Usually makes up for 40% of the full gait cycle.
- Double support phase: Phase where the body weight is supported by both limbs. During the gait there are two double stance phases each one lasting 10-15% so all of them account for 20-30% of the gait cycle.
- Single support: Opposite to the other phase, in this, one all body weight is supported by one limb only, and represents 70-80% of the gait cycle

Figure 2.2 syntheses all the gait phases highlighting the main events in each.

Gait phases	IC Initial Contact	LR Loading Response	MST Mid Stance	TST Terminal Stance	PSW Pre Swing	ISW Initial Swing	MSW Mid Swing	TSW Terminal Swing
Gait cycle	0 %	0 – 12 %	12 – 31 %	31 – 50 %	50 – 62 %	62 – 75 %	75 – 87 %	87 – 100 %
Hip	20° flexion	20° flexion	0° flexion	-20° hyperextension	-10° hyperextension	15° flexion	25° flexion	20° flexion
Knee	0° – 5° flexion	20° flexion	0° – 5° flexion	0° – 5° flexion	40° flexion	60° – 70° flexion	25° flexion	0° – 5° flexion
Ankle joint	0°	5° – 10° plantar flexion	5° dorsal flexion	10° dorsal flexion	15° plantar flexion	5° plantar flexion	0°	0°
Muscle activity	M. quadriceps femoris M. tibialis anterior M. gluteus medius M. gluteus maximus Ischiocrurale Muskulatur	M. quadriceps femoris M. tibialis anterior M. gluteus medius M. gluteus maximus M. adductor Magnus M. tensor fascia latae M. tibialis posterior M. peroneus longus	M. gastrocnemius M. soleus	M. soleus M. gastrocnemius M. flexor digitorum longus M. flexor hallucis longus M. tibialis posterior M. peroneus longus M. peroneus brevis	M. soleus M. gastrocnemius M. rectus femoris M. adductor longus	M. extensor hallucis longus M. flexor hallucis longus M. sartorius M. iliacus M. tibialis anterior	M. semimembranosus M. semitendinosus M. biceps femoris M. tibialis anterior	M. quadriceps femoris M. semitendinosus M. semimembranosus M. biceps femoris M. tibialis anterior
Functions	• heel contact to the ground	• shock absorption in knee and ankle joint • load transmission and stability in the hip • forward motion by heel rocker	• controlled forward motion of the tibia • shifting of the gravity centre to the front by ankle rocker	• controlled dorsal extension at the ankle joint with lifting the heel from the ground	• passive knee joint flexion of 40° • plantar flexion of the ankle joint	• min. 55° knee flexion for sufficient ground clearance	• increasing hip flexion to 25° • dorsal extension of the ankle joint to neutral-zero-position	• knee joint extension to neutral-flexion • preparation for stance phase

Figure 2.2: Summary of the gait phases, pointing their main features. [40].

2.3 Kinematics and Kinetics of Walking

The following section will provide a brief description regarding the knee joint motion, moment of force and power patterns. The motion is defined as the relative angle between the thigh and shank, and the power as:

$$P_{Knee} = M_{Knee}\omega_{Knee} \tag{2.1}$$

where M_{Knee} is the knee moment and ω_{Knee} the angular velocity.

As an example of kinematic and kinetic knee profiles, figure 2.3 is presented.

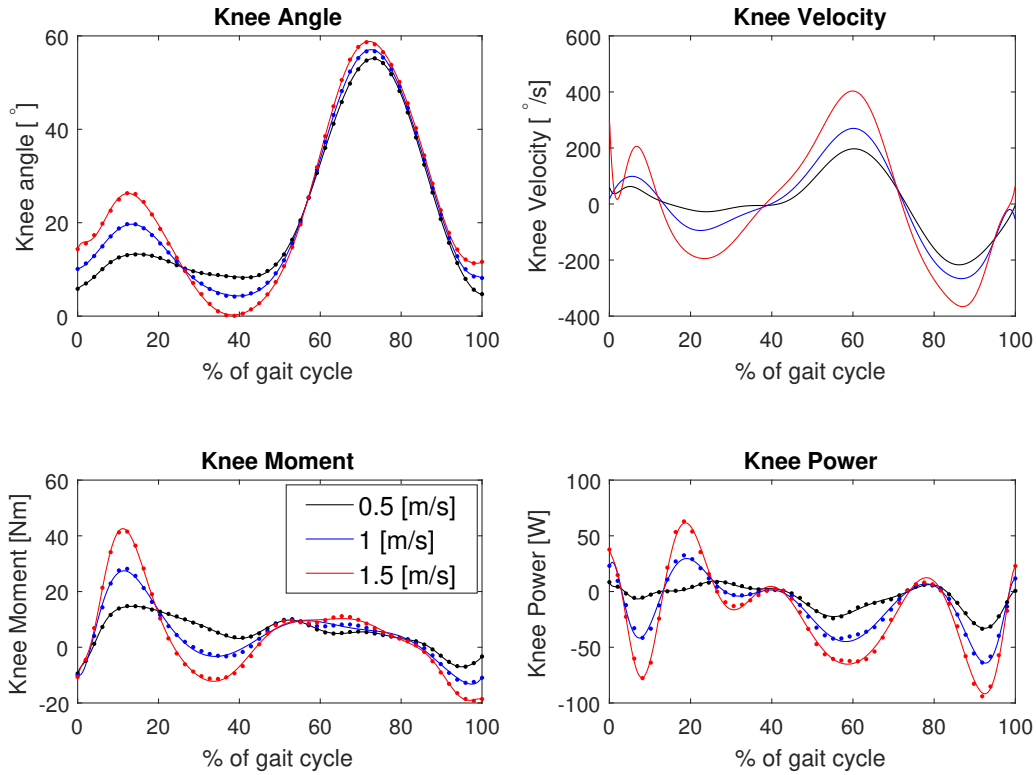

Figure 2.3: Kinematic and Kinetic data at the three different walking speeds. [48]

As the focus of this thesis is the knee joint a close look will be taken to it.

2.3.1 Knee

Knee joint plays a dominate roll both during stance, determining the limb stability, and in swing whose flexibility is critical for the limb's freedom to advance.

Knee motion

The motion patterns in the sagital plane cover a large range in opposition to the coronal and transverse motion which are rather limited. Only the sagittal motion will be presented, as it is the most complex and critical to allow body propagation. In each stride knee goes through four arcs of motion where flexion and extension permute in a particular way ranging form 0° to 70°, however this values differ according to the walking speed, body weight and leg length. [34]

Figure 2.4 illustrates an example of a knee angle profile.

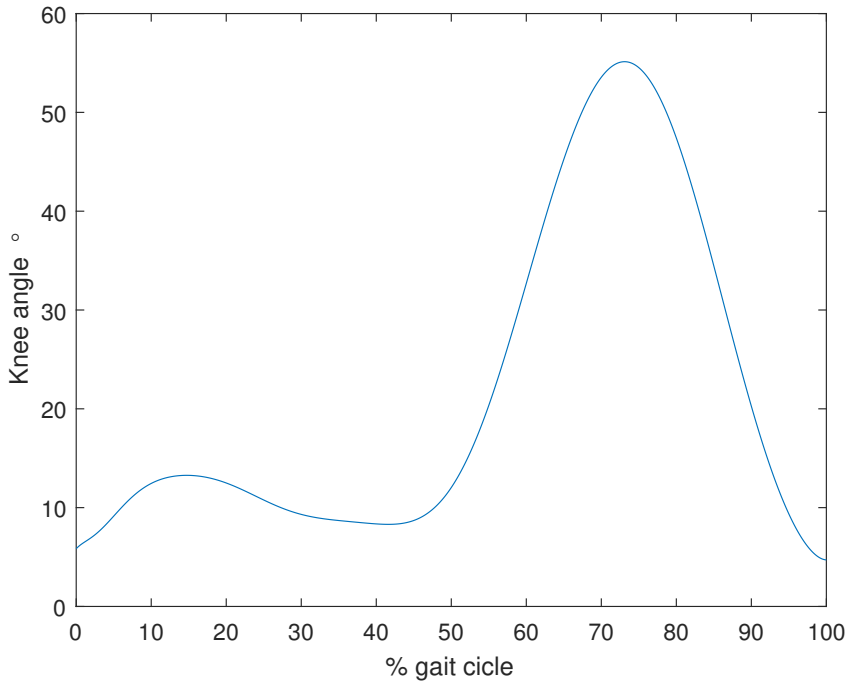

Figure 2.4: Knee range of motion for a 70 Kg male subject walking at 1 m/s.

By the time of heel strike, the knee starts to flex until reaching the peak angle during loading phase. After, extension begins, propelling the body forward, having as a consequence the knee extension. Subsequently reaching a minimum angle, flection motion begins with a high angular velocity, indicating the start of the swing phase. The leg lifts form the ground and moves forward. Then other peak knee angle is achieved, beginning the last arc of motion, knee extension, lasting until the next heel strike.

In the end, the knee pattern is presented by a sequence of extension, flexion, extension and flexion.

The figure below demonstrates the differences in the knee profile at different walking speeds. As one can see the great changes are reflected in both peak knee angles during loading and swing phase.

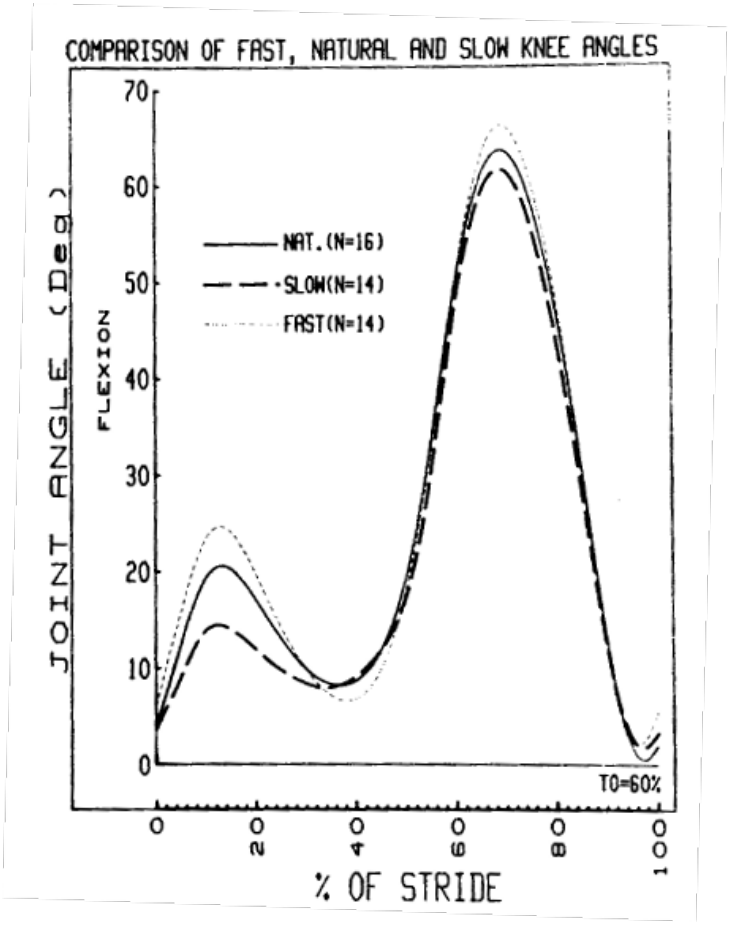

Figure 2.5: Knee range of motion for slow, natural and fast walking speeds. [47]

Knee torque

A torque pattern for the knee joint can be seen in figure 2.6.

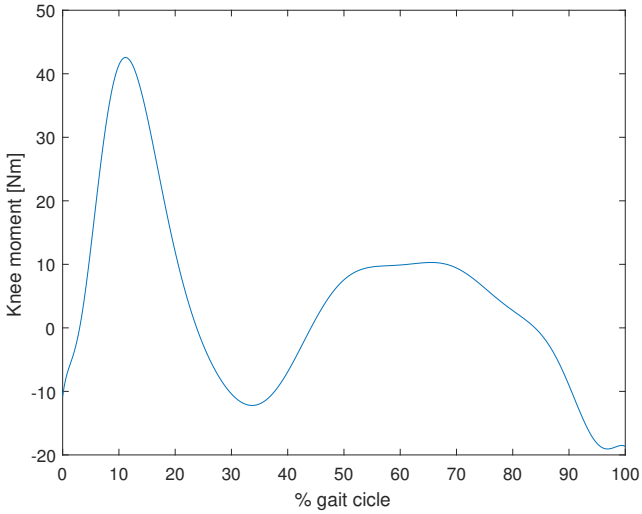

Figure 2.6: Knee torque pattern. [48]

In the begging an extersor torque is created due to the initial reaction force (figure 2.7) witch is anterior to the knee. As this vector moves forward a flexion moment is created and a maximum is reached by the end of loading phase. Then a transition to extension moment occurs as the weight transfer moves the loading vector anterior to the knee until middle of terminal stance (42% GC).Through this point on, the reaction vector starts to approach the knee joint explaining again the decreasing extension torque, and the arise of a new zero torque point at the end of single limb support (50% GC). At the pre swing phase the vector positions posteriorly to the knee creating a flexion torque.

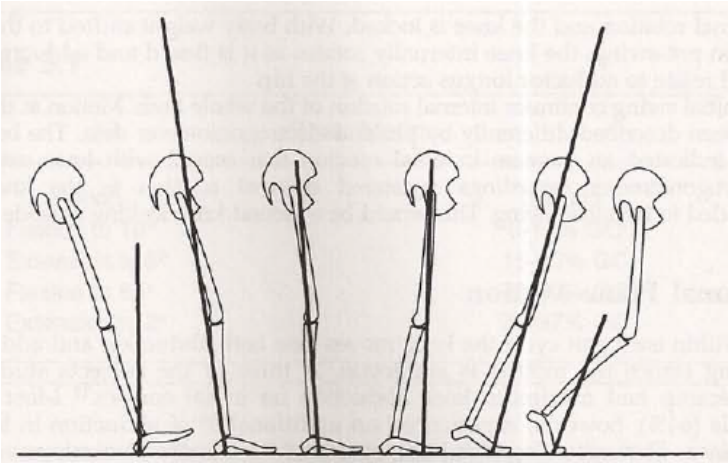

Figure 2.7: Reaction vectors until pre swing.

By plotting the knee torque with respect to the angle one can have a perception of how does the knee stiffness (slope of the curve) proceeds during gait cycle. One example of such relation is presented in figure 2.8. It is worth notice the knee spring like behavior

during the stance phase, being the stiffness represented by a uniform spring.

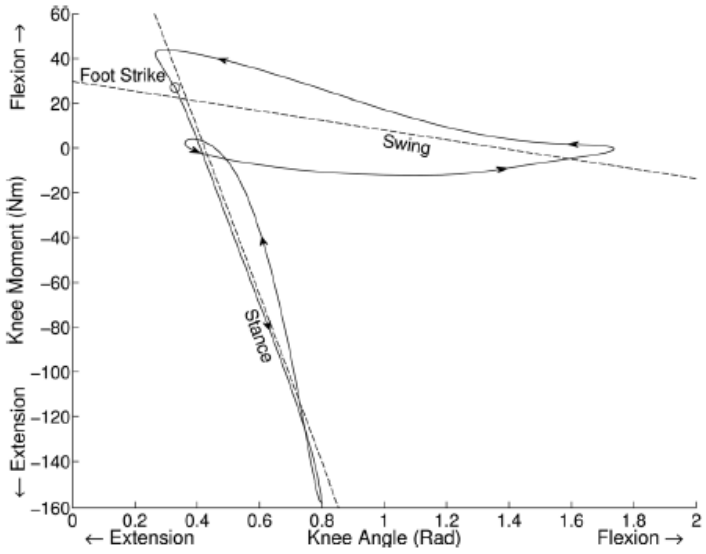

Figure 2.8: Torque-angle of the biological knee during walking. Linear regression during stance and swing phase. [9]

Walking velocity also changes the knee joint torque profile, however, instead of that profile, it is shown in figure 2.9 the peak knee moment during loading response, terminal stance, pre-swing and swing, and its evolution with the walking speed.

As one can see all the peak torques increase with the walking velocity.

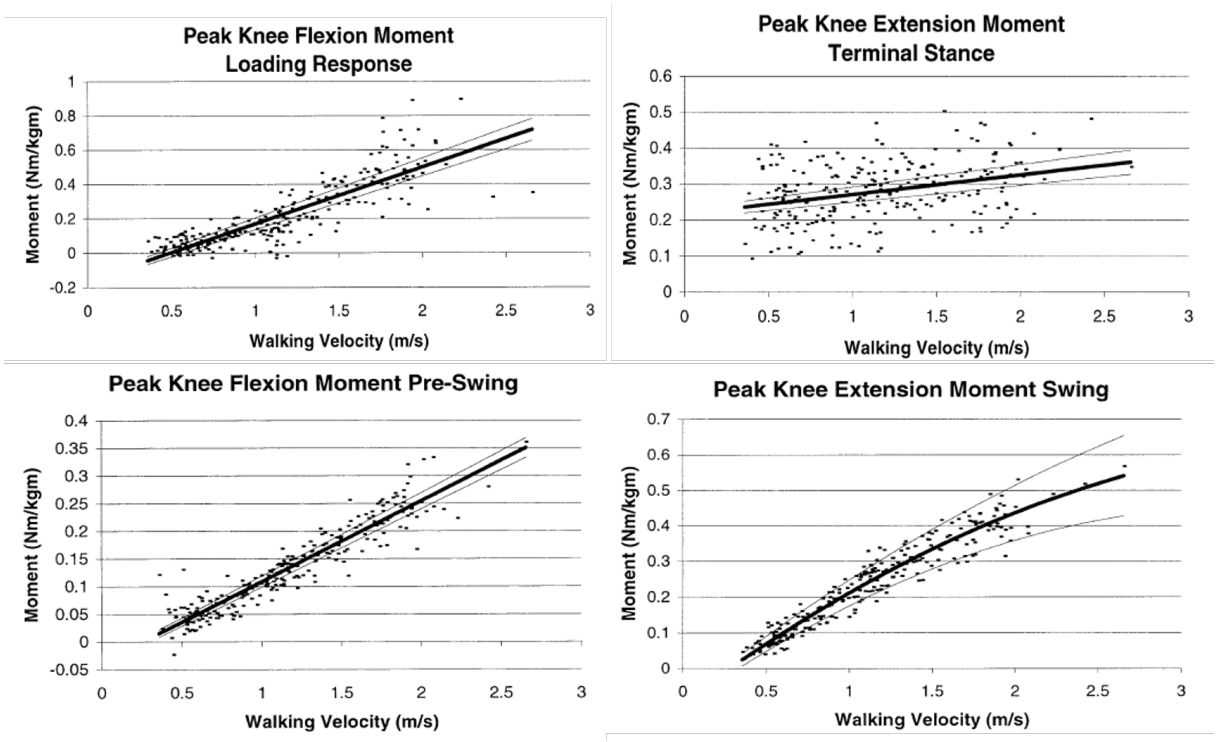

Figure 2.9: Top left : Peak Knee Flexion Moment at Loading Response ; Top right: Peak Knee Extension Moment at Terminal Stance ; Bottom left: Peak Knee Flexion Moment at Pre Swing ; Bottom right: Peak Knee Extension Moment at Swing. [21]

Knee power

The knee power is calculated using equation 2.1 and its profile during the gait cycle with three different velocities is presented in figure 2.10

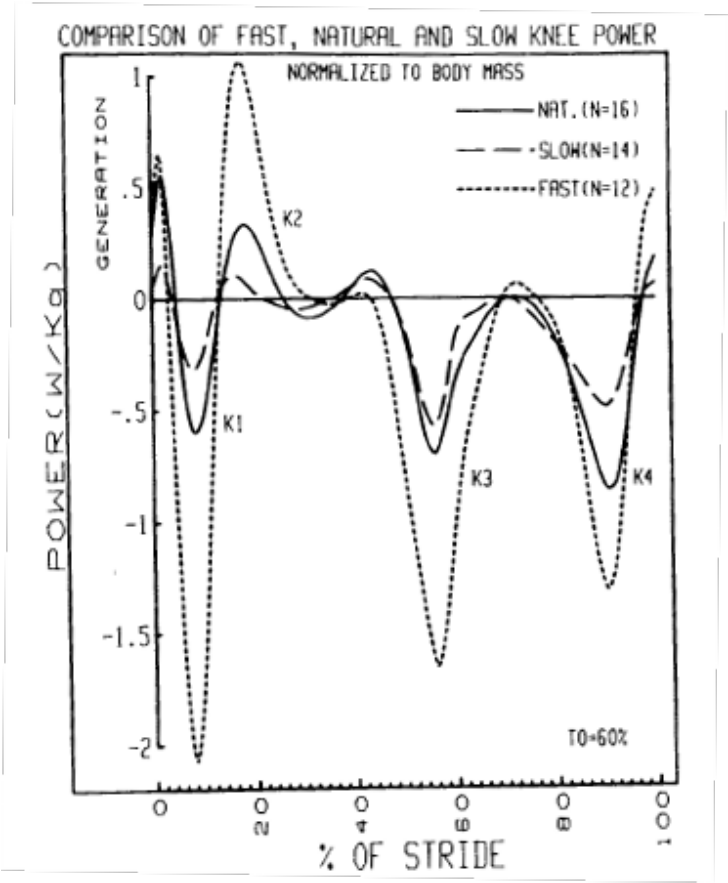

Figure 2.10: Knee power profile for slow, natural and fast walking velocities. [47]

These power profiles highlight three main regions of negative power being the first (K1) one related to the loading phase where energy absorption occurs due to the center of mass fall. The other regions are during pre- swing (K3) and finally in terminal swing (K4) to decelerate the moving limb. K2 region corresponds to positive power during mid stance.

It is also possible to represent the peak knee power in loading response, mid-stance, pre-swing and swing, with respect to the walking speed - see figure 2.11

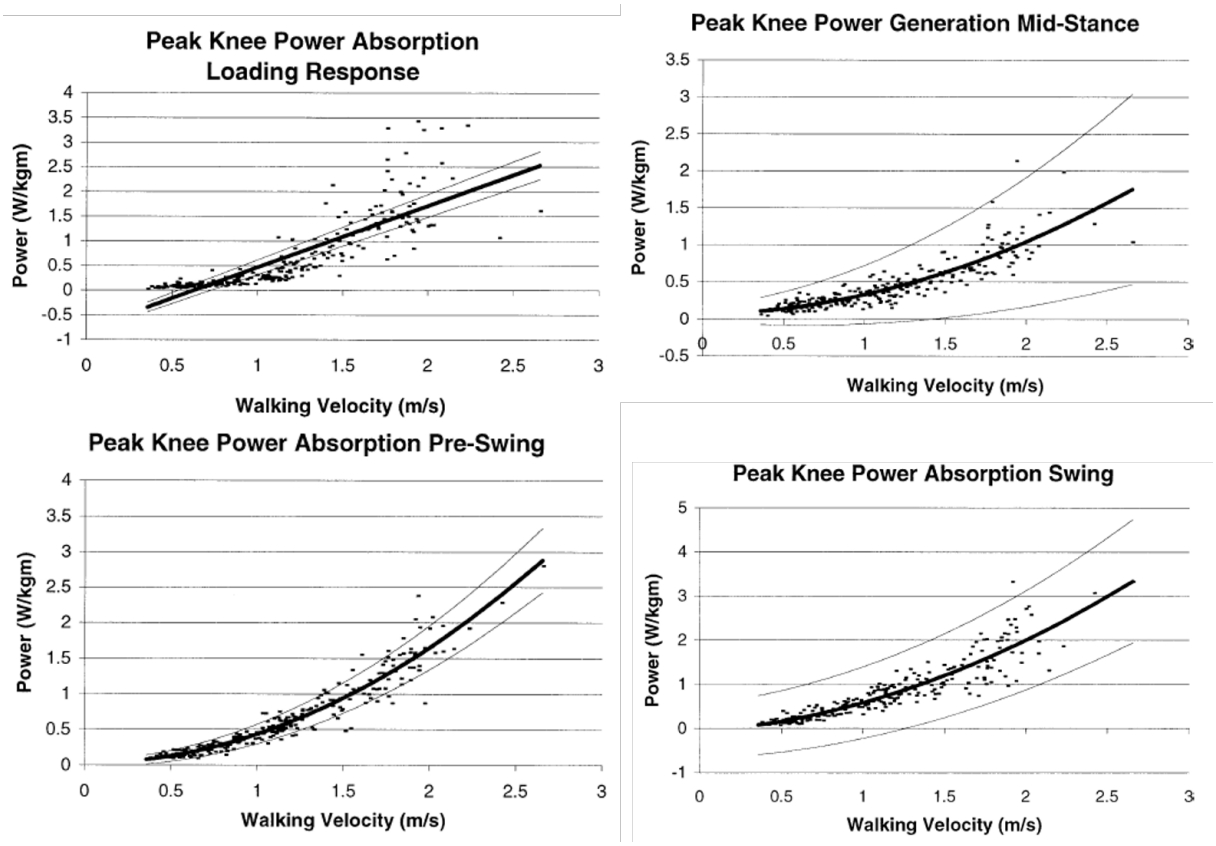

Figure 2.11: Top left : Peak power at Loading Response ; Top right: Peak power at Mid Stance ; Bottom left: Peak Knee power at Pre Swing ; Bottom right: Peak Knee power at Swing. [21]

As one can see the peak powers in each region increase with the walking velocity.

Regarding the actual work done by the lower limb muscles during one gait cycle, [30], states that stance phase only, accounts for 79.6% $\pm$ 7.5 for young and 68.2% $\pm$ 3.4 of the total energy. Such fact supports the aim of the thesis, desiring to reduce muscle work during loading response.

3. Exoskeletons for the Lower Limb

In this chapter a brief context about exoskeletons will be presented to the reader, regarding the several criteria that allow us to classify the types of exoskeletons, as well as the applications range where such can be found.

3.1 Introduction

The word, Exoskeleton, has different definitions depending on the authors. The one adopted was the following, "mechanical devices that are essentially anthropomorphic in nature, are worn by an operator and fit closely to the body, and work in concept with the operator's movements." [16] Generally exoskeleton is a term used for devices that augment the performance of an able-bodied wearer and can be applied in different fields. [16] Such fields include the military one, where this devices are used to reduce soldiers muscle fatigue under load carriage, Human Universal Load Carrier is one of such example. In the industry environment, workers may have to perform activities in harmful position for their joints and muscle, so exoskeleton are indeed useful in order to allow ergonomic postures during work, especially if these ones involve carrying heavy loads. Companies like Panasonic, BMW and Audi already have exoskeletons that help workers during their job activities. [18] The other exoskeleton market is the medical one, more specifically for rehabilitation and augmentation purposes. In the first one the user is assumed that will improve performance with time and so, the exoskeleton support will decrease, though augmentation devices are for individual with chronic motor limitations. Ekso GT and REX are respectively one example of such exoskeletons.

3.2 Exoskeletons taxonomy

The exoskeleton can be divided in different categories based on several properties that will be presented below. First the exoskeleton can be attached in the upper limb (arms and torso), lower limb (hip, knee and ankle joints) actuating in one or several joints at the same time, or in all body. The existence or absence of power is also an important parameter. [23]

Active exoskeleton can be defined as a wearable system provided with an actuator (hydraulic, pneumatic, electrical motor) capable of increasing the strength and endurance of the human limb. [6] In the other end, the passive exoskeleton, are the ones that do not possess any power source, and usually have springs to store and release energy during the gait cycle, or dampers to dissipate it. The called quasi-passive use a passive actuation system however, are provided with a power source to feed electronic components. An example of such devices is the commercial available C-Brace by Ottobock, witch have a variable damping system incorporated. Lastly, there are the hybrid-exoskeletons that contain a power source used to create Functional Electrical Stimulation which consists on electrical impulses that contract the user muscles. [23]

Regarding the control features, the exoskeleton can have a joystick (for devices that provide 100% of the motion energy); buttons or control panels usually for exoskeletons with pre-programmed modes; electrode skull cap allowing for mind control activation; sensors that monitor linear and angular acceleration, tilt angle, pressure, torque and even Electromyography signals. In the passive exoskeletons the most common is the absence of a control method. [23]

According to the building material there are two main groups, the rigid exoskeletons, built in metallic or low weight fiber-reinforced composite, and the soft exoskeleton or exosuit, that adjust tightly to the user limbs. [23]

Exoskeletons can also be divided depending whether it is in series or parallel with the limb. In the first one, loads are still totally carried by the user joints, nonetheless parallel solutions allows to reduce those loads. [23]

In the scope of this thesis only passive, in series and parallel lower limb exoskeletons will be treated.

4. Passive Mechanisms of Assistive devices for Locomotion

In the next chapter some passive exoskeletons mechanisms and results will be presented. Besides, it is also worth pointing out other passive systems, implemented in above knee prostheses, whose purpose is clearly different from the exoskeletons' one, however the mechanism principle are of interest.

4.1 State of the Art in Passive Exoskeletons

4.1.1 Series-limb exoskeleton

Ligaments and tendon are a biological strategy to reduce impact energy losses while storing some of it when striking the ground and propel the body during late stance in walking and running. This biological structures served as an inspiration for mechanical devices acting in series with the human leg. The first example of this type is the running shoe called Springbuck,figure 4.1 (a), with a carbon composite elastic midsole that showed some minor metabolic improvements ($\sim 2\%$). Other efforts have been made to improve running speed and economy by devices like the PowerSkip and the SpringWalker, figures 4.1 (b) and 4.1 (c) respectively. Nevertheless, despite this systems clearly augmented jumping height, they did not brought any benefits to locomotion economy. In fact the SpringWalker increased metabolic cost by 20% compared to walking without the device. Results which can be explained by the substantial weight increase to the human leg, requiring more work to be done by the hip to propel the limb during aerial phase. [16]

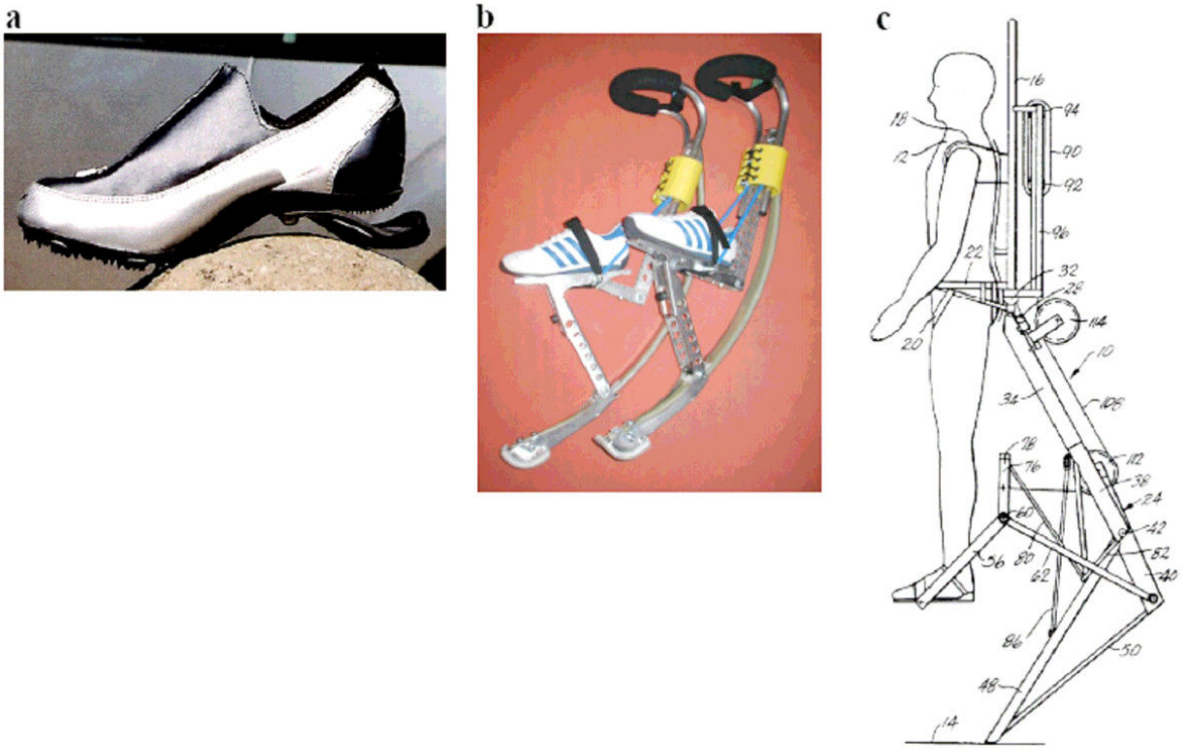

Figure 4.1: a) Springbuck ; b) PowerSkip c) SpringWalker. [16]

In series exoskeletons still cause the ground reaction load to be transferred to the human leg. However, by using a parallel exoskeleton this reaction can be held by the device only, resulting in a decrease of the limb loads and metabolic cost, both in walking and running. Furthermore the limb length would not be increased so energy doesn't need to be spent in movement stabilization. [16]

4.1.2 Parallel-limb exoskeleton

The first mention of such devices is in an America patent granted by Nicholas Yagn in 1890, whose invention is presented in figure 4.2a). This is composed of two long leaf springs operating in parallel to the legs, each supposed to engage during the heel strike, transferring the body weight to the ground and reduce the loads in the limb. The disengagement happened right before the aerial phase in order to allow the leg to flex and gain toe clearance. Until now, there was no record of a built design and it's demonstration.

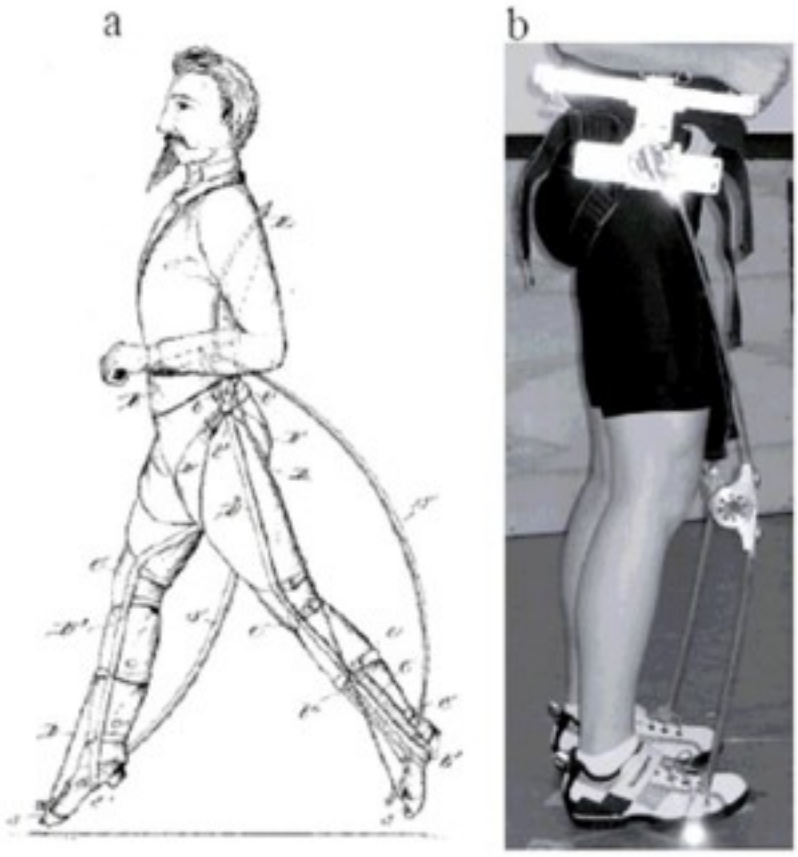

Figure 4.2: a) Yagn's running design [16] ; b) MIT's hopping exoskeleton. [15]

MIT biomechatronics group based on the design presented above, built an elastic exoskeleton (figure 4.2 b), which obtained satisfactory results. Unlike the other, whose purpose was to augment running, this was for lowering the metabolic cost. The principle was quite similar, two fiberglass leaf springs spanning the entire leg are capable of transferring body weight directly to the ground during stance period. The MIT device however cannot disengage the spring during aerial phase as it doesn't contain a clutch device to do so. Even though 24% metabolic cost reductions were reached when compared to normal walking. [15] Such value is hypothesized to be due to low activation of ankle plantar flexors and knee extensors. [9] Nevertheless the lack of a clutch resulted in an expenditure of energy in swing phase as the knee flexion compressed the spring. Later on, MIT also improved this concept by adding a custom high torque and low mass clutch as the commercial options do not fulfill both the requirements for this applications. This clutch (illustrated in figure 4.3) has a sawteeth shape with a limiting torque of 190Nm and weights 710g. The implementation of a planetary gear in the device allowed for a torque reduction in the clutch shaft, improving also the angular accuracy on engagement and allowing to machine smaller teeth. Other important feature is the usage of an encoder and a sagital plane gyroscope that are the input elements for the state machine algo-

rithm capable of identifying the gait cycle stages and de/activate the clutch according to those. In terms of power consumption the total amount of electronic components require 860mW. [9]

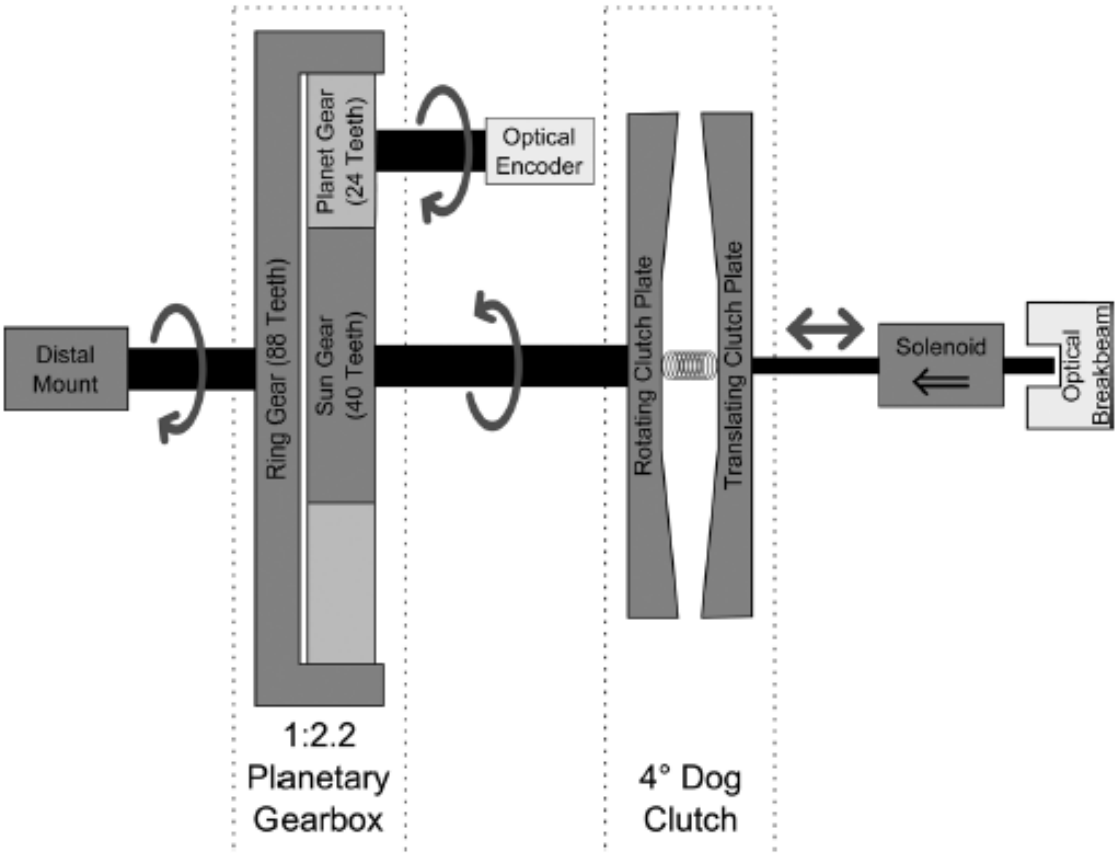

Figure 4.3: Mechanism simplified scheme. [9]

Other investigations were also made in the field of elastic passive exoskeletons with positive results achieved. As a first example, the work of [5] will be summarized. The final goal of the project was to reduce the human walking cost by an unpowered exoskeleton. Figure 4.4 demonstrates the device being used, a drawing of the parts and the clutch system. The main components of the device is a spring parallel to the Achilles tendon, whose function is to reduce calf muscle activation, and a passive clutch whose dis/engagement allows the first element to store and release energy in the right gait cycle stages. At heel strike the clutch was engaged, allowing for the spring to be loaded during the stance phase and then release all that potential energy at toe-off, giving auxiliary torque at the ankle and reducing musculotendon work. Several trials were made varying the spring stiffness and it's important to remark the non linear relation of metabolic rate with stiffness, being the first reduced until a certain value of stiffness and then increases, evolution seen in figure 4.5. This increasing values might be explained by a higher plantarflexor activity, due to a rise in contraction velocities, in the end of end stance, even though the torque

produced by this muscles decreased. Actually the metabolic rate increment can not be explained using mechanical power, because human contributions decreased with stiffness raise, nevertheless the metabolic rate increased. [5]

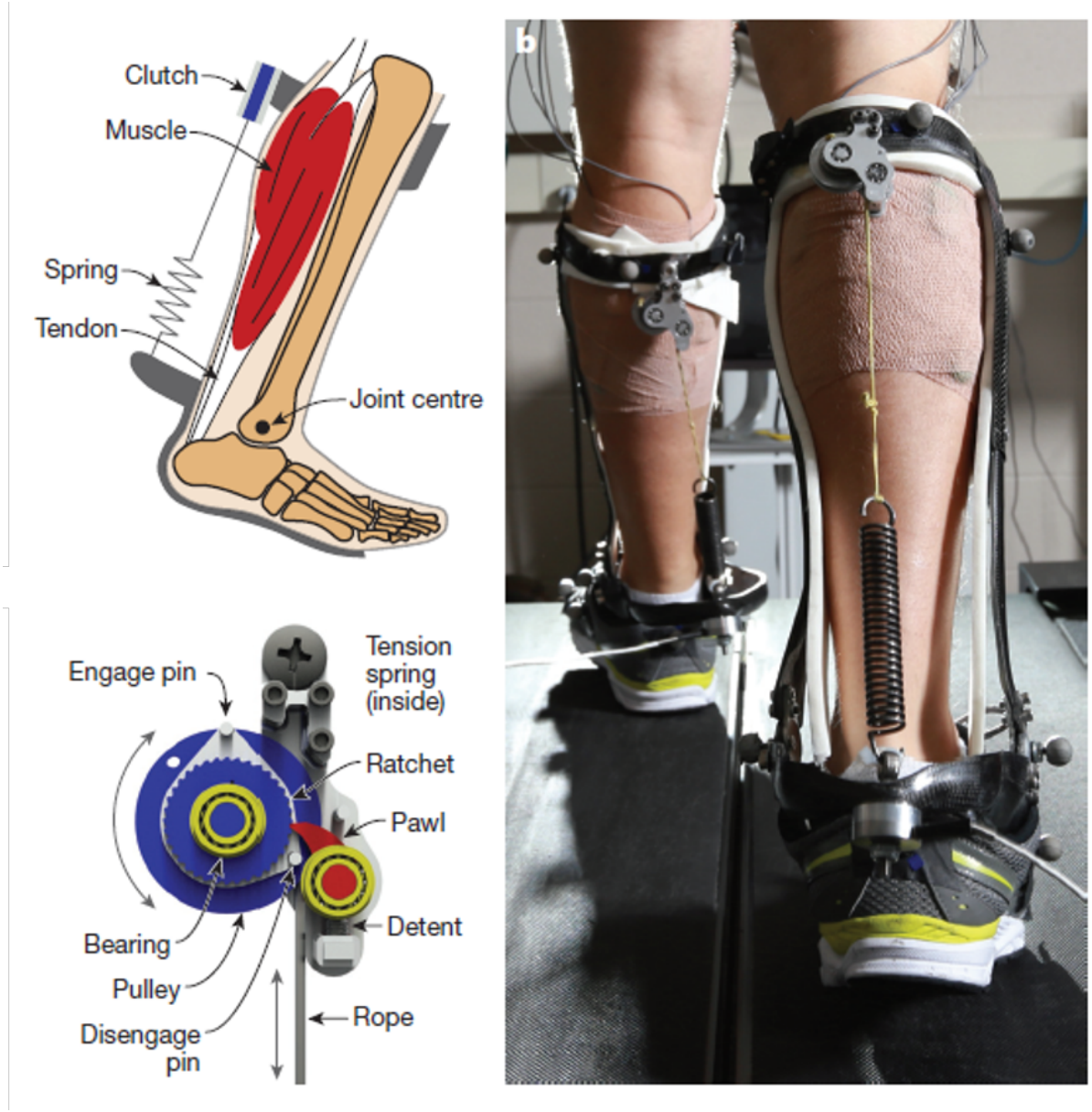

Figure 4.4: Right: User wearing the device ; Top left : Schematic picture with the device elements (Spring and clutch) and their assembly location ; Bottom left : Clutch components. [5]

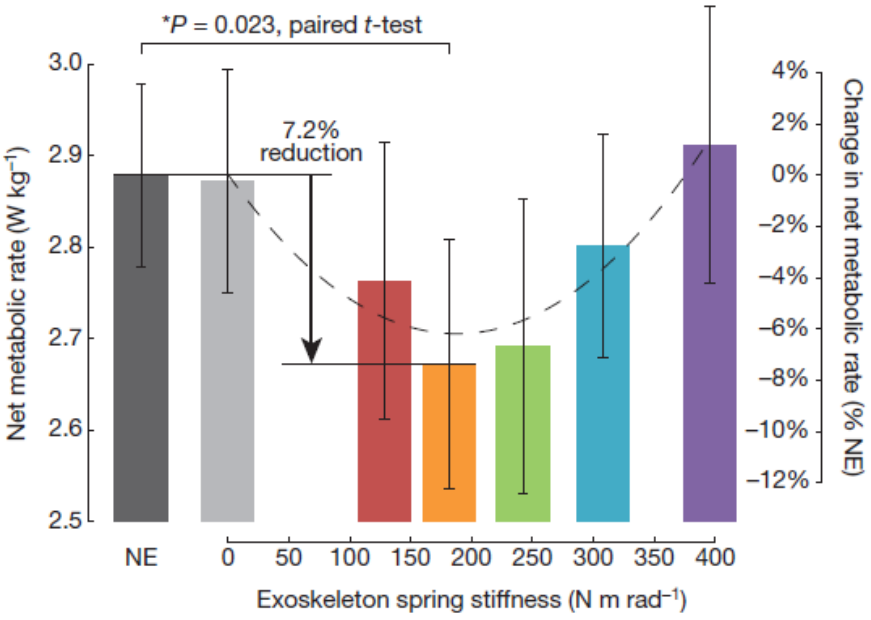

Figure 4.5: Metabolic rate evolution with spring stiffness. [5]

The clutch mechanism is worth a deeper look. The diagram in figure 4.6 is helpful to visualize the mechanism in action.

During swing the linkage (Kevlar strands plus linear spring) is allowed to move creating a rotation of the ratchet, motion which is represented as blue arrow lines in the figure. At heel strike (box in orange) however, a pin engages the pawl in the ratchet, restricting further downward motion of the linkage. As the foot plantar flexes until foot-flat position (box in purple) the linkage gains slack because of shortening distance between the two connection points. This situation inverts in mid stance as dorsiflexion begins but the clutch is engaged not allowing linkage motion and so the ratchet rotation. System responds by stretching the spring and so energy from the body's center of mass is stored (green rectangular area). At push of, all the energy previously stored returns to the ankle joint to perform positive mechanical work, resulting in forward body propelling (dark blue rectangle). During the energy release, because of the teeth ratchet shape that only allows unidirectional locking, this part rotates counterclockwise and at maximum plantar flexion other pin now disengages the pawl freeing the ankle to dorsiflex during the rest of swing, resetting the cycle. [46]

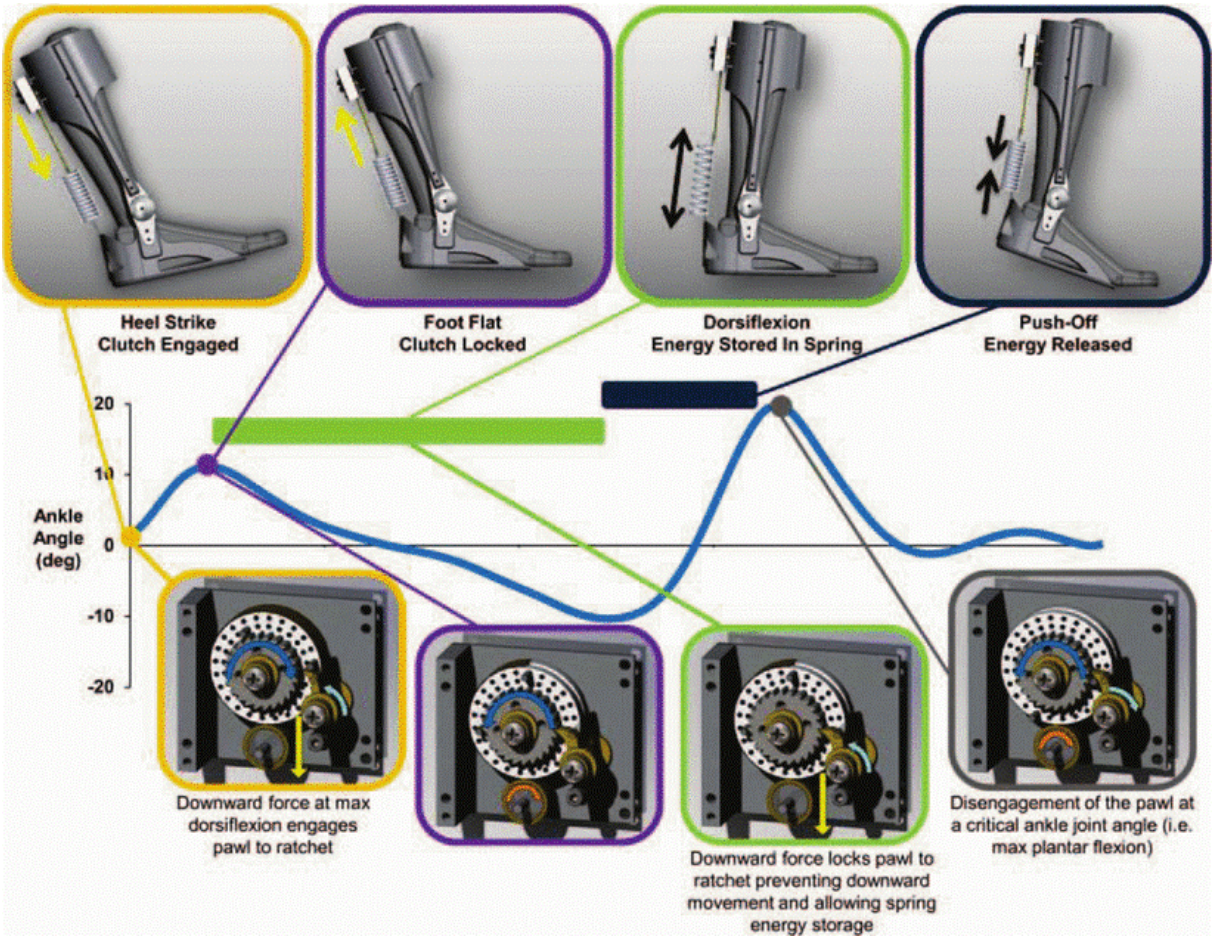

Figure 4.6: Schematic highlighting the key events of the clutch functioning over the gait cycle. The ankle joint pattern (blue line) is from a walking speed of 1.25m/s. Positive values indicate plantarflexion and negative dorsiflexion. [46]

Other similar design is presented in [5], where a leaf spring was used instead with an equivalent stiffness of $5Nm/deg$ and a clutch mechanism based on cams to dis/engage the spring. Figure 4.7 shows the several key points trough the gait cycle. The system is very identical to the previous so it will not be further analyzed. [45]

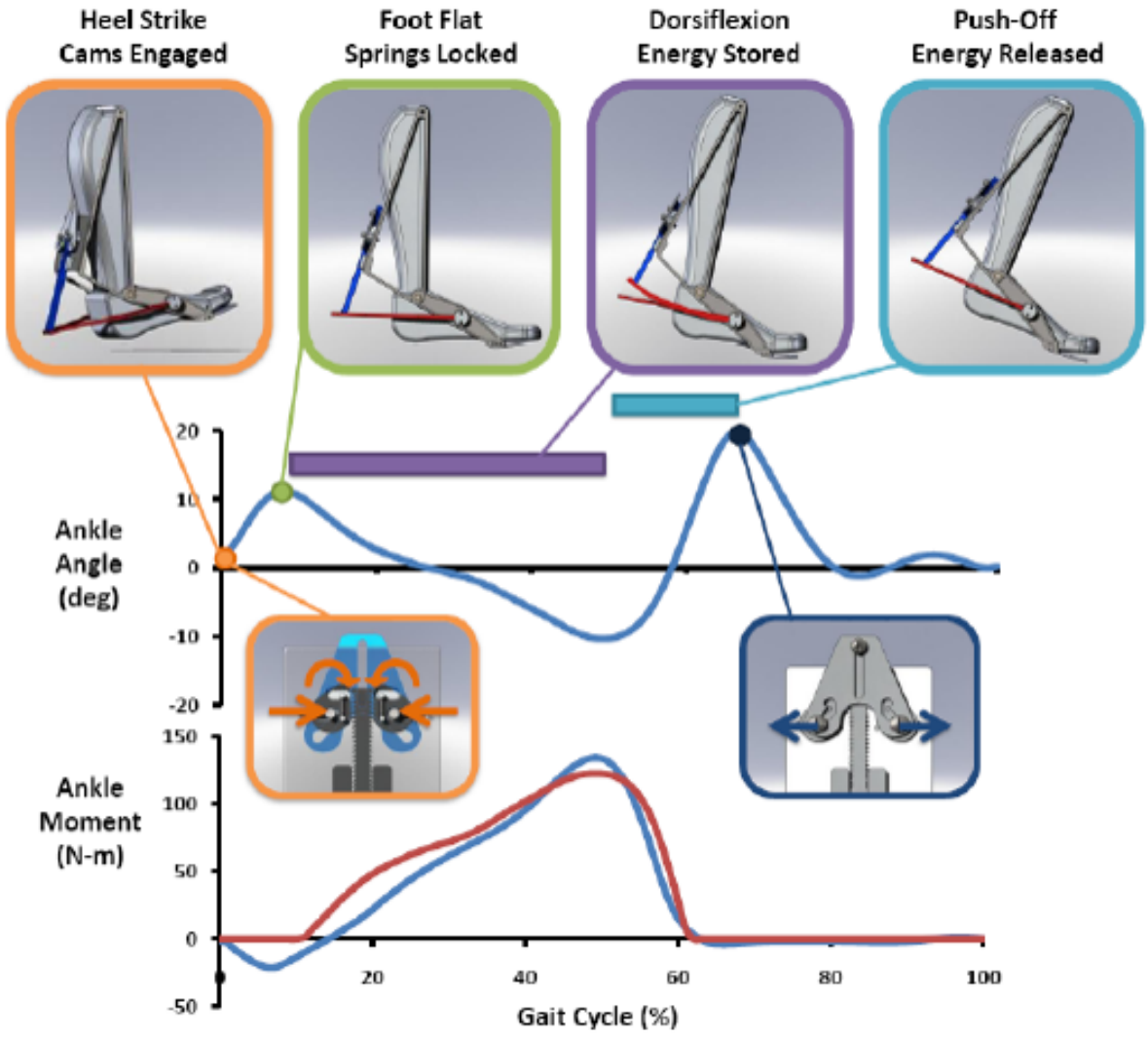

Figure 4.7: Schematic highlighting the key events of the clutch functioning over the gait cycle. The ankle joint pattern (blue line) is from a walking speed of 1.25m/s. Positive values indicate plantarflexion and negative dorsiflexion. Ankle moment blue curve is also for a walking speed of 1.25m/s as the red one represents the torque contribution of the spring exoskeleton. Orange outline panels cam/clutch engagement at heel strike. The purple bar indicates the spring storing energy period and the light blue the period of energy release tduring push-off. Dark blue panel illustrate cam/clutch disengaging the spring to allow free swing. [45]

In [42], is presented a quasi-passive exoskeleton (power is used for electronic components only) for metabolic reduction of walking while carrying a load. The device presented in figure 4.8 is composed of two parallel legs that transfer payload forces to the ground. For energy storage, two springs are employed in the hip and ankle. To ensure knee muscular effort reduction during early stance, a variable damping is implemented. This variable damping was a commercial one made by Össur of Reykjavik, Iceland. The human interface is made by means of a backpack shoulder straps, a waist belt, thigh cuffs and cycling shoes. Regarding the DoFs, the hip joint has three in order to mimic the biological ball

and socket joint, both knee and ankle have one DoF. The exoskeleton ground interface is made by a carbon fiber foot-ankle produced by the same company as the variable knee damper. [42]

Through experimental trials of a person carrying a 75lb (34Kg) payload it was possible to conclude that the device actually increased metabolic cost by 39% compared to carrying the same weight without the exoskeleton. However by removing the variable damping knee and replacing it by a simple pin joint, the metabolic cost reduced 34% in the same testing conditions. One can hypothesis that the damping advantages are overtaken by the adding mass. The influence of this adding mass is greater as this moves distal to the hip joint, increasing the moment of inertia relative to this joint requiring more torque in order to swing the leg. [42]

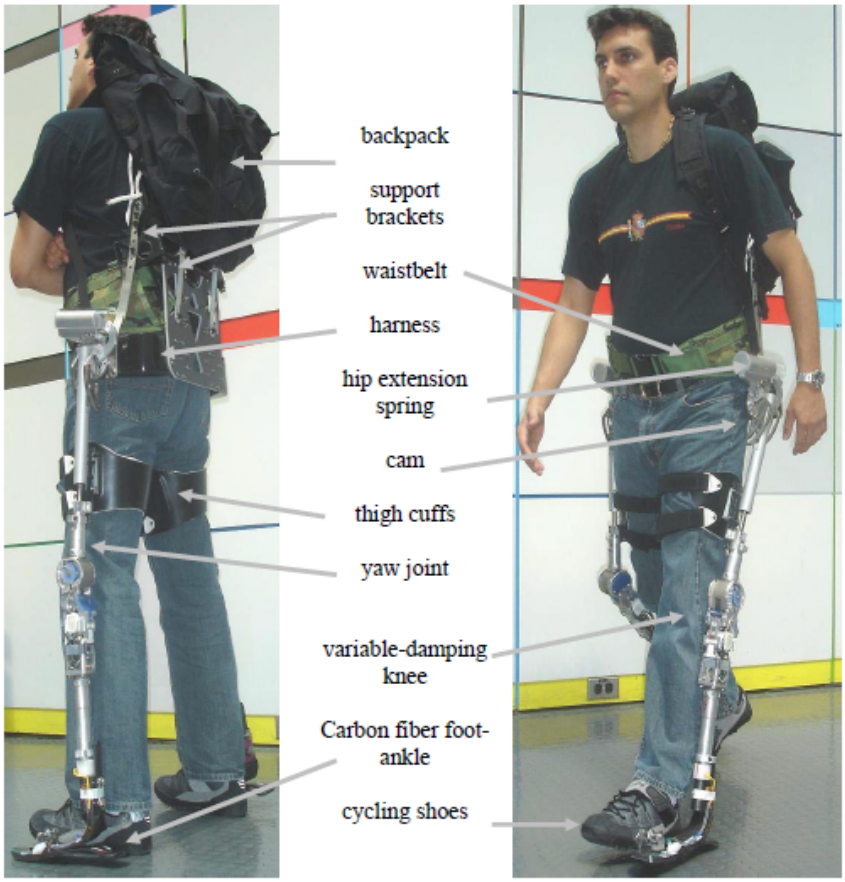

Figure 4.8: Picture of exoskeleton being worn and it's main parts. [42]

Although positive results have been presented, that is not always the case as it can be seen in [43]. In this article a passive exoskeleton named XPED 2 (figure 4.9) was studied. This one uses the concept of exotendons, which are basically long elastic cables spanning multiple joints. This cables act just like a spring, storing and releasing energy between joints. Figure 4.9 a) illustrates the working principles enumerating the several

components, being the main functional one the exotendon 3), a cable that spans between a lever at the pelvis 1), via a pulley at the knee 4), to a leaf spring at the foot 5) which gives elasticity to the mechanism. Because of the cable's offset relatively to the joint centers, the spring deformation and so the force acting on the cables will depend on the joint angles. Hip extension and ankle dorsiflexion will tighten the cable and hip flexion and ankle plantarflexion will loosen the cable. In some joint angle combination the cable will be slack meaning no forces on it. The moment on each joint is a simple multiplication of the cable's force and the joint offset. Human-exoskeleton interface is made by a rigid frame 2) connected to the pelvis, shank and foot segments. In figure4.9 b) the several XPED 2 DoF are highlighted by arrows, showing that six are active per leg. This ones are flexion/extension, ab/adduction and endo/exorotation at the hip, flexion/extension at the knee, plantar/dorsiflexion and pronation/supination at the ankle. [43] The exoskeleton experiments lead to conclude that although hip and knee kinematics were almost unchanged compared to walking without the device, the same was not applied to the ankle, where the maximum dorsiflexion angle decreased 5° compared to normal locomotion conditions. Regarding the metabolic cost there was an indication that this actually increased (figure 4.10) although the human joint torque was indeed reduced. In fact tendons are already biological energy transfer mechanism and the addiction of exotendons might interfere with this saving systems, increasing the locomotion metabolic cost. Other justification is the substantial leg weight increase, due to the 6.92Kg distributed through the lower limb. [43]

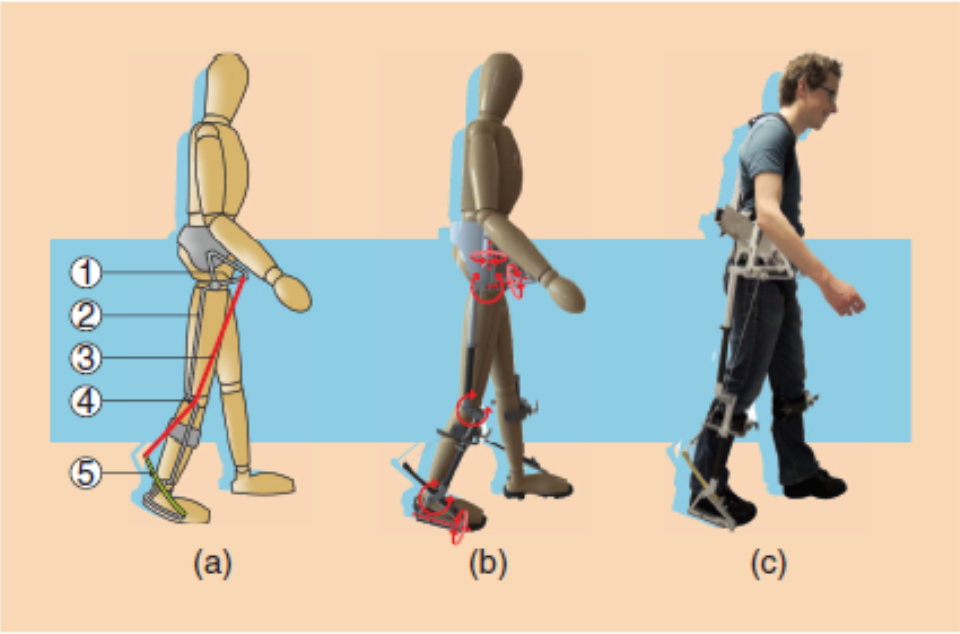

Figure 4.9: a) Working principles ; b) Active degrees of freedom (DoF) ; c) User wearing XPED 2. [43]

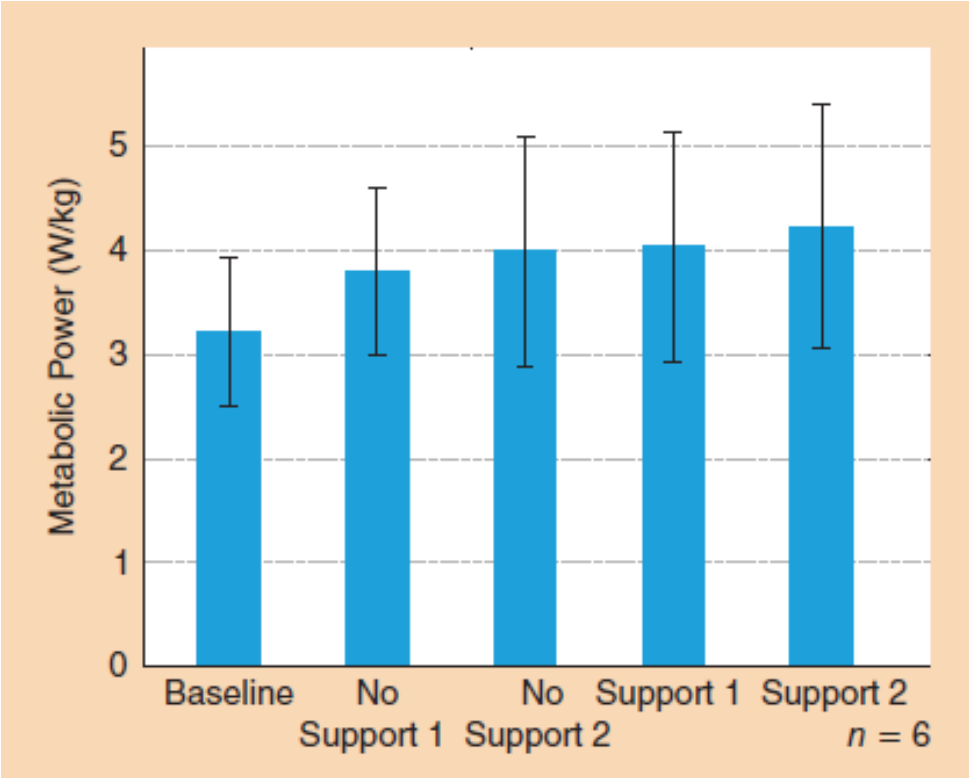

Figure 4.10: The metabolic cost: The bars represent the average over the subjects with the standard deviations.The no support 1 and 2 are the first and second test respectively with the worn exoskeleton without the springs attached. The support 1 and 2 are the first and second test respectively with the worn exoskeleton when the springs are attached. [43]

4.1.3 Passive exoskeletons overview

Table 4.1: Passive exoskeletons overview. Negative values for the metabolic reduction indicate a metabolic increasement, and vise-versa.

	Name	Spring	Damper	joints	Metabolic reduction
Series	Springbuck [16]	×			+2%
	PowerSkip [16]	×			–
	SpringWalker [16]	×			-20%
Parallel	MIT's hopping [9]	×		Knee	+24%
	Unpowered Exo. [5]	×		Ankle	+7.2%
	Leaf spring [45]	×		Ankle	–
	Load carry [42]	×	×	Ankle/Knee/Hip	+34%
	XPED 2 [43]	×		Ankle/Knee/Hip	–

Every system analyzed, except one, relied on the use of a spring to store and release energy. Indeed, as mentioned in section 2.3.1, the knee has a spring-like behavior in the stance phase, commonly motivating the usage of a spring mechanism.

On the other hand, considering the full gate cycle, this joint has three time-intervals of energy dissipation, which resembles the behavior of a damper. This thesis took this consideration, following a different approach of the most used in the state of the art. In fact, only one exoskeleton (for the knee) was found using a damper, but, firstly, it did not have a beneficial result [42] and, second, an expensive and too complex damper was selected, while this thesis proposes the design of an economical mechanism.

4.2 Other passive mechanisms – Knee Prostheses

Knee prostheses mechanisms also use passive elements like springs or dampers in order to fulfill their use. Springs solutions have already been presented so more focus will be given to the damper systems. This operate using fluids in liquid or gas states, that dissipate the energy via viscous motion resulting then in an increment of the fluid internal energy. The system can be described as a simple dash-pot where the holes function can be replaced by valves with a variable or static displacement depending on the solution complexity. The first type are capable of changing the damping coefficient, depending on the velocity and also the gait cycle stage. An example of such devices is presented below being applied in a transfemoral knee prosthesis.

The damper, whose explication follows, is a pneumatic swing-control above knee prosthesis whose main goal is control the shank motion during this gait cycle stage. For that purpose a double pneumatic actuator with three valve step up was built, being two of those bidirectional flow control valves, L and R and one check valve. The flow control valves also called leak rate valve are a crucial component being responsible for the damping and elastic effect on the system. If closed the devises behaves as a pneumatic spring and so the energy is stored and is only a function of position, meanwhile if opened the air will flow from the pressurized chamber to the other resulting in an exchange of mass. In the end most of energy is dissipated through heat by an increase of the air internal energy. Also important to remark that the Pressure-displacement evolution is now highly dependable with the piston velocity and the valve opening. The relation curves differ from the pneumatic spring being this values lower as the valve opening increases. [19]

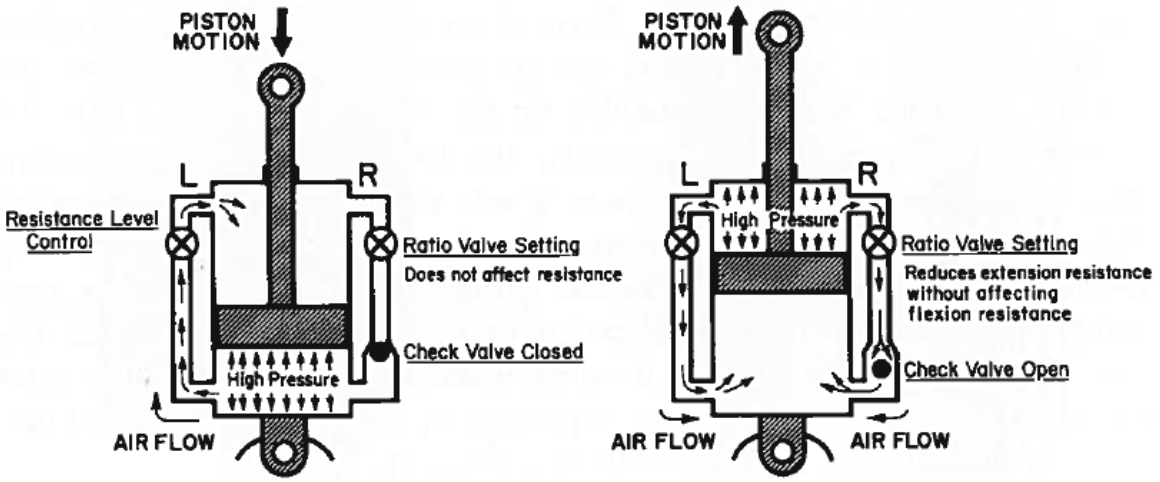

Figure 4.11: Right: Air flow corresponding to knee flexion ; Left: Air flow corresponding to knee extension. [19]

During initial swing the knee flexes and from the actuator view point, a high pressure is built in the lower chamber and air flow is made trough L valve,witch is the dominant damping element in this phase, to the too chamber. When maximum flexion angle is reached the pressure difference between the chambers might not be reestablished due to the low flow valve opening or the high velocities. The consequence is an initial thrust in extension motion, however as it progresses the top chamber is pressurized and flow is made from top to bottom, though this time the check valve opens and both L and R valves serve as path for the air reducing the motion resistance. During stance phase the pressures on the chambers are equalized and prepared for other duty cycle. [19]

5. Knee damping coefficient estimation

5.1 Gait data analysis

When designing a passive system, it is necessary to know the required knee damping coefficient for different walking speeds. However, these values are hard to generalize for different subjects as the damping coefficient changes with their leg length and weight. Still, one can estimate such values for an average person. So, the joint Kinematics and Kinetics data from a 70Kg male individual with a leg length of 90cm, walking at 0.5, 1 and 1.5m/s [48] were analyzed and the extracted coefficient used as reference for the design.

The knee angle, velocity, torque and power are plotted in figure 5.1. It is important to state that the data presented, expect for the angular velocity, resulted from a polynomial fit to the original data. The coefficient of determination, R^2 for each fit is shown in table 5.1.

Table 5.1: Polynomial fits.

Velocity (m/s)	0.5	1.0	1.5
Polynomial Degree	18	13	15
Knee Angle R^2	1.0000	0.9999	0.9999
Knee Moment R^2	0.9991	0.9926	0.9984
Knee Power R^2	0.9951	0.9897	0.9951

The angular velocity was obtained using two consecutive times and also the difference of the knee angle at each time considered. Equation 5.1 translates this relation mathematically.

$$\dot{\theta}_i = \frac{\theta_{i+1} - \theta_i}{t_{i+1} - t_i} \tag{5.1}$$

With the polynomial fit instead of the 50 points available in the original data one can have as many points as desired, which allowed a more precise calculation of the angular velocity.

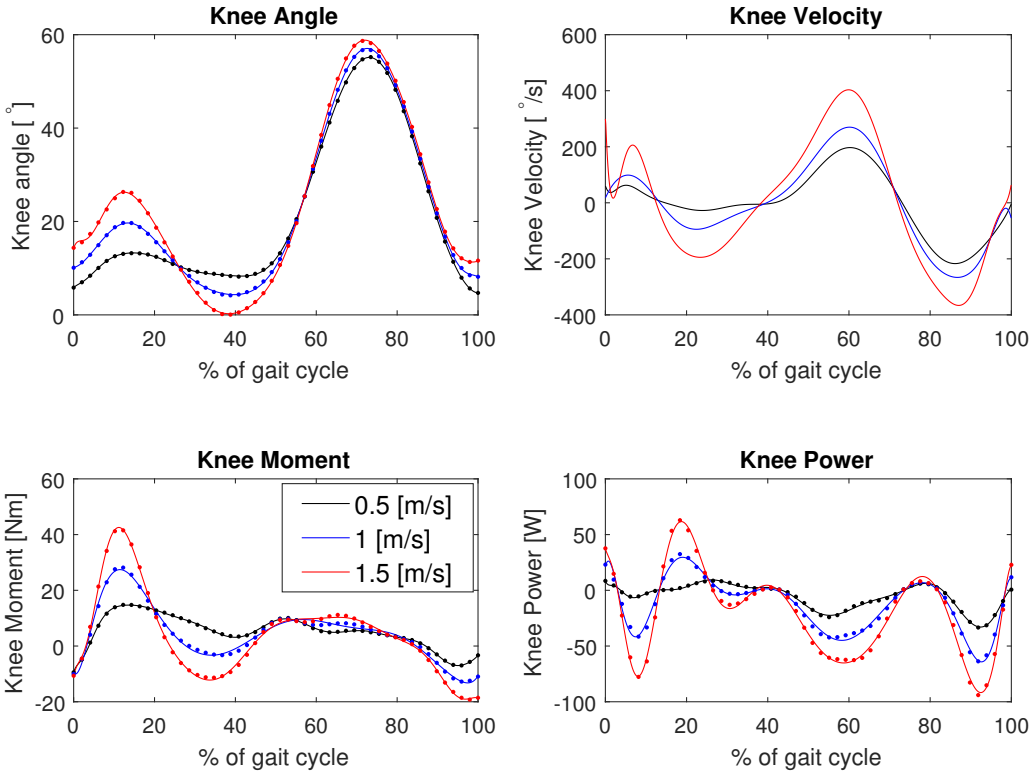

Figure 5.1: Kinematic and Kinetic data at three different walking speeds (0.5, 1.0, and 1.5m/s).The lines are the curve fitting result and the dots represent the data used to make them.

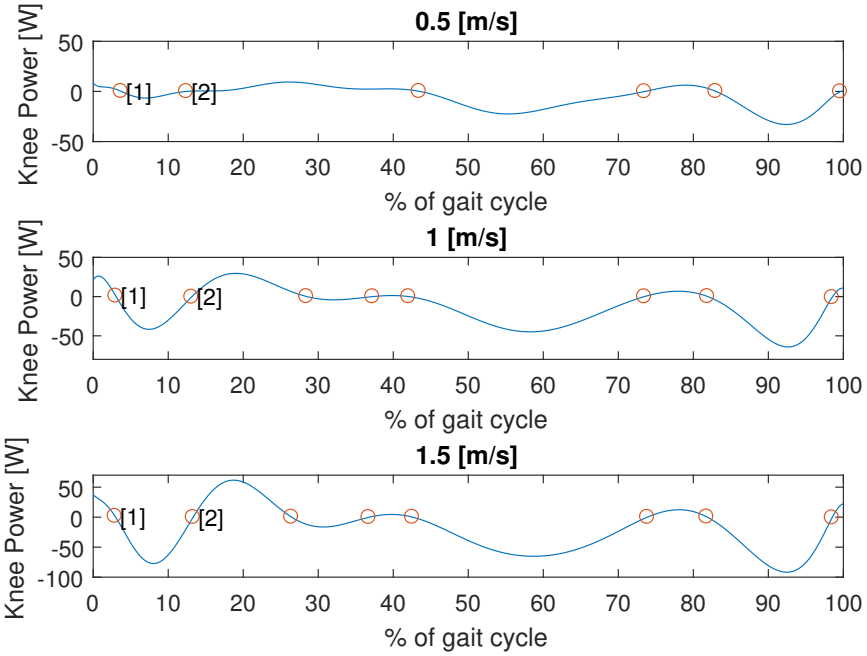

Figure 5.2: Points where the knee power is null. K1 region is defined between points 1 and 2.

It is, then, necessary to know, for each speed trial, which region corresponds to K1. This was done by simply identifying the points where the Knee power profile is zero. The region of interest is between the first and second point as indicated in figure 5.2.

Having the K1 region defined one can obtain the damping coefficient evolution with respect to the knee angle (represented in figure 5.3). This parameter is calculated in each point by doing the division below:

$$C_i = \frac{\tau_i}{\dot{\theta}_i} \tag{5.2}$$

where C_i, τ_i and $\dot{\theta}_i$ are the damping coefficient, the knee moment and the knee angular speed at each point i, respectively.

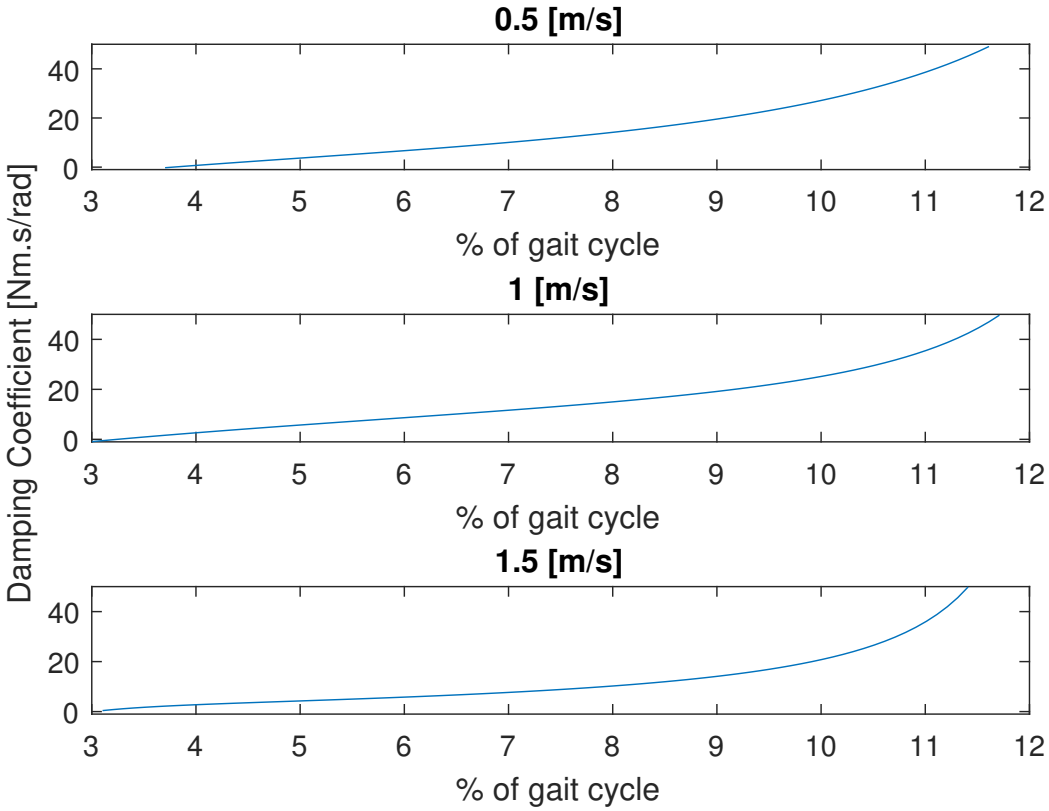

Figure 5.3: Damping coefficient for the three velocities during the K1 region.

As the gait cycle develops, the damping coefficient tends to infinity, because of the zero angular velocity reached at the end of K1, which corresponds to the angular peak during the loading response. Consequently, in the figure above (5.3), the plot was limited to 50N.m.s/rad, in the y-axis, because the very high damping coefficients close to the end of K1 ($\approx 12\%$) did not allow the smallest values to be visible.

An alternative to visualize the data is to plot the knee moment with respect to the angular velocity. The results are presented in figure 5.4.

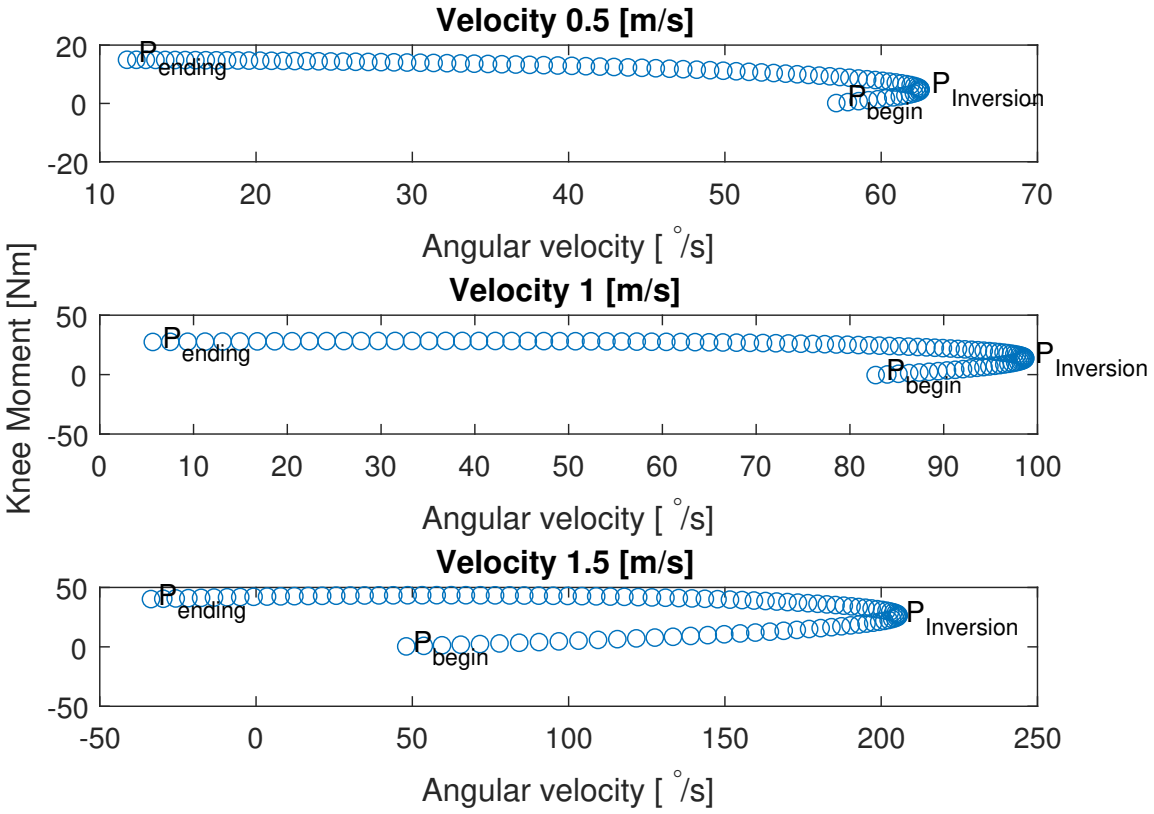

Figure 5.4: Knee Moment with respect to the angular velocity.

A very important observation results from this analysis: biologically, some velocities are associated with two different values of moment. However, for a device to reproduce this behavior, the damping coefficient would have to change dynamically during the gait cycle, requiring an extra system to induce that modification and, consequently, increasing the complexity of the device. As a first approach, a simpler system is desired, so, in this thesis, the damping mechanism was considered to be only changeable before start walking.

5.2 Damping coefficient estimation

A very simple approach is done in order to find a suitable reference value for the damping coefficient. For each walking velocity the following calculations are performed.

$$E_{K1} = \int_{t(P_{begin})}^{t(P_{ending})} C_{Damper} * \dot{\theta}^2 dt \tag{5.3}$$

$$\int_{t(P_{begin})}^{t(P_{ending})} W_{Knee} dt = C_{Damper} * \int_{t(P_{begin})}^{t(P_{ending})} \dot{\theta}^2 dt \tag{5.4}$$

$$C_{Damper} = \frac{\int_{t(P_{begin})}^{t(P_{ending})} W_{Knee} dt}{\int_{t(P_{begin})}^{t(P_{ending})} \dot{\theta}^2 dt} \tag{5.5}$$

Basically, C_{Damper} is found integrating the given knee power, and the knee angular speed squared. Table 5.2 indicates the calculated values for this parameter. Indeed the results are odd because there is not a continues growth of the damping coefficient with the walking velocity, making the calculation method not trustworthy (too simplistic). Nevertheless this data is still used.

Table 5.2: Damper coefficient values for each walking velocity studied.

Walking Velocity	0.5m/s	1m/s	1.5m/s
C_{Damper}N.m.s/rad	5.72	14.41	7.93

Following this, the real knee torque can be compared with the one created assuming the calculated damper coefficients, if the kinematic profile for each walking speed is used. The result is presented in figure 5.5.

As one can see, in the beginning of region K1, the damper moment is bigger than the real knee moment, leading to the conclusion that a kinematic change will occur in the knee. In addition, the constant damping consideration approximates the real knee moment poorly, yet, allows to have some reference numbers for that characteristic.

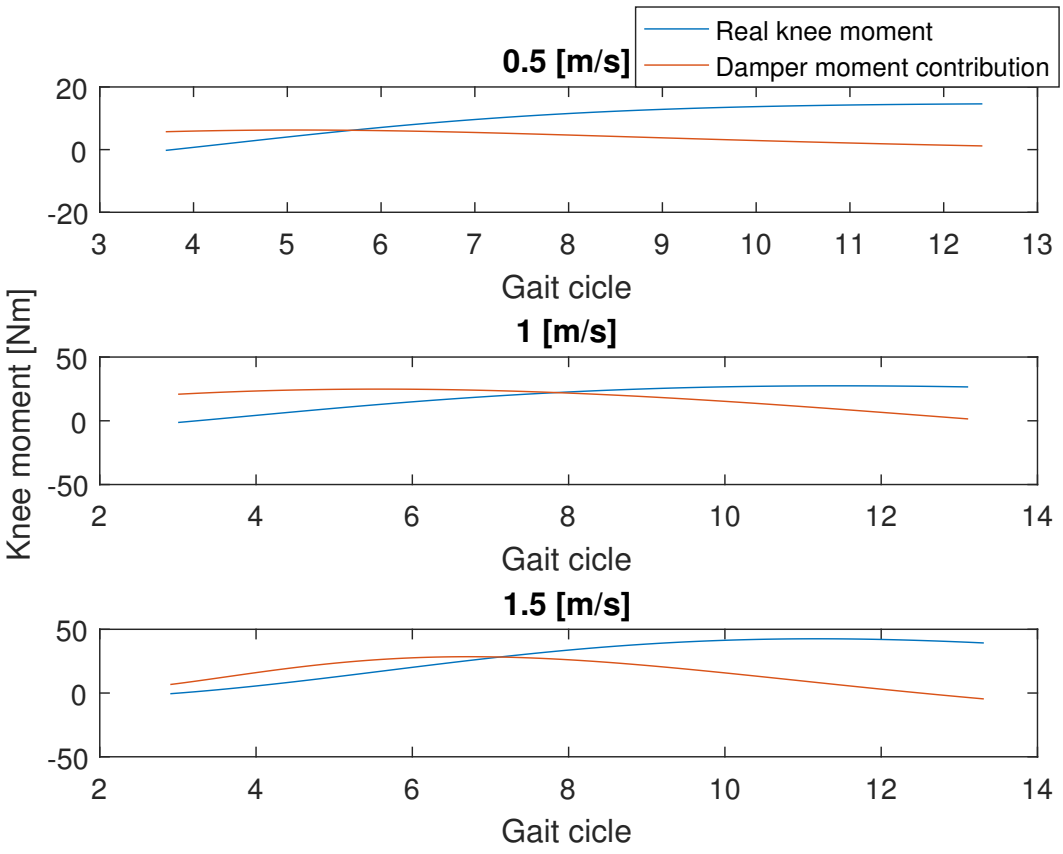

Figure 5.5: Comparison of the real knee moment with the one produced by the calculated damper coefficients for the three different walking velocities.

5.3 Conclusion

In this chapter, a gait cycle at three different walking speeds was evaluated, to address some reference values desired for the damping coefficient of the device's damping mechanism. This analysis showed a high variation of such coefficient with the walking speed, implying that, ideally, the selected damper should be tuneable, ranging its coefficient from 5.72 to 14.41 N.m.s/rad. Of course these values are obtained from data of one person only, being subjected to error both in data acquisition and post-processing. Still, these are useful to gain sensibility to this coefficient value, even tough it can poorly reproduce the real knee moment, 5.5. So, the damper selected in chapter 7 should have a damping coefficient between 5 and $15 N.m.s/rad$.

6. Solution 1 - Pneumatic actuator

This system is meant to have a pneumatic actuator connected to the thigh and shank. By using a restriction valve that allows communication between the two chambers, air flow would suffer a resistance and energy would be wasted in the form of heat. A by-pass would be required to free the system, so that the user could move the limbs, ideally with null resistance in specific gait phases.

This chapter offers a theoretical and preliminary analysis, as rigorous data for the valves were not found, and, consequently, values of some parameters had to be assumed.

6.1 System overview

For the system to be able to properly provide the required knee torque, some internal pressure, bigger than the atmospheric one, must exist. This unknown pressure is determined in section 6.2 based on a subject's kinematic and kinetic data from several walking speeds (addressed in chapter 5). The pressure must be held in the system, and for that, the two chambers must be connected and isolated from the outside. Besides this, the effective chamber area must be the same, otherwise, with the same pressure on both sides, the forces transmitted to the limb segments would be different, causing distortions in the walking pattern. The conclusion taken is the need for a symmetric chamber area, leading to the use of a through-piston-rod pneumatic actuator. To actually dissipate energy, a restriction flow valve is used, being regulated according to the person and his/her walking speed. However, it is only supposed to be active during the K1 region. After that, a parallel system must deviate the air flow from the restrictor, making the device transparent to the user. Such flow change is done by a 5/2 pneumatic solenoid valve, that when piloted can direct the flow from one chamber directly to the other reducing the pressure difference between them (so the system resistance), or force the air through the unidirectional flow restrictor valve (UFRV). The other valve, a 2/2 normally closed (NC), is used so that air can fill the chamber and remain in the pneumatic circuit.

In figure 6.1, the pneumatic configuration can be observed.

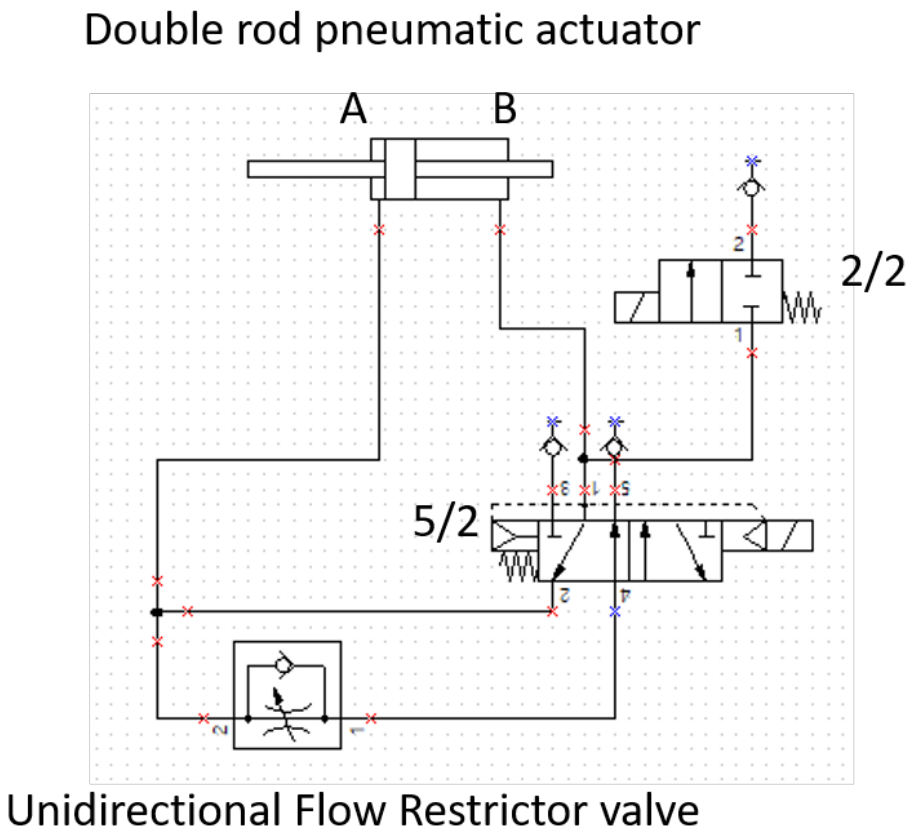

Figure 6.1: Pneumatic circuit and its components.

Regarding the connections to the limbs, the actuator rod can be linked, for example, to the shank, forcing the actuator body to be locked to the thigh. This strategy will result in the movement of the other rod during the gait cycle, and special attention must be taken to avoid this moving rod to touch the human body. The actual interface between limbs and actuator is not studied here, but figure 6.2 demonstrates an example of an active knee exoskeleton whose limb connections can be applied to this pneumatic solution.

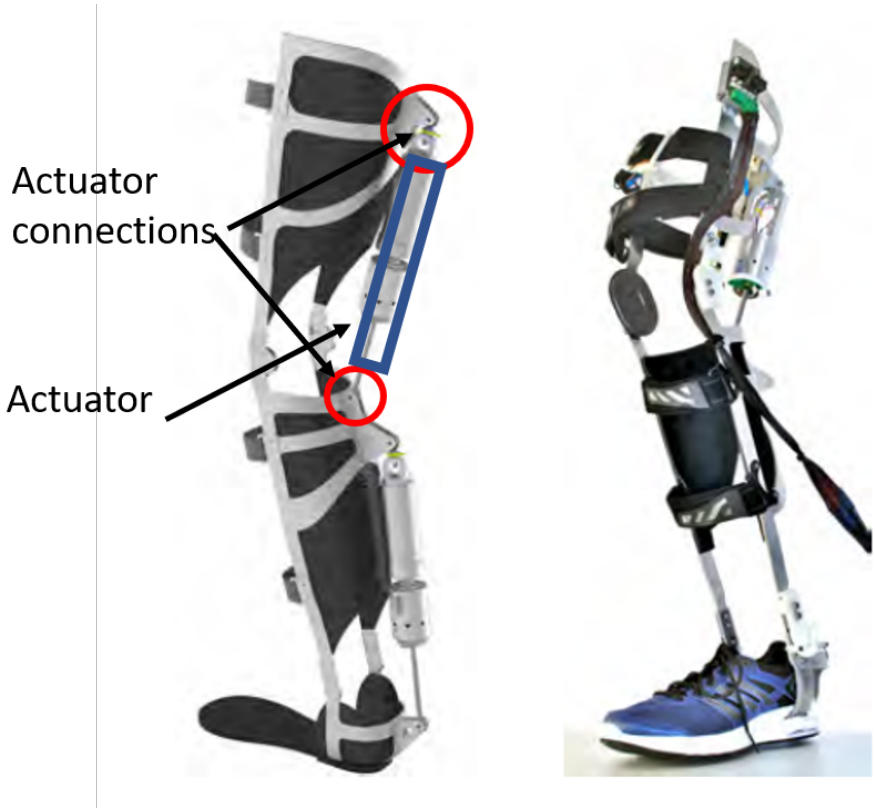

Figure 6.2: Lower Limb Exoskeleton KIT-EXO-1. An example regarding the actuator-limb interface. [3]

In the next paragraphs, the system usage in each phase of the gait cycle will be explained in detail:

At the heel strike instance, the actuator starts to compress, meaning air flows from chamber A to B (see 6.1). In this stage, the air path must cross the UFRV, responsible for damping the motion, and, to do so, the 5/2 valve must be switched. After the peak knee flexion during the loading phase, the directional valve returns to the original position, making the system transparent. Note that the directional valve must have two blocked ports so that air does not leave the system. Although such valve configuration behaves as a 3/2 valve, that cannot be used, as port 3 is not accessible, unlike a 5/2 valve, where all ports are available for connections.

Table 6.1 summarizes the system resistance or transparency depending on the actuator's direction of motion (extending or shortening) and the state of the 5/2 valve (active or inactive).

	5/2 state	
Actuator motion	Inactive	Active
Extending (B-A)	Transparent	Transparent
Shortening (A-B)	Transparent	Resistance

Table 6.1: Inactive and active refer, respectively, to the normal position and the position when the solenoid is activated. The actuator direction of motion is characterized by the air flow direction, A-B or B-A, where the first letter indicates the source chamber and the last the destination chamber.

In the event of lack of power (5/2 is inactive), for safety reasons, the user's locomotion must not be affected. For that purpose the device only resists motion when the solenoid from the directional valve is activated.

6.2 Actuator Selection

The methodology to select the actuator dimensions and internal pressure were based on the hypothesis of the actuator's chambers being completely isolated from each other, having then a pneumatic spring. Moreover, this spring can be analyzed as an adiabatic system because the K1 region accounts roughly for 12% of the gait cycle, lasting a few hundred of milliseconds [34], time in which the effects of thermal dissipation through conduction and convection are negligible.

The adiabatic pressure evolution in a chamber is given by equation 6.1.

$$P_2 = P_i \left(\frac{L_{ic}}{L_c} \right)^{\gamma} \tag{6.1}$$

P_2 refers to the air pressure in the compression chamber, whose length is L_c. P_i and L_{ic} represent, respectively, the initial pressure and initial chamber length. γ is the adiabatic constant, which for air can be considered 1.4 [28].

The installed pressure will then produce a force proportional to the chamber's area, which will then cause a moment in the knee joint. The main goal is to approximate this moment of force to the biological muscle torque in the knee during the loading phase, so that less energy is wasted by the muscles. However, first, it's necessary to evaluate the

stroke of the actuator, that will depend on where it is attached, and then estimate the required chamber area as well as the initial pressure, P_i.

A limiting value for the minimum stroke (St) of the actuator can be found considering the model presented in figure 6.3. The actuator is connected to the thigh and shank along the axis created by straight lines joining the hip-knee and knee-shank joints. The top end of the actuator is fixed with a distance Xk from the knee. The bottom end is Xs distant from the same joint. Finding the minimum stroke consists in determining the maximum length variation of the actuator during the gait cycle.

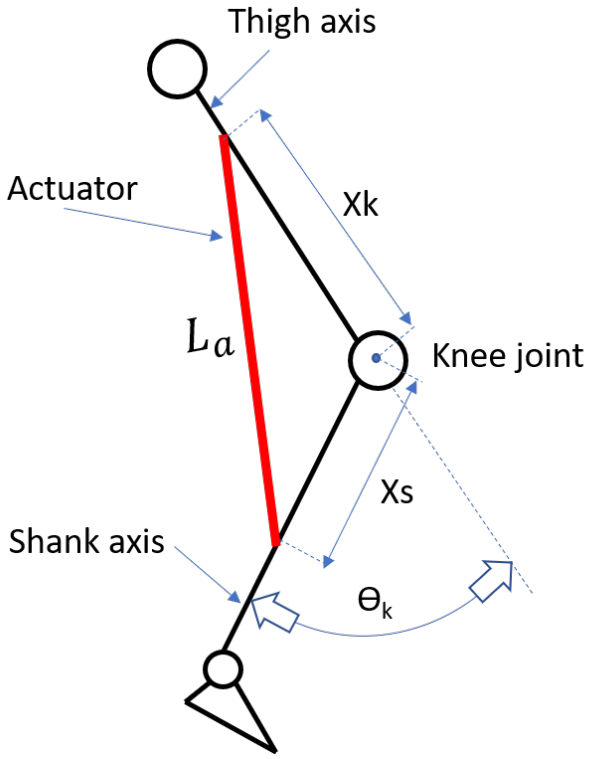

Figure 6.3: Simple model to determine the actuator minimum stroke.

The actuator length, La, can be defined with respect to Xk, Xs and the knee angle θ_k by applying the law of cosines, as in equation 6.2.

$$La^2 = Xk^2 + Xs^2 - 2 * Xk * Xs * cos(\pi - \theta_k) \tag{6.2}$$

So considering a maximum knee angle, $\theta_k Max$, of 70°, St is equal to:

$$St = Xk + Xs - \sqrt{Xk^2 + Xs^2 - 2 * Xk * Xs * cos\left(\frac{\pi - \theta_k Max * \pi}{180}\right)} \tag{6.3}$$

Evaluating the evolution of this parameter, with Xk and Xs comprised between 100 and 500mm, generates the surface presented in figure 6.4.

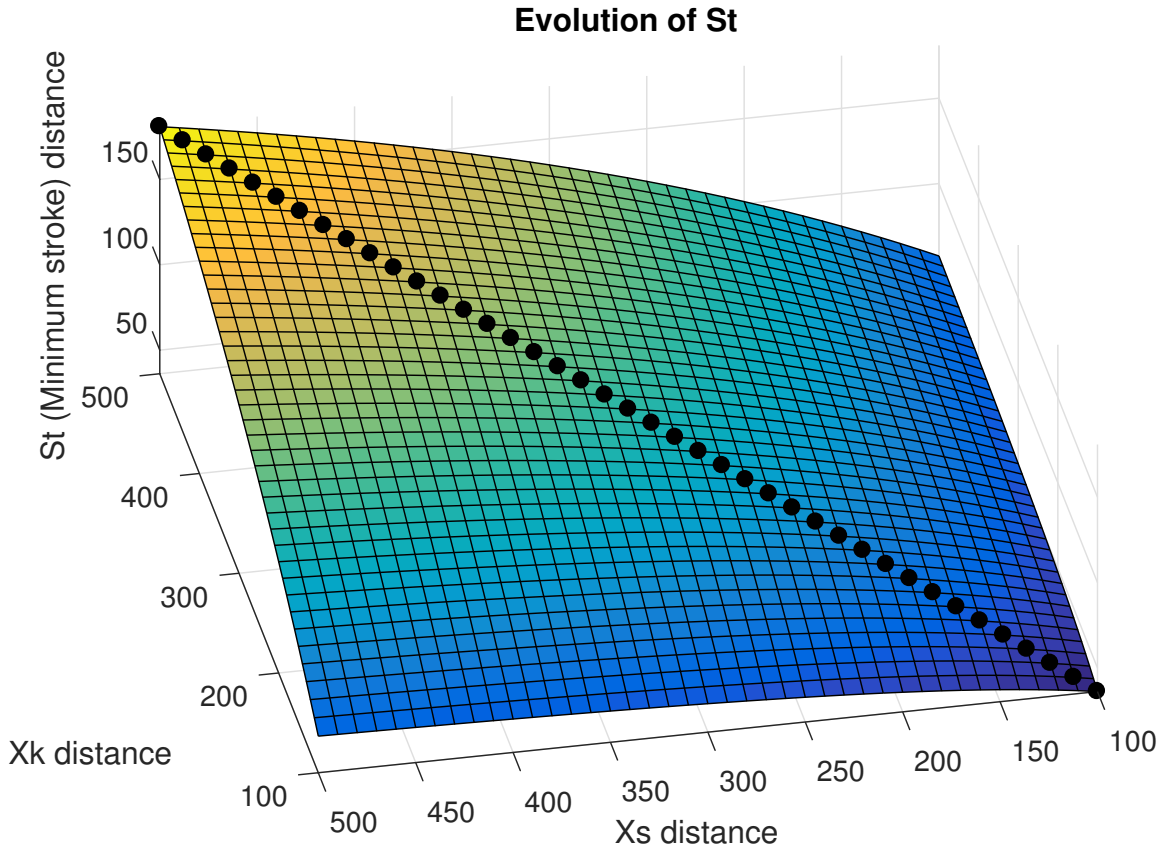

Figure 6.4: Minimum actuator stroke evolution. The black dots indicate the maximum evolution of St.

As one can see, St assumes higher values when Xk and Xs are equal (black dots in the figure above).

Now that the stroke dependency on Xk and Xs is well defined, the next step requires an actuator to be chosen, and knowing its stroke values, Xk and Xs can be set. These two variables are essential as they dictate the pressure evolution inside the actuator when it behaves as a pneumatic spring. In fact, the pneumatic spring consideration is just a simplification to find an appropriate internal pressure. In reality, any pressure curve evolution will be always below the spring-like behavior because of the air flow through

the restrictor valve. One can see a pneumatic spring as a restrictor valve with infinite flow resistance.

Several through-piston-rod pneumatic actuators from *Festo*, were considered, having a stroke (St_A) of 50, 75, 80, 100, 125, 150, 160, 200, 250, 300, 320, 400 and 500mm. The actuators chosen have a chamber outer diameter (D_{ext}) of 32mm, a 12mm rod diameter (D_{rod}) and a maximum pressure operation of 10bar and an effective chamber diameter of 30 mm. [10]

Equations 6.4 and 6.5 allow us to calculate Xk and Xs, which are the same, by knowing the actuator stroke, St_A.

$$St_A = Xk + Xs - \sqrt{Xk^2 + Xs^2 - 2 * Xk * Xs * cos\left(\frac{\theta_k Max * \pi}{180}\right)} \tag{6.4}$$

$$Xk = Xs \tag{6.5}$$

The evolution between St_A and the calculated Xk and Xs are illustrated in figure 6.5

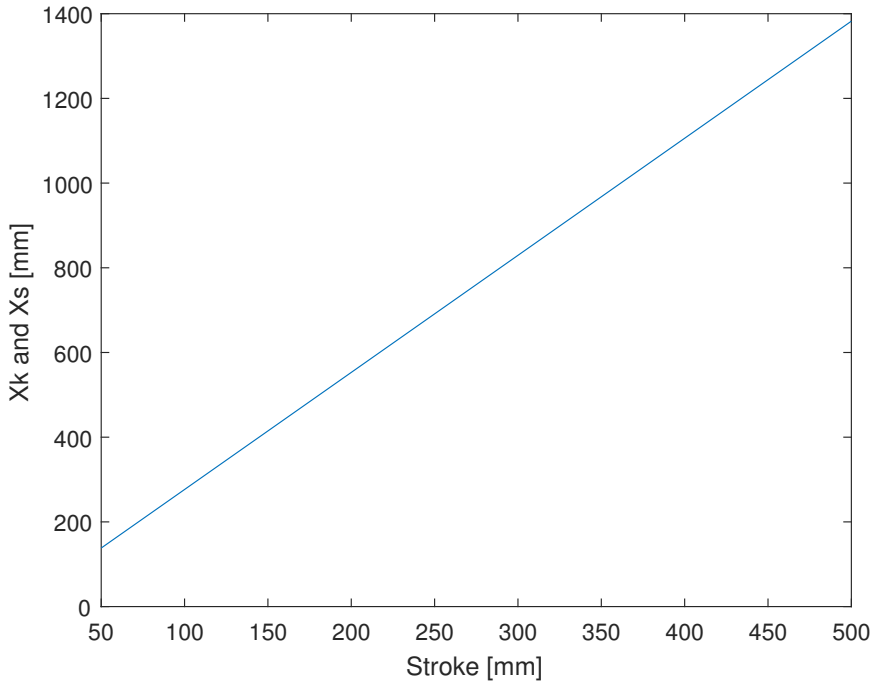

Figure 6.5: Relation between Xk and Xs with St_A.

A visual meaning of the value Xk and Xs can be seen in figure 6.6. The crosses represent the place where the mechanical connections to the limb interface mechanism should be.

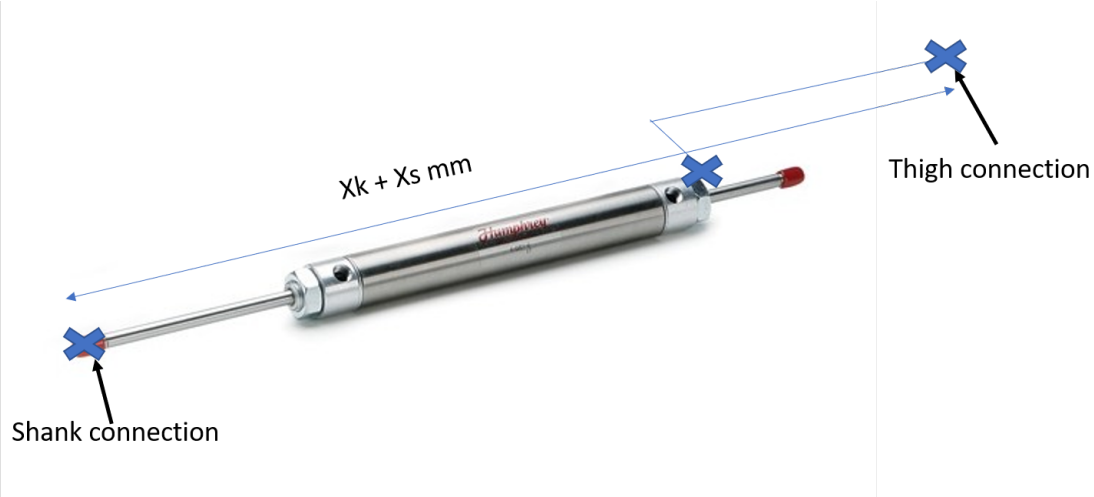

Figure 6.6: Visual representation of the Xk and Xs values. The crosses represent the place where the mechanical connections to the limb interface mechanism should be.

6.3 Initial Pressure

Kinetic and kinematic data from a 70Kg male, walking at three speeds, 0.5, 1 and 1.5m/s were used to predict a reasonable value for the initial pressure, P_i, in the actuator, so that the spring-like behavior approximates the real knee moment. More information about this gait data analysis can be seen in chapter 5.

To compute the initial pressure, P_i, a linear regression was made, in which the input (X) was obtained as below. The output (Y) is simply the knee moment from the given data.

$$X = B_j * A_{eft} * \left(\left(\frac{Lic}{Lc} \right)^{\gamma} - \left(\frac{Lie}{Le} \right)^{\gamma} \right) \tag{6.6}$$

$$P_i * X = Y \tag{6.7}$$

Note that P_i is the coefficient that minimizes the root mean square error between $X * P_i$ and the output Y.

B_j is the lever arm for the actuator force, at the time j, with respect to the knee joint - see figure 6.7. This actuator force is produced by the actuator shortening during the K1 region. Lic, Lc, Lie, Le are the initial length of the compression chamber, the compression chamber length throughout K1 phase, the initial length of the expansion chamber and the expansion chamber length throughout K1 phase, respectively.

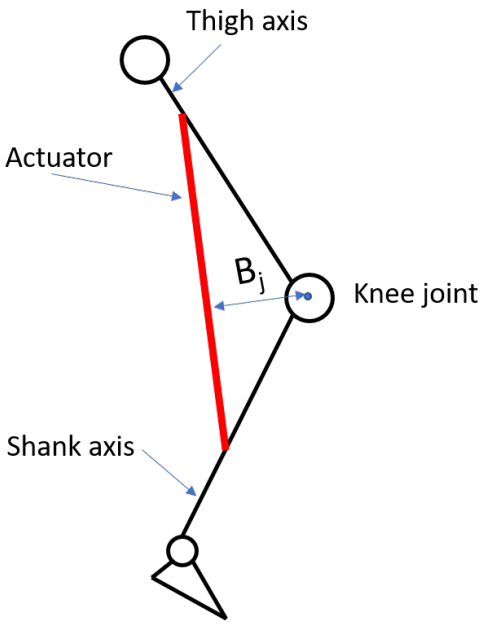

Figure 6.7: B_j is the minimum distance between the knee joint and a perpendicular line to the actuator (line in red).

Such procedure was repeated for each walking speed and stroke value, resulting in the graphs presented in figure 6.8.

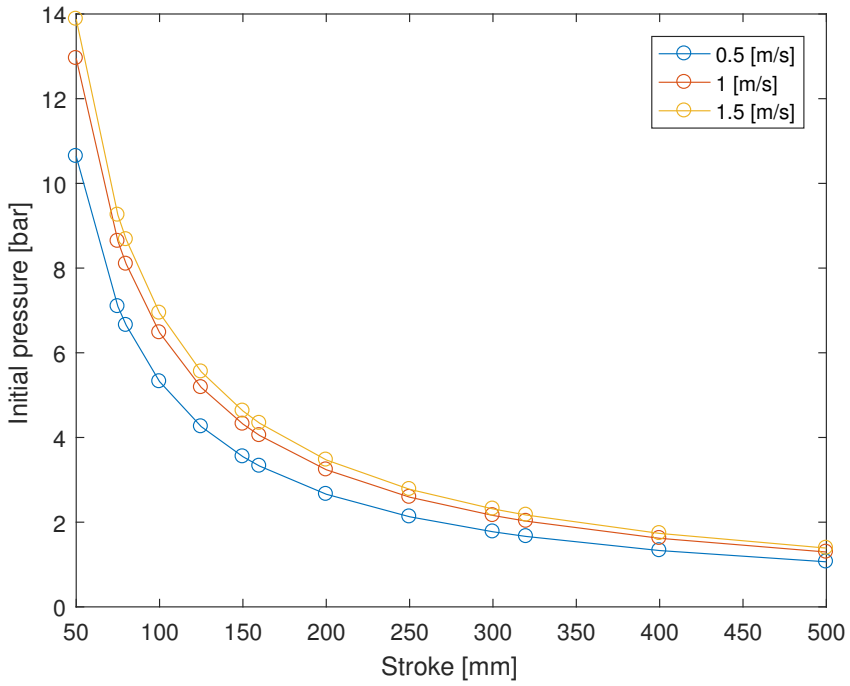

Figure 6.8: Initial pressure values, in bar, depending on the actuator stroke and walking speed.

The actuator limiting pressure is 10bar [10], however, the valves usually have a maxi-

mum limiting pressure of 8bar [12]. With this said, 8 bar must be the maximum allowable pressure in the compression chamber. Figure 6.9 indicates the maximum pressure in the compression chamber during the K1 phase.

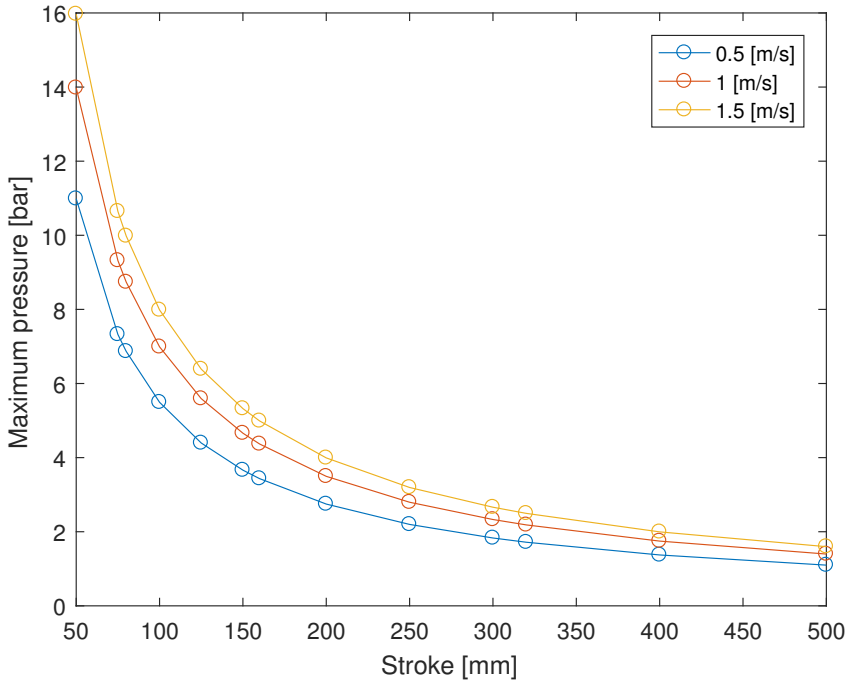

Figure 6.9: Maximum pressure values for the compression chamber, in bar, depending on the actuator stroke and walking speed.

So, based on the figure above, to have the minimum weight possible and still fulfill the required limiting pressure of 8 bar, a stroke of 100mm must be chosen, making Xk and Xs equal to 276,48mm (equation 6.4), and P_i equal to 6.9bar (figure 6.9). The actuator, alone, weights 525.5g. [10]

Figure 6.10 illustrates the difference between the moment created by the selected pneumatic actuator (when performing as a pneumatic spring) and the real knee moment, during K1, for a walking speed of 1.5m/s. As one can see, the actuator mimics fairly well the biological knee moment only assuming higher values in the end of K1, with 4Nm difference between the peaks of the two functions.

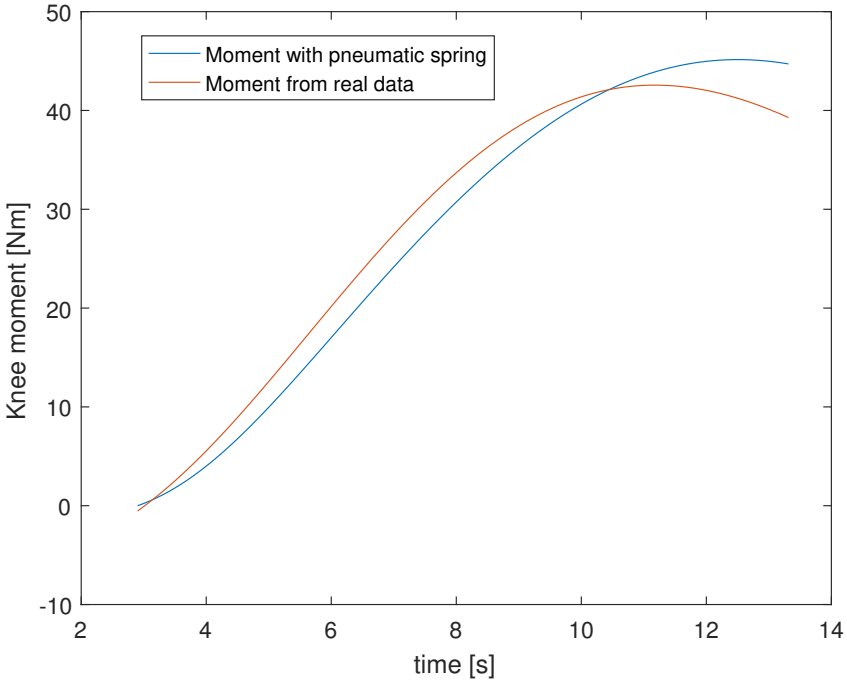

Figure 6.10: Representation of the real Knee moment and the one created by the pneumatic spring, during K1, for a walking speed of 1.5m/s, showing their similarity.

6.4 Flow restrictor valve effect

To evaluate the effect of the UFRV, *Simscape*® was used to emulate a through-piston-rod pneumatic actuator, whose chambers are connected by a flow valve that can change its hole size according to an input block, explained later. Figure 6.11 illustrates the block diagram, built to obtain the simulations, where the colors identify some relevant components, as explained in the caption. Two pneumatic actuators were used because each one represents a chamber, whose area (A_{eft}) is given by equation 6.8

$$A_{eft} = \frac{\pi \left(D_{ext}^2 - D_{rod}^2\right)}{4} \tag{6.8}$$

$$D_{ext} = 30(mm) \tag{6.9}$$

$$D_{rod} = 12(mm) \tag{6.10}$$

Regarding the actuator velocity profile, this was obtained taking the derivative of the chamber position, using an actuator with a stroke of 100mm and the knee angular data for a walking speed of 1.5m/s. Both position and velocity profiles are shown, respectively, in figures 6.12 and 6.13.

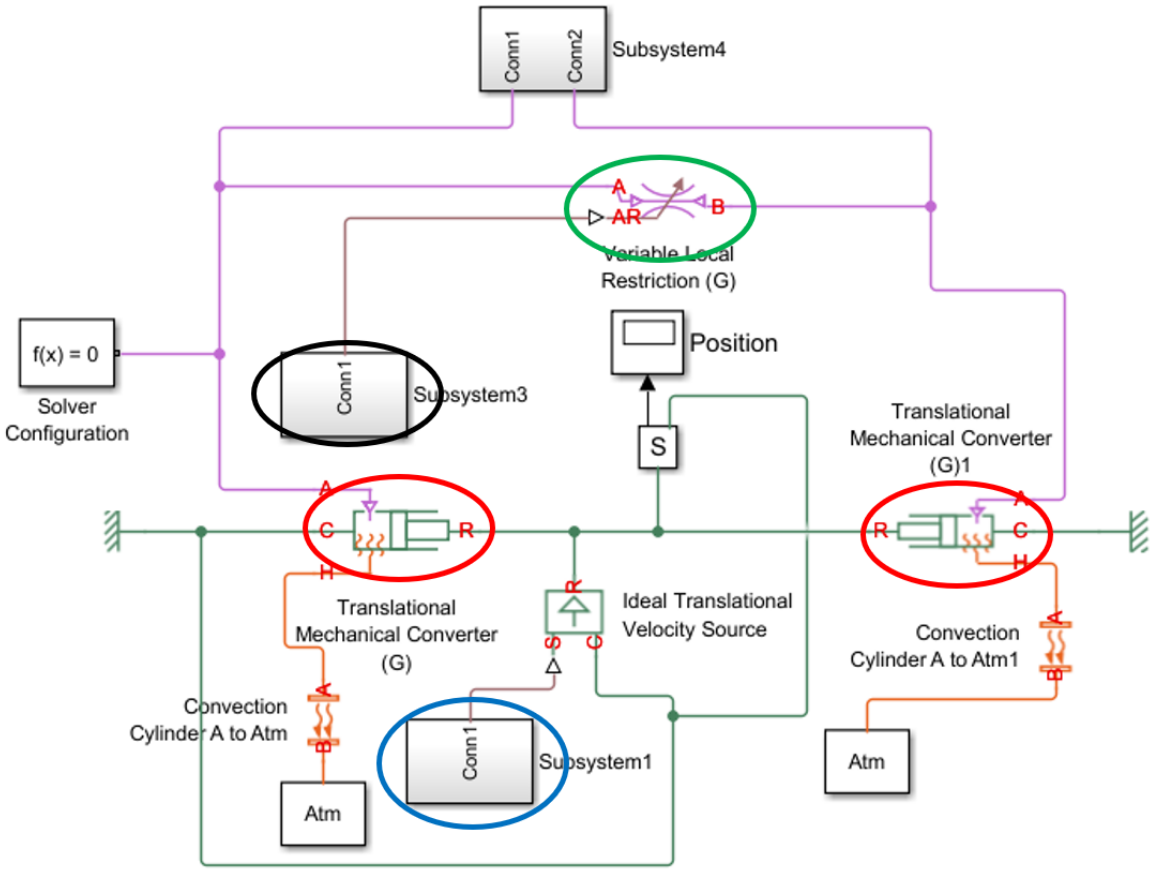

Figure 6.11: Simulink® diagram. The block's color code is the following: Red: Pneumatic actuator; Blue: Actuator velocity profile; Green: Variable restrictor flow valve; Black: Restriction area profile of the valve.

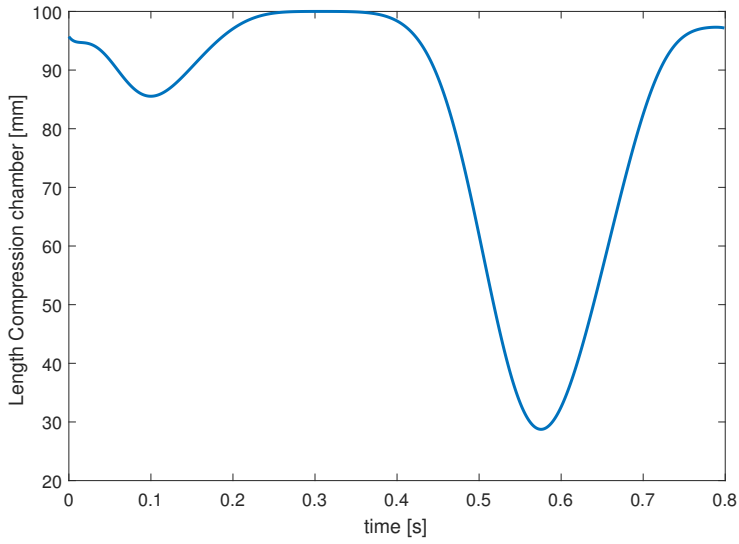

Figure 6.12: Chamber length evolution with time. When it increases, it means the actuator is stretching, and vice versa.

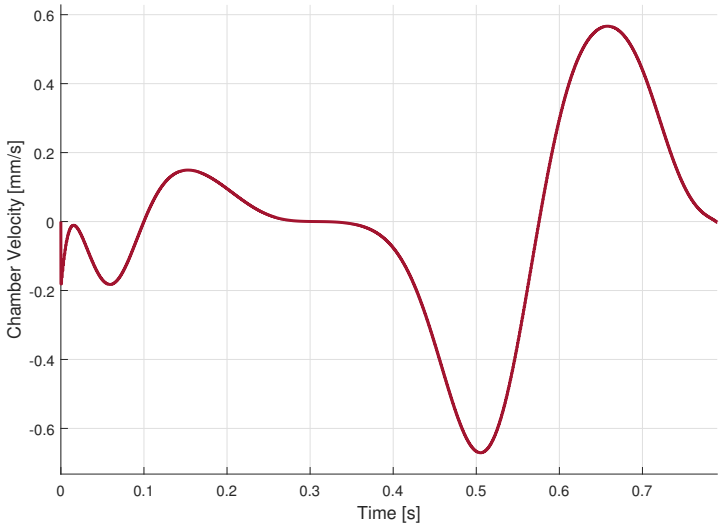

Figure 6.13: Velocity profile of the chamber over time.

As for the valve, marked with the green circle, its cross section area can change with time according to the input signal in the port AR. That signal comes from the block signaled by the black circle. To simulate the device's transparent and resistant state, this profile's area is alternated between two values, A_{max} and A_{def}, depending on the gait cycle stage. Moreover, A_{def} only occurs during K1, when energy must be dissipated, corresponding to the activation of the 5/2 directional valve. Throughout the rest of the gait, the variable local restriction has an area of A_{max}, corresponding to the normal position of the directional valve. Values for these areas can be found in equations 6.13 and 6.14.

$$D_{Max} = 4.40(mm) \tag{6.11}$$

$$D = [0.1 \quad 0.5 \quad 1 \quad 1.5](mm) \tag{6.12}$$

$$A_{max} = \frac{\pi D_{Max}^2}{4} = [0.0079 \quad 0.1963 \quad 0.7854 \quad 1.7671](mm^2) \tag{6.13}$$

$$A_{def} = \frac{\pi D^2}{4} = 15.2053(mm^2) \tag{6.14}$$

0.0079 0.1963 0.7854 1.7671 The value D_{Max} was chosen as half of the actuator hole port diameter, which has a G1/8 thread (8.8mm). [11] Four values for D were tested to understand its effect in the motion resistance.

Other parameter, the coefficient of discharge, Cd, was required due to its relation to the mass flow rate through the valve. Such coefficient accounts for the mechanical energy

losses [28] and depends on the valve design. The mass flow rate in compressible fluids through an orifice is given by the equations below [27].

$$\dot{m}_t = C_d \frac{MaA_{val}P_i\sqrt{\gamma/RT_0}}{[1+(\gamma-1)Ma^2/2]^{(\gamma+1)/2(\gamma-1)}}, \quad if \quad Ma < 1 \tag{6.15}$$

$$\dot{m}_t = C_d A_{val} P_i \sqrt{\frac{\gamma}{RT_0}} \left(\frac{2}{\gamma+1}\right)^{(\gamma+1)/2(\gamma-1)}, \quad if \quad Ma = 1 \tag{6.16}$$

Where Ma, T_0, A_{val} and R are, respectively, the Mach number, the initial chamber temperature ($293 Kelvin$), the valve area, either A_{max} or A_{def}, and finally the gas constant (for air $296.8 JKg^{-1}K^{-1}$).

For the Discharge coefficient, C_d, of the restriction valve, a value of 0.61 is considered, which is typical for Orifice Plates, geometry that approximates the restriction valve. [7]

To better approximate the model to an adiabatic behavior, the convection coefficient to the atmosphere was set to a value of magnitude $1 * 10^{-10}$, so almost null, not allowing energetic losses.

The simulation results for the different values of D, equation 6.12, are presented in figure 6.14 where the output is the knee moment provided by the pneumatic system.

As expected, as the flow valve diameter decreases, the torque exerted by the actuator approaches the one provided by the knee muscles, figure 6.14. Choosing a value of 4.4mm for D_{Max} was enough to allow a device transparency, meaning the resistance to motion is almost imperceptible. This statement is proved by the small knee moment delivered by the actuator in all regions except K1. However, D_{Max} value was not based in any specific datasheet because the opening area of a 5/2 directional valve was not found, so a reasonable value was attributed.

Naturally, the model here presented is somehow simplistic and, for more accurate results, all the pneumatic circuit (figure 6.1) should be modeled as well as all the connection ports between all components. Nevertheless, such simplification allows us to verify the likelihood of the device's good performance, in case of no air leaks.

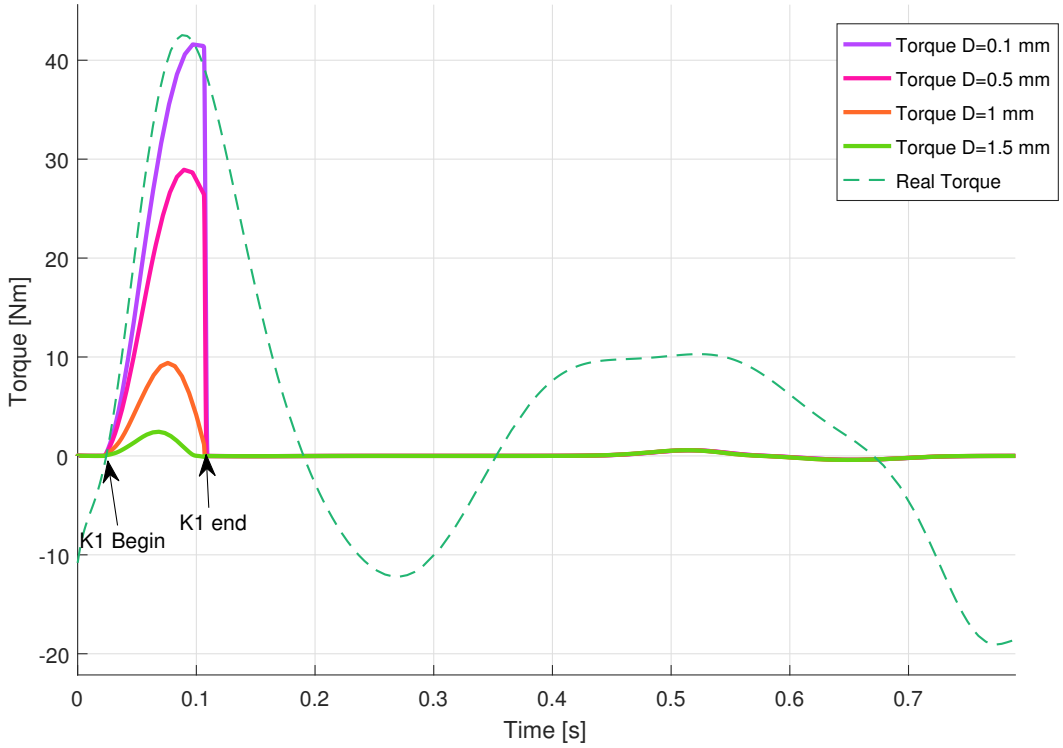

Figure 6.14: Comparison between the real knee moment, and the one provided by the actuator for different opening diameters of the restriction valve.

6.5 Conclusions

The results obtained seem to support this solution as the mechanism allows for a good individual adaptability due to the regulated UFRV, and offers a moment close to the biological knee. However, one main problem is the air leaks that can jeopardize the all system. These leaks may occur in the pneumatic connections with the other components, and also during the directional valve transition that in between states may not be properly sealed. Moreover, the selected actuator only, weights 525.5 grams overcoming the stipulated limit in the *Goals* section. Both reasons lead to the search of other solution.

To actually verify how critical the air leaks are, and verify if the circuit behaves the desired way, experimental tests had to be made.

In alternative, to avoid such leaks, a custom actuator had to be designed so that in its rod, the developed pneumatic circuit would be incorporated. An example of a flow valve integration can be seen in [27].

7. Solution 2 - System based on a commercial rotary damper

This chapter reports the second solution developed to dissipate the knee energy during the loading phase. For that, a commercial rotary damper was chosen based on the results reported in the chapter 5, and the theory of section 2.3.1. The use of a rotary instead of a linear damper was motivated by the simplicity and compactness it brings. In fact, the performance of the linear device would depend, for example, on where it is attached in the thigh and the shank - see figure 6.3. Moreover, the components of a linear device have a larger span over the leg, taking more space than a rotary damper. Space is, indeed, an important factor as the device is thought to be applied, in the future, to other joints.

The system here designed also accounts for a custom dog-clutch and a possible state machine, capable of controlling the (de)activation of the first. Throughout the chapter, the main components of the device are presented, as well as their function and calculation behind. Finally, results of experimental tests done to the damper are shown. These tests intend to verify whether the chosen damper suits its application.

7.1 System overview

The device presented has six main components. First, there is the **damper**, which, as referred previously, is responsible for the energy dissipation. Its selection and behavior under different velocities are treated later on the chapter. However, the damper must have some kind of (dis)enabling-in-series mechanism, which in the end controls whether the device is dissipating energy or behaving transparently. For that, a customized **unidirectional Dog-clutch** was used, whose (dis)engagement is commanded by an **hold-and-pulse solenoid**. Meanwhile, this last component has to be controlled by a **microcontroller**, which receives the data from the **encoder** (reads relative angle between the thigh and shank) and acts according to it. All these electronic components must be powered by a **battery**. Lastly, there is a **spring** connected in parallel to the damper, whose function is to ensure its return to the original position. Such return is necessary because the damper has a limited range of motion, so if not returned to the original position, after a certain number of cycles it would reach its limit, blocking fur-

ther motion. Then, the damper is not the only dissipating element because the spring also contributes to that effect, although its stored energy is not inserted at the knee but instead used to move the damper backwards to the neutral position.

The device correct functioning will be explained below: Initially, before the heel strike, the clutch is disengaged, so the shank rotates relatively to the damper. A simple state machine is then used to detect critical points during the gait cycle. This algorithm tries to compensate the solenoid activation time, firing it before the actual heel strike in order to make the clutch engagement easier. The solenoid firing brings the two plates of the clutch together, causing an overlap between the teeth, that forces the damper and spring to rotate with the shank, thus creating a resistance to the knee flexion motion. The disengagement occurs in the next zero angular velocity point, detected through the encoder signal. From this point on, the damper does not interfere in the gait cycle and, as said before, its initial position is set by the parallel spring. Then, the next point of interest is the peak knee angle at the swing phase, detected again by a zero angular velocity and a rising angle evolution. After that, as soon as the encoder detects other null velocity, means a heel strike has occurred and other cycle may begin.

Two images illustrate the device and the main components described above - see figure 7.1 and 7.2. Only the microcontroller and the electric circuit are not represented in the 3D model, but will be shown later.

The exterior connections of the device to the shank must be done trough the shank connector, that has two holes for bolt and nuts fixations. The interface with the thigh, on the other hand, must be done trough the damper flange, which contains 4 nuts to hold that mechanism. As for the pneumatic solution, details on the limb connection elements were not investigated for this thesis because it was not a priority study, given that several solutions already exist today [3, 32, 33] that may be adjusted for this case, in a future work.

The external housing, besides protecting the components, specially the electronic ones, also serves as an anchoring element for one part of the encoder, so it can read the relative angle between the shank and thigh. The two parts comprising the housing connect each other trough bolts and nuts, being also connected, in the same way, to the damper flange (linked to the thigh) and the encoder electronic reader. In the end, this encoder part follows the thigh motion and the other (magnetic ring) rotates with the shank, allowing to read the relative angle of these body segments.

Regarding the encoder and solenoid positioning, these components should be on the same side, whether on the right or left of the clutch system, to make the electrical

connections to the microcontroller and battery easier.

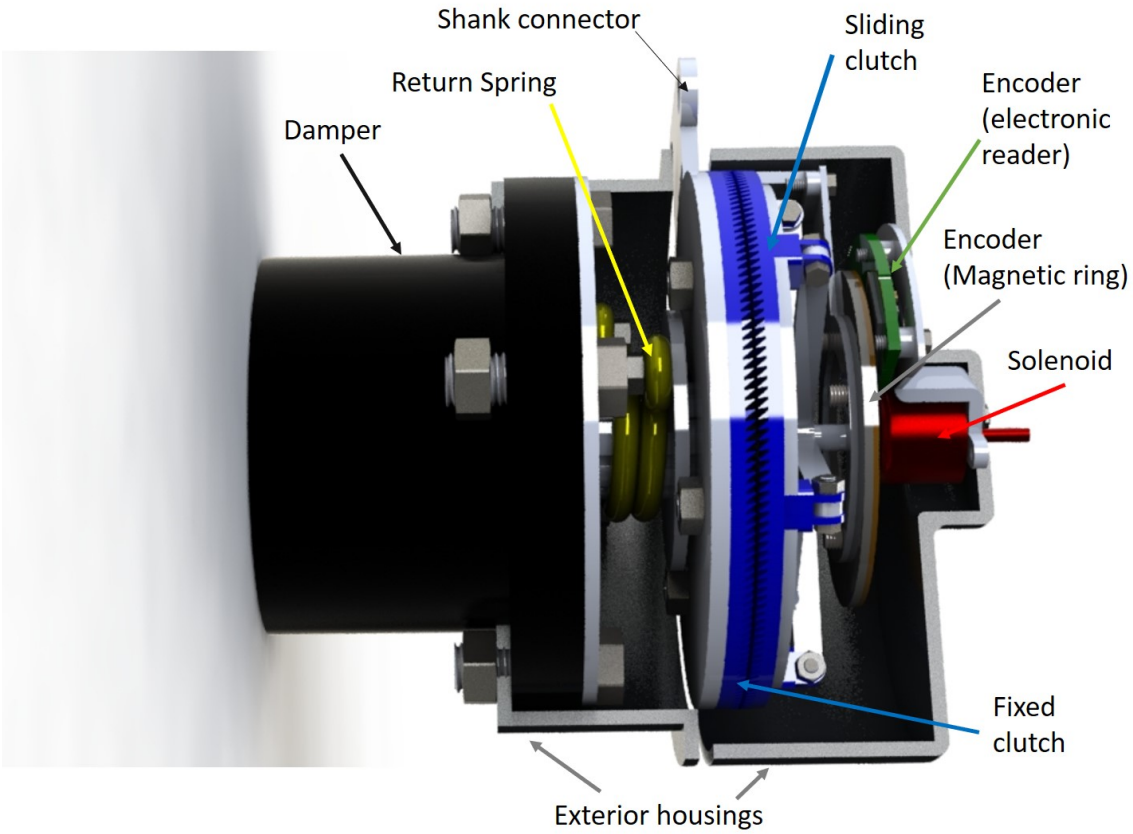

Figure 7.1: Main components identification.

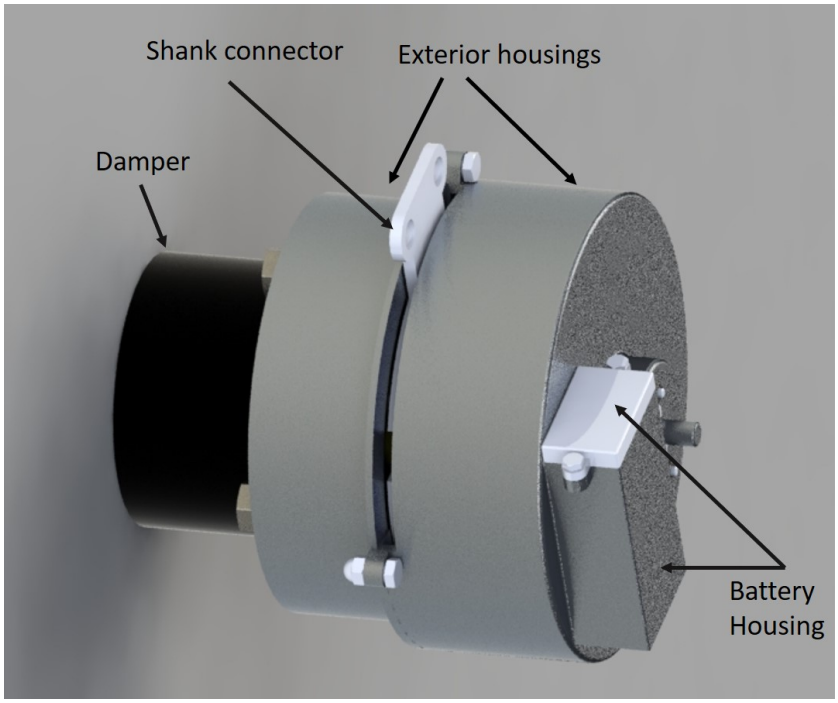

Figure 7.2: Battery housing location.

7.2 Damper Selection and characterization

According to chapter 5, the damper should have a damping coefficient ranging from 5 to 15Nm.s/rad. Besides this, other two criteria must be applied, being the first the damper weight, which must be as low as possible, and the last the maximum holding torque. Based on figure 2.9, a normalized knee moment value of 0.45Nm/(Kg.m) (corresponding to a walking velocity of 2m/s) will be used as the peak knee torque. Considering a person of 80Kg and a leg length of 1 meter the maximum damper holding torque is 36Nm. After applying a safety factor, S_{dMT} of 1.5, the maximum torque, T_{DMAx} is set to 54Nm.

A rotary damper was chosen from the the following list, see figure 7.1. [44]

Table 7.1: Results for the damping test with zero turns on the restrictor. V_{out}, T_{sens}, C_{damp} are respectively the motor output velocity, the torque obtained by the sensor, and the computed damping coefficient for each output velocity.

Clockwise	Anti-clockwise	Clockwise and anti-clockwise	Torque	Opening angle	Weight
			Nm	°	g
WRD-H-2515-R	WRD-H-2515-L	WRD-H-2515-C	10	180	80
WRD-H-3015-R	WRD-H-3015-L	WRD-H-3015-C	14	180	80
WRD-H-4025-R	WRD-H-4025-L	WRD-H-4025-C	40	180	352
WRD-H-6030-R	WRD-H-6030-L	WRD-H-6030-C	110	180	767

Clockwise and Anti-clockwise refer to the direction where the damper offers the most resistance. So, in the case of a clockwise damper, the most resistance will be felt in this direction. However, the other is not completely free, there is always some resisting torque. The table above also shows the angle range of motion, weight and maximum torque. As one can see, only the last model supports the limiting torque of 54Nm. However, its weight is considered too much. Having said this, the model WRD-H 4025 [44] was selected, although it violates the maximum torque requirement. Nevertheless, the components' dimensions will be obtained based on the 54Nm limitation. Other important factor is the angular range of motion, that must be higher than the difference between peak knee angle during stance and the angle at heel strike. This difference will be considered as 20° based on figure 5.1 in the top left.

The damper selected has the possibility to change the damping coefficient by means of a screw, however, the only information available from the company is a test made at an angular velocity of 1rad/s in maximum damping capacity. Figure 7.3 illustrates such torque curves over the angle.

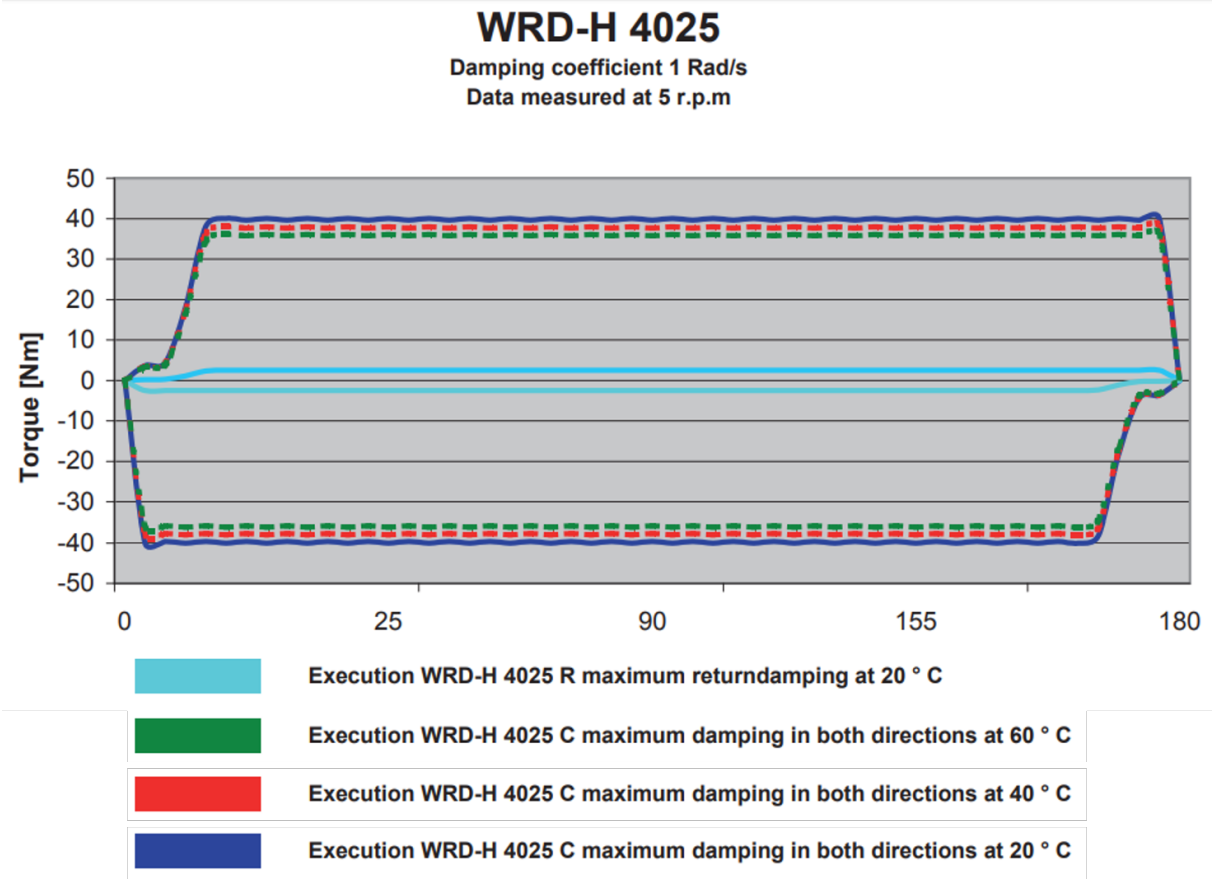

Figure 7.3: Torque tests at the maximum damping with a rotation speed of 1rad/sec. This test was performed at three different temperatures, 20, 40 and 60°.

With this information, the damping coefficient can be estimated as $40Nm.s/rad$, which surpasses the limit of $14Nm.s/rad$ obtained before (section 5.2). Yet, the value of 40 is estimated at maximum damping capacity and no other information is given for other damping regulation values and rotational speeds. That lack of information motivated the realization of some tests to the damper in order to better understand its behavior.

7.2.1 Experimental Tests and results

With the objective to properly characterize the damper over some ranges of operating velocities and damping regulations, a test bench was set up, comprising a DC motor, the testing damper, and a torque sensor. The motor rotates the damper shaft, originating a resisting torque measured by the torque sensor.

The DC motor of 150W and maximum of 7000rpm [26] has a planetary gear assembled with a reduction 1:81 and an optical encoder. Regarding the torque sensor this has a maximum holding torque of 50Nm, with a sensitivity of $12.343Nm/V$ [13].

The tests were done using an open-source software platform SCILAB/SCICOS [1] running on the operative system Ubuntu (8.04) with patched RTAI kernel. CoMeDi drivers allowed interfacing of the control algorithms and the servomotor through one S626 Sensoray I/O board.

The mechanical part of the test rig is presented in figure 7.4.

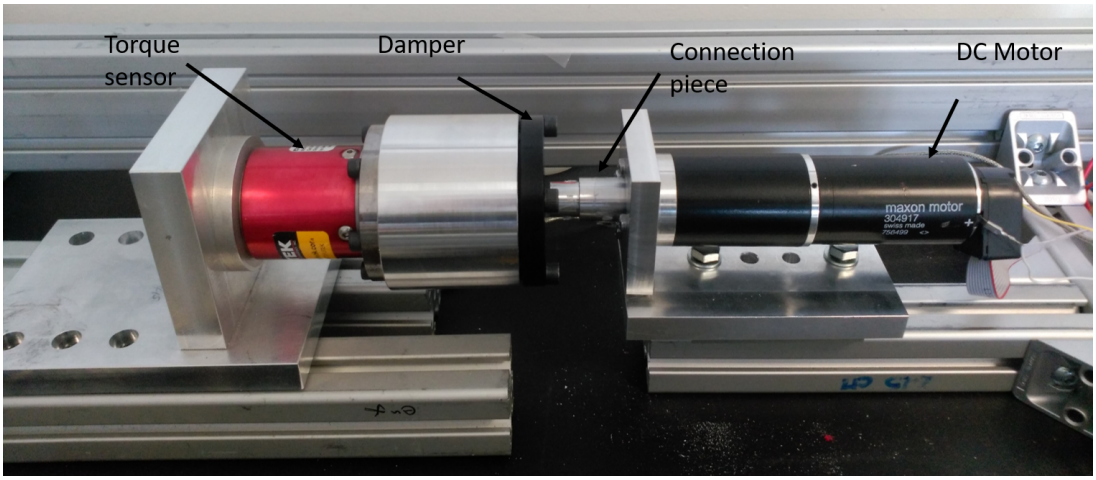

Figure 7.4: Test rig: the motor rotates the damper shaft, originating a resisting torque measured by the torque sensor.

The position of the motor was controlled via a closed-loop control system using a proportional gain. The control architecture is depicted in figure 7.5.

When the step function is activated, two square waves, representing the desired output speed, are also activated. After integrating them, the desired output angle profile is obtained. These waves have symmetrical amplitudes and are shifted in time, so that the motor rotates in one direction, stops and then comes back to the original position with the same speed. The desired position is subtracted to the real one, computed with the encoder information. That subtraction gives origin to the error. Note that the encoder output is digital, so after a numerical conversion such value is multiplied by the inverse of the encoder resolution times the gear ratio, mathematically stated as:

$$K = \frac{1}{E_{reso} * G_{ratio}} \tag{7.1}$$

This error is then inserted in a PID block, that experimentally was found to have a good performance with a P value of 0.035 and the others being null. After the PID block,

[1] http://www.scicos.org/scicosaddtools.html

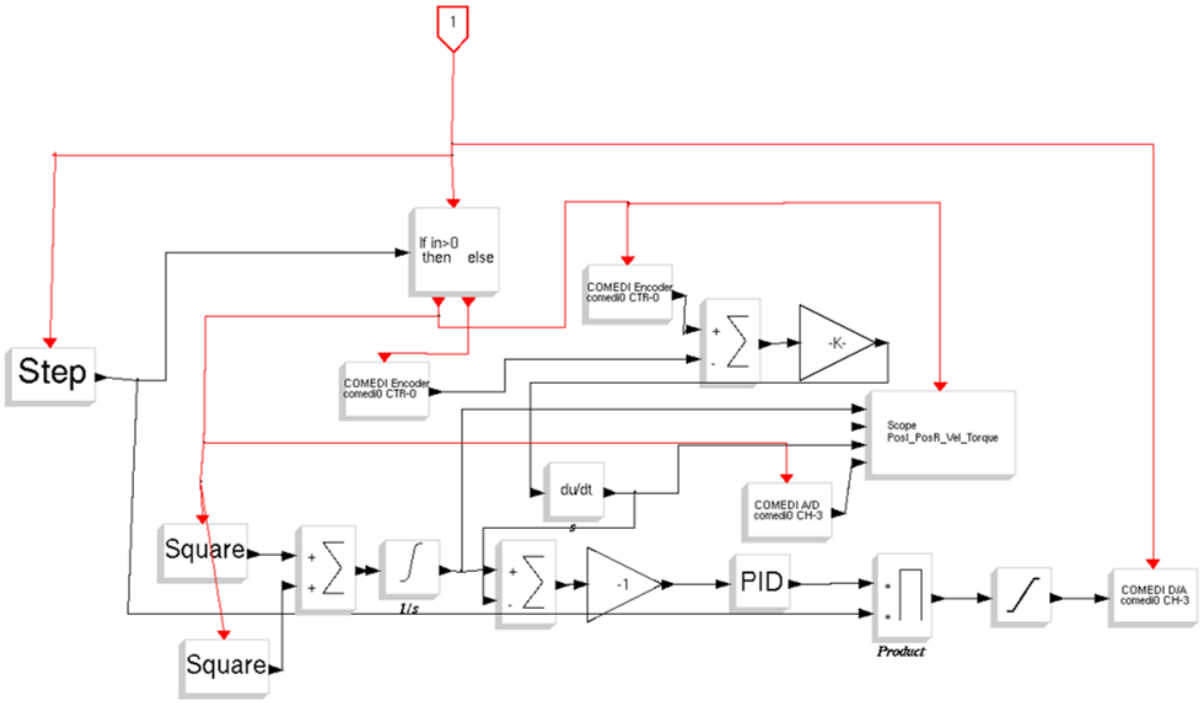

Figure 7.5: Control architecture developed in Sicos.

voltage goes through a saturation block (± 10V) and then the result is converted to an analog signal inserted in the motor to change the output speed.

Three levels of damping effects were tested, by rotating a screw, responsible for this damper characteristic change. The "stages" tested, corresponded to 0, 1/4 and 1/2 turns. Although one full turn was possible, after 1/2 turn the motor was already overloaded and no more tests were performed. For each regulation turn, nine speeds were tested and both the torque signal and the output speed were extracted for further analysis, made in *Matlab*®.

The velocity signal obtained had to be first filtered by a low-pass filter with a cut-off frequency of 1Hz. On the other hand, the voltage from the torque sensor had no significant noise, so this was directly converted to torque using the sensor's sensitivity ($12.343 Nm/V$). Then, for each rotational direction, a region was manually identified where the torque and velocity signals were fairly constant and an average was taken in that interval. Afterwards, the damping coefficient of each turning direction was computed by simply dividing the mean torque by the mean output velocity. Performing a test in two rotational directions offers the advantage of characterizing the damper in the active and free mode, in one single test.

Figure 7.6 illustrates the real and filtered velocity, as well as the torque evolution and the marks that delimit a constant region.

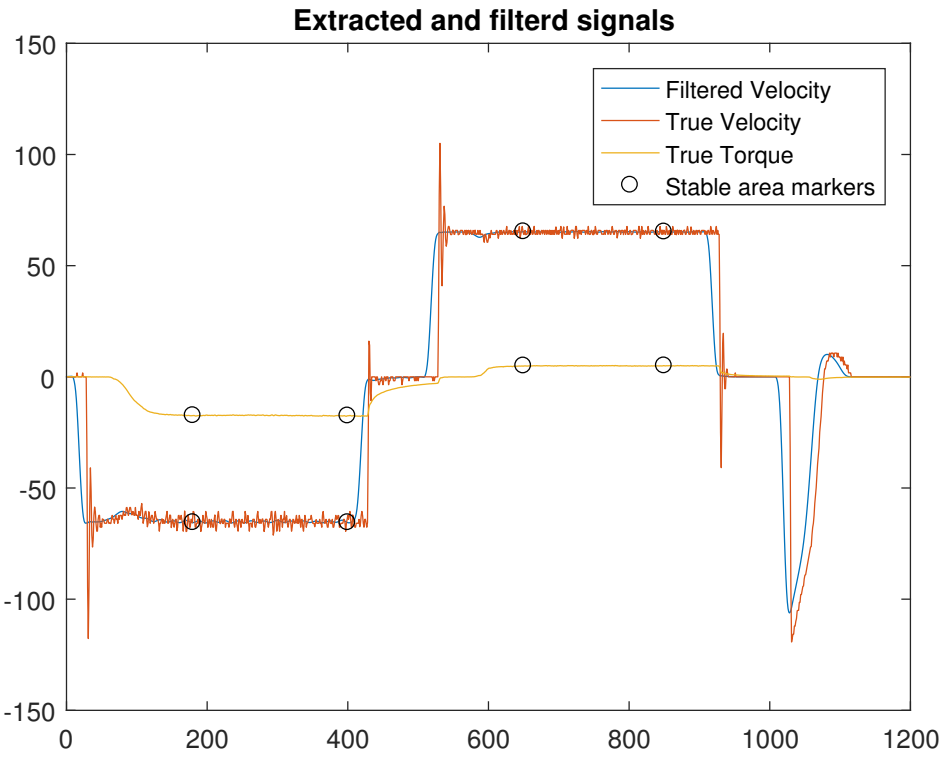

Figure 7.6: True velocity, torque and filtered velocity profiles. The circumference delimits the constant areas where the average was done. The first two bound one rotational direction and the other two restrain the other direction.

The table 7.2 sums up the results obtained for zero turns of the restrictor. On appendix A, other data related to different restrictor adjustments can be found.

Table 7.2: Results for the damping test with zero turns on the restrictor. V_{out}, T_{sens}, C_{damp} are, respectively, the motor output velocity, the torque obtained by the sensor, and the computed damping coefficient for each output velocity.

Target Speed $(°/s)$	$N_t = 0$					
	Active Direction			Free Direction		
	V_{out} $(°/s)$	T_{sens} (Nm)	C_{damp} $\left(\frac{Nm*s}{rad}\right)$	V_{out} $(°/s)$	T_{sens} (Nm)	C_{damp} $\left(\frac{Nm*s}{rad}\right)$
10	9.67	6.67	38.26	9.69	1.35	7.98
20	19.63	9.77	28.00	19.95	2.30	6.60
30	30.11	11.63	22.22	30.63	3.04	6.00
50	49.13	14.59	16.72	49.92	4.06	4.65
75	75.17	18.14	13.86	75.25	5.24	3.76
100	101.05	21.25	12.18	100.41	6.31	3.74
150	149.22	25.41	9.70	150.04	7.98	3.00
200	201.40	27.14	7.77	201.22	9.27	2.48
300	298.34	26.14	5.00	299.05	10.45	1.95

The results were then fitted to an exponential equation of the form:

$$C_{damp} = a * exp(b * V_{out}) + c * exp(d * V_{out}) \tag{7.2}$$

Table 7.3 identifies each of the coefficient for every damper regulation.

Table 7.3: Exponential regression coefficients for the three regulations values.

	$N_t = 0$		$N_t = 1/4$		$N_t = 1/2$	
	Active Dir	Free Dir	Active Dir	Free Dir	Active Dir	Free Dir
a	38.04	5.16	43.66	6.48	57.11	6.79
b	-0.063	-0.041	-0.06	-0.047	-0.083	-0.068
c	18.85	4.64	21.91	4.51	38.45	5.33
d	-0.0044	-0.0028	-0.005	-0.0026	-0.0075	-0.0036

An example of such curve fitting is presented in figure 7.7 with a zero turn adjustment.

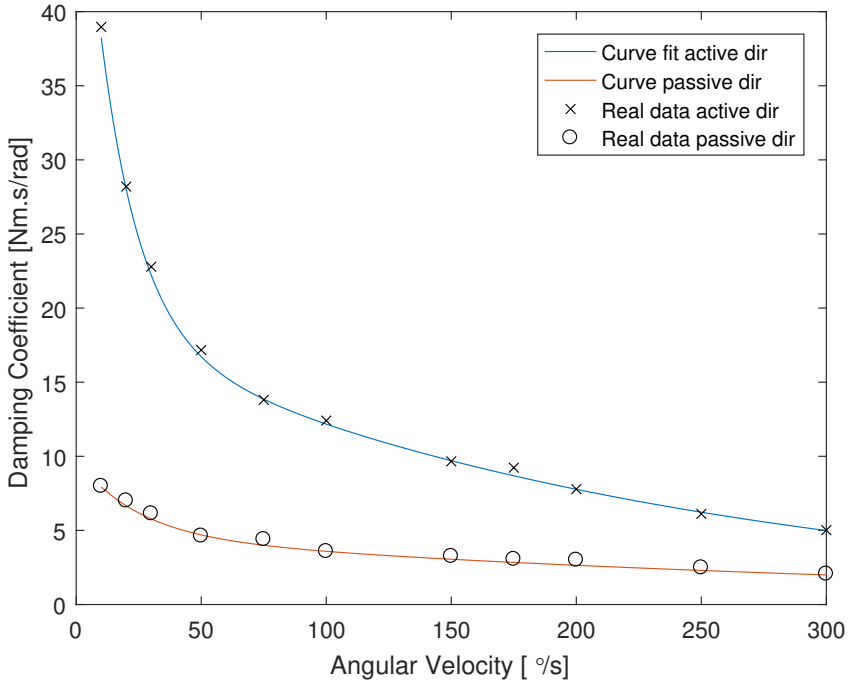

Figure 7.7: Curve fitting for the active and passive directions for $N_t = 0$.

Next, the surface fitting is presented, in figures 7.8 and 7.9. This fitting was done taking into account all the data throughout the different damper adjustments, angular velocities and rotating direction. Such fitting was performed using the curve fitting toolbox in *Matlab*®, and a custom equation was found iteratively, bringing the determination coefficient, R^2, to a value of 0.991 for the active direction and 0.980 for the passive one.

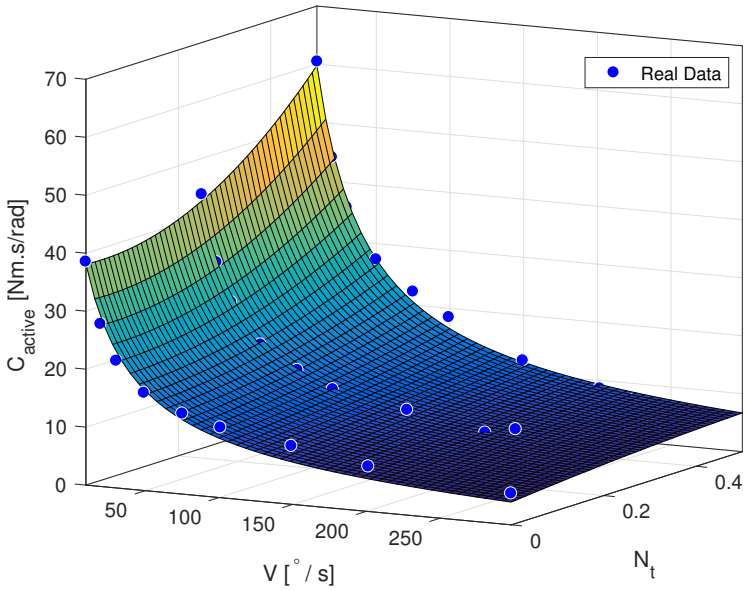

Figure 7.8: Surface fitting for the active direction.

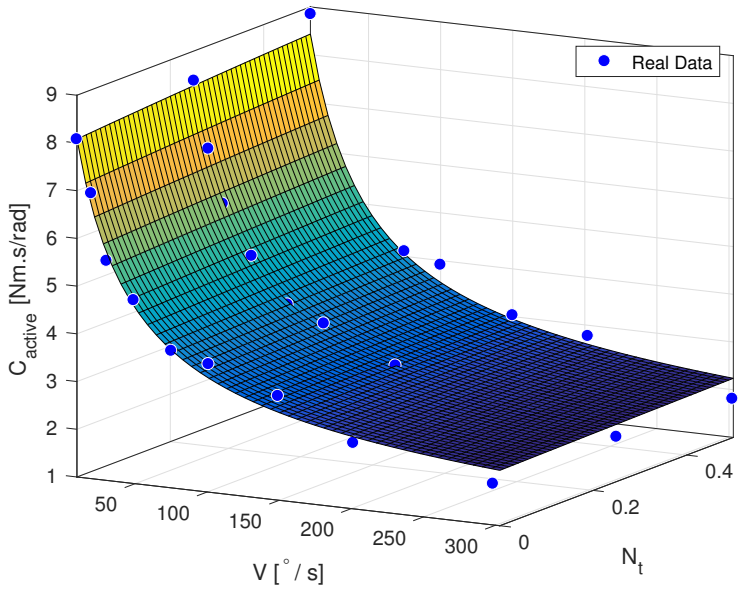

Figure 7.9: Surface fitting for the passive direction.

The resultant equation and coefficients that describe the active and passive surface fits are shown in the equation 7.2.1 and 7.2.1, respectively. N_t and V variables represent the adjustment number of turns and the damper shaft velocity, respectively. The other parameters are simply coefficients determined by optimization algorithms embedded in the curve fitting toolbox.

$$
\begin{aligned}
C_{active} &= \frac{(A * N_t^2 + B * N_t + C)}{(D * V + E)} + F * N_t^2 + G * N_t \\
A &= 227.47 \quad ; \quad B = -32.81 \\
C &= +73.31 \quad ; \quad D = 0.058 \\
E &= 1.362 \quad ; \quad F = -17.92 \\
G &= 10.11
\end{aligned}
\tag{7.3}
$$

$$
\begin{aligned}
C_{passive} &= \frac{(A * N_t^2 + B * N_t + C)}{(D * V + E)} + F * exp(G * N_t) \\
A &= -1.47 \quad ; \quad B = 3.832 \\
C &= 33.53 \quad ; \quad D = 0.127 \\
E &= 3.768 \quad ; \quad F = 1.365 \\
G &= 0.0601
\end{aligned}
\tag{7.4}
$$

Having the mathematical model that describes the behavior of the damper, it is possible to see its contribution during the gait cycle if one imposes an angular velocity obtained from the walking data analyzed in chapter 5.

Considering $N_t = 0$, figures 7.10, 7.11 and 7.12 compare the real knee torque during K1 with the one provided by the damper if this follows the same knee pattern for the three distinct walking velocities (0.5, 1 and 1.5m/s).

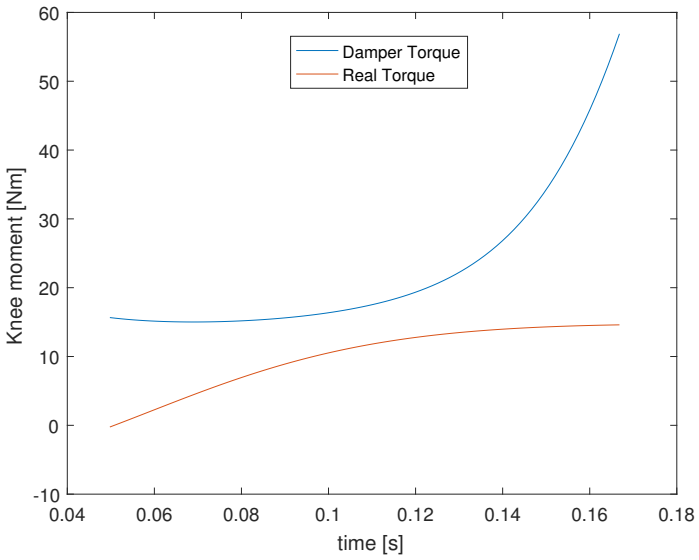

Figure 7.10: Comparison between knee and damper moment at 0.5m/s walking speed.

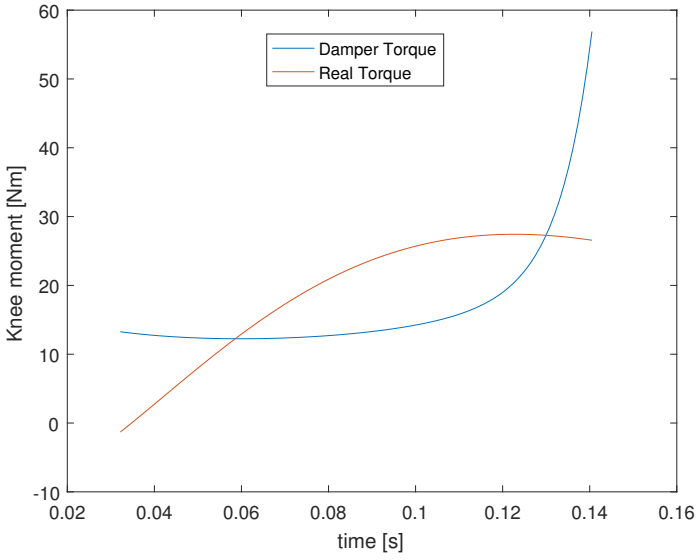

Figure 7.11: Comparison between knee and damper moment at 1.0m/s walking speed.

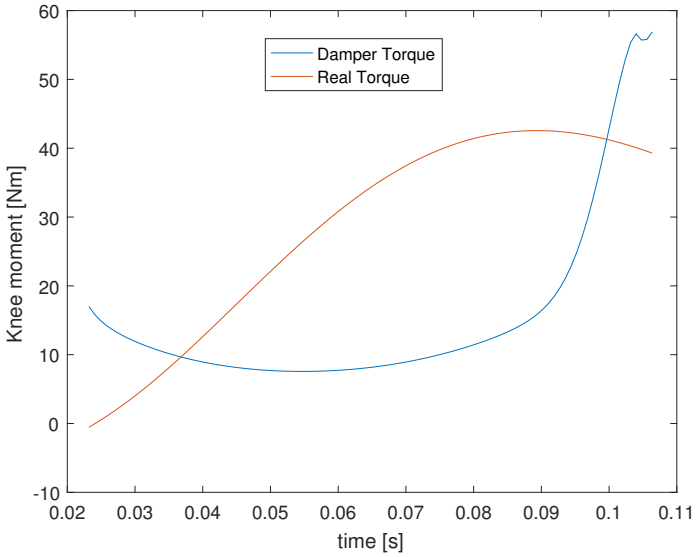

Figure 7.12: Comparison between knee and damper moment at 1.5m/s walking speed.

By looking at the figures above, one can conclude that the damper will alter the normal gait pattern because its resisting moment is higher that the one provided naturally by the muscles in the knee. If below, though, the gait could remain the same or very similar. At the same time, the moment provided by the muscles would decrease, which in fact is the desired situation. However, to access how different the gait would be, experimental tests had to be performed.

7.3 Dog-Clutch

As explained above, the Dog-clutch is the component responsible for making the damper active or transparent. Commercially, there are several technologies, as pointed below [9]:

1. Particle brakes activate an electromagnet whose field affects a ferrous powders that links the rotor to the stator. Particle brakes permit very accurate control of torque, which varies almost linearly with applied current.

2. Friction clutches rely on the application of a normal force, that must be enough to allow friction between the two surfaces to transmit the required power. This force may be provided by air pressure, springs, centrifugal force, permanent or electromagnets.

3. Toothed clutches are similar to friction clutches, however the disk possesses interlocking teeth not relying purely on friction. This solution can withstand significant torque, yet it discretizes the possible engagements angles. Sometimes a sycronizer is needed to ensure there is no engagement at certain angles.

As low power consumption is a requirement for the device in question, both particle brakes and friction clutch are put aside leaving only the tooth clutch technology as an option. In fact, as this is less dependent on friction, lower normal forces are needed. Actually, by changing the teeth geometry - see figure 7.13, this force can be reduced to zero.

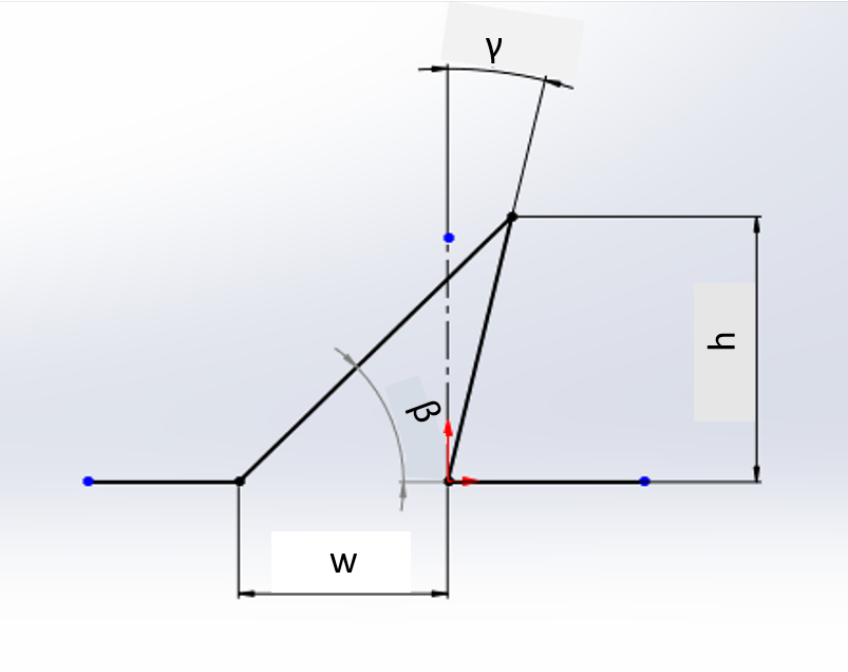

Figure 7.13: Side view of a tooth and it's dimension parameters.

For a rough estimation of the holding torque, a simple model was used based on an isosceles triangular tooth loaded with a concentrated force in the middle section. Equation 7.5 expresses this maximum torque as a function of several parameters explained below. See the deduction in [9].

$$T_{c,max} = \frac{1}{12} \frac{\eta^2}{(2-\eta)\dfrac{w_c^2 * d_c}{h_c} n_c * r_{i,c} * \sigma_{y,AL}} \tag{7.5}$$

η is the engagement fraction, w_c tooth width, d_c tooth depth, h_c tooth height, n_c

number of teeth, $r_{i,c}$ clutch inner radius and $\sigma_{y,AL}$ yield strength of a AA2011 T3 aluminum allow.

The angular resolution was chosen to be 2° giving rise to 180 teeth. There are still three degrees of freedom to be defined, so, as a first iteration, measures were picked based on [9], which depicts a very similar problem to this thesis. The dimensions chosen are:

Table 7.4: Teeth Clutch Measures.

w_c	d_c	h_c	n_c	$r_{i,c}$	γ
1.01mm	5mm	2.5mm	180mm	29mm	5°

Using an aluminum alloy, AA2011 T3 with a $\sigma_{y,AL}$ of 290 MPa [1], $T_{c,max}$ can be computed using equation 7.5 giving a value of 108 Nm, which is two times greater than T_{DMAx}.

Since the actual geometry (figure 7.13) is far from an isosceles triangle, a finite element simulation was performed to better describe the component and its stress distribution. For this purpose, the *SolidWorks* Finite Element Simulation toolbox was used. For the sake of numerical simplicity, only 10 teeth were simulated instead of the 180. The simulation accounted for the two plates whose contact occurred in the teeth using the contact mode of node-surface. The elements were tetrahedral and the boundary conditions can be seen in figure 7.14. Face A is fixed in all directions, face B is fixed only radially and in face C is applied the torque. This amount instead of being 108Nm, as only 10 teeth were simulated, to keep the torque per teeth the same, the moment applied was $T_t = \frac{108 * 10}{180}$. The mesh was refined using the adaptive mesh h-type with a 5 step.

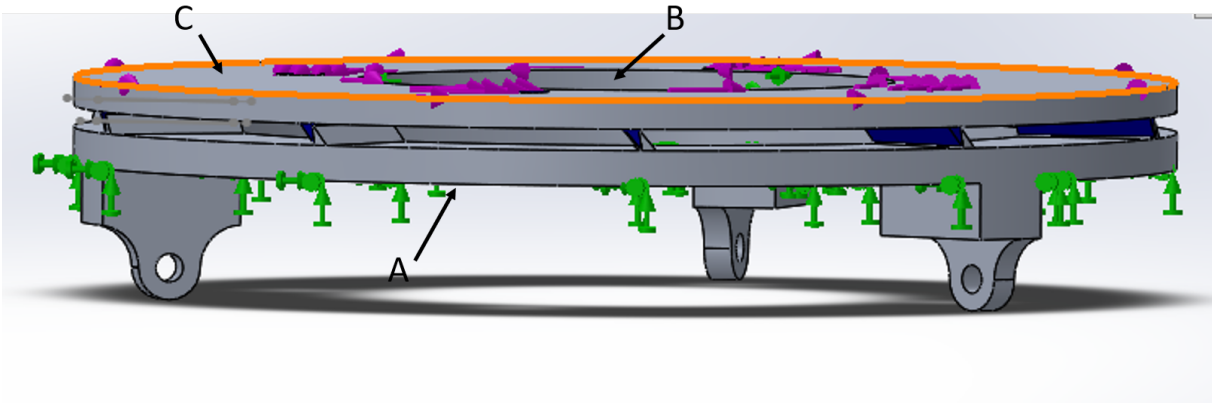

Figure 7.14: Face A: Fixed all directions ; Face B: Fixed radially ; Face C: Torque applied

The teeth geometry was slightly changed, figure 7.15, by adding fillet radius in the

tooth tip and root, avoiding then a big concentration factors.

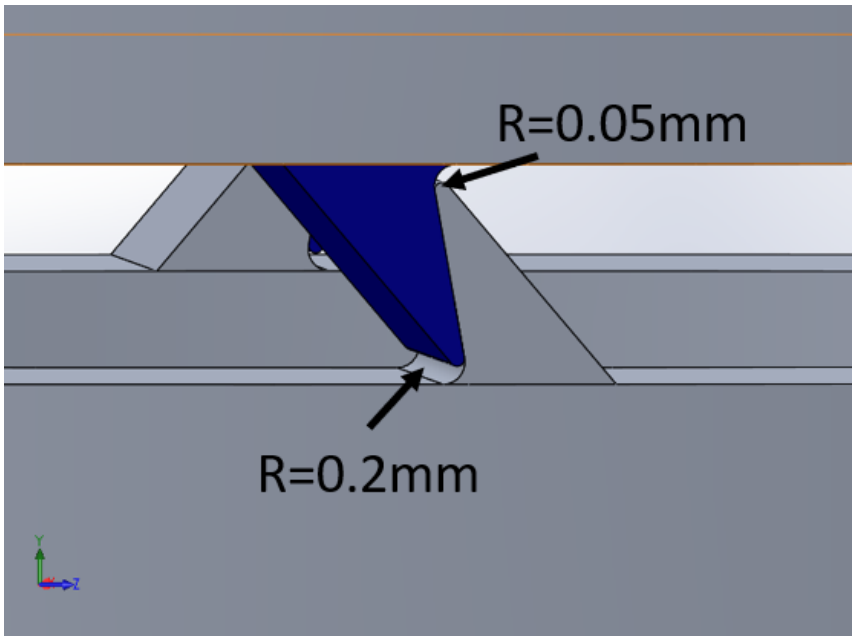

Figure 7.15: Teeth geometry : Fillet radius were included to avoid stress concentrations

The results of the simulations is presented in figure 7.16.

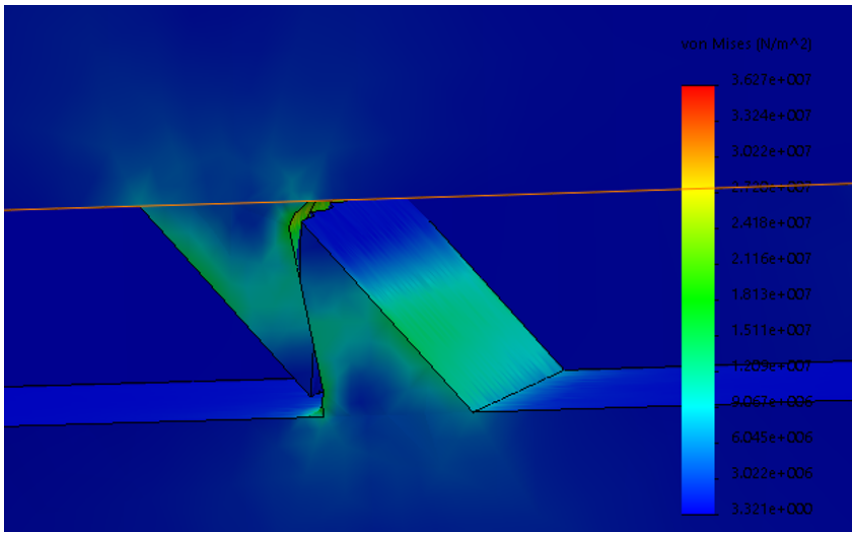

Figure 7.16: Simulation results: Maximum stress is 36.2 MPa.

As one can observe, the maximum stress is 36.2 MPa, meaning that the theoretical approach is more conservative as estimates a limiting stress of 290 MPa. The clutch dimensions are not reduced, as it could make the manufacturing process impossible or very difficult.

Furthermore, the mechanism responsible to (dis)engage the clutch is better seen in

figures 7.17 and 7.18.

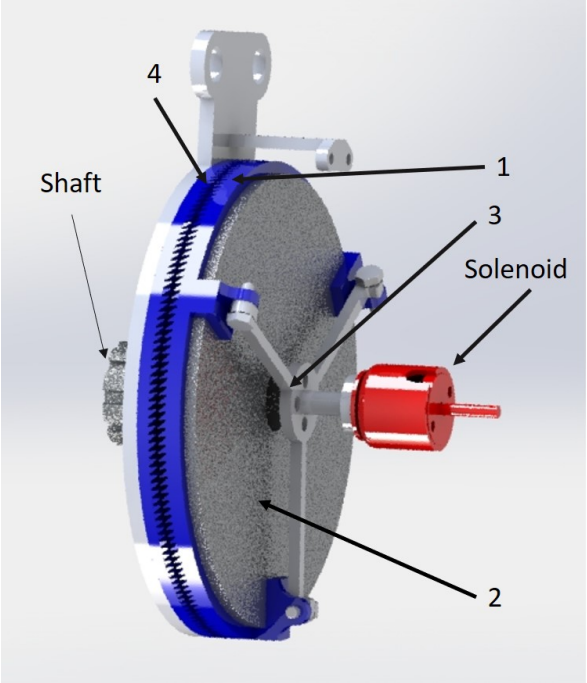

Figure 7.17: Clutch mechanism components.

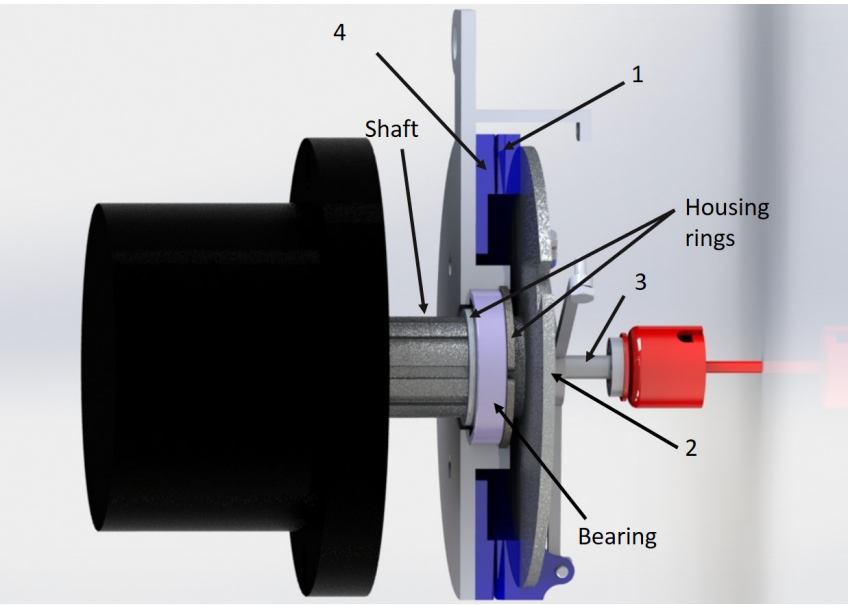

Figure 7.18: Clutch mechanism components.

In the figure, number 1 is the clutch plate that moves relatively to the homologous one (4), attached to the shank by means of an interface mechanism (not evaluated in this thesis). Component 2 is the base disk, attached to the damper, and the transmission of torque between the clutch and the damper is made by three boss extrusion in 1. Finally 3

is the connector element between the solenoid and the clutch and allows 1 to move when the solenoid is activated.

The clutch translation, in order to spare the use of linear bearings, is made through Aluminum-Aluminum contact so the tolerances of both 1 and 2 in the boss extrude and cut extrude, respectively, must not allow tightening contact, otherwise motion is impossible.

The clutch 4 is attached to a disk that must have the shank motion supported in the device shaft (figure 7.19). So, to allow relative motion between the shaft and the disk, a bearing must be used - see figure 7.18. As no meaningful loads are expected in both normal and radial directions, the smallest bearing to fit the shaft is selected. The one chosen was a capped, single row, deep groove ball bearing from SKF [39], whose specifications can be found in table 7.5.

Table 7.5: Shank Bearing.

d_{ber}	D_{ber}	B_{ber}	C_{ber}	C0	Pu	Kg
17 (mm)	26 (mm)	5 (mm)	2.03 (KN)	1.27 (KN)	0.054 (KN)	0,0075 (Kg)

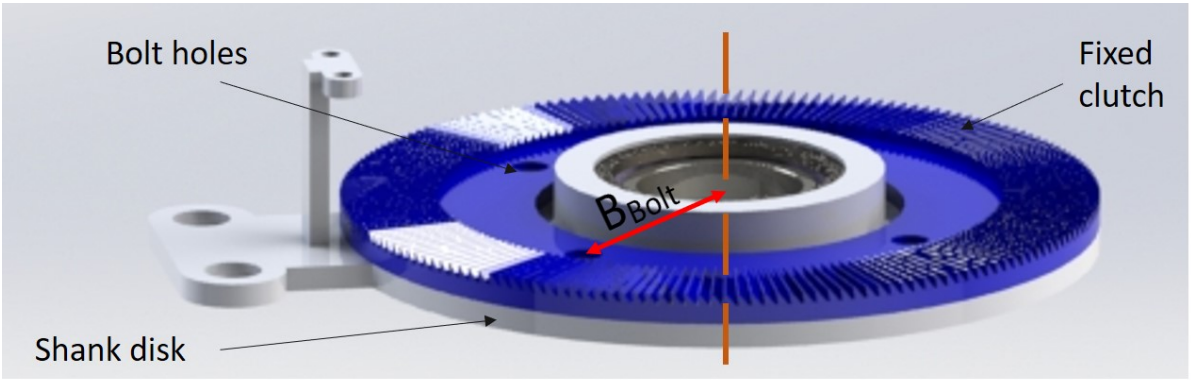

Figure 7.19: View of the fixed clutch, shank disk and the holes used to connect both. B_{Bolt} represents the distance from the holes to the center of rotation, represented by the orange intermittent line.

The connection between the clutch plate (4) and the shank disk (figure above) is made by bolts and nuts. However, to avoid bolts working in shear, such connection must be pre-tensioned allowing the torque to be transmitted between elements by friction only. Using the limiting torque of 54Nm defined in section 7.2, the tangential force caused by each bolt, F_{Fbolt}, is given by:

$$F_{Fbolt} = \frac{54}{n_{Bolt} * B_{bolt}} \tag{7.6}$$

where n_{Bolt} and B_{bolt} are respectively the number of bolts and the distance between them and the shaft's axis.

After defining the tangential force, the normal force (F_{Nbolt}) can be obtained considering a friction coefficient of 0.21 (Aluminum-Aluminum [4]). Moreover, the tension installed in the bolt (σ_{Bolt}) is simply obtained dividing F_{Nbolt} by the bolt resistance area, A_{Rbolt} - see equations bellow:

$$F_{Nbolt} = \frac{F_{Fbolt}}{\mu_{Al}} \tag{7.7}$$

$$\sigma_{Bolt} = \frac{F_{Nbolt}}{A_{Rbolt}} \tag{7.8}$$

$$A_{Rbolt} = \frac{\pi(D_{Bolt} - 0.935P_{Bolt})^2}{4} \tag{7.9}$$

The variables D_{Bolt} and P_{Bolt} refer to the bolt nominal diameter and pitch, respectively.

Finally, the torque provided to the bolt is expressed by:

$$M_{bolt} = 0.2 * D_{Bolt} * n_{Bolt} \tag{7.10}$$

The 0.2 coefficient can be found in [38] and is applied when not much information about the running conditions are known.

Using the set of equations described above, four M4 bolts of class 8.8 were chosen giving an installed tension of 305MPa in the bolt and a tightening torque of 2.14Nm. The safety coefficient, S_{Fbolt}, can be obtained knowing that the class 8.8 bolts have a yield strength of $0.8 * 800$MPa.

$$S_{Fbolt} = \frac{0.8 * 800}{305} = 2.1 \tag{7.11}$$

7.4 Encoder

An AKSIM™ absolute rotary encoder [36] (MBA7 with a MRA7D049AB025E00 ring) was selected, due to its high compactability. M2.5 fasteners are used to assembly

both moving parts of the encoder in the device. Figure 7.20, illustrates the encoder's 3D view and a technical drawing.

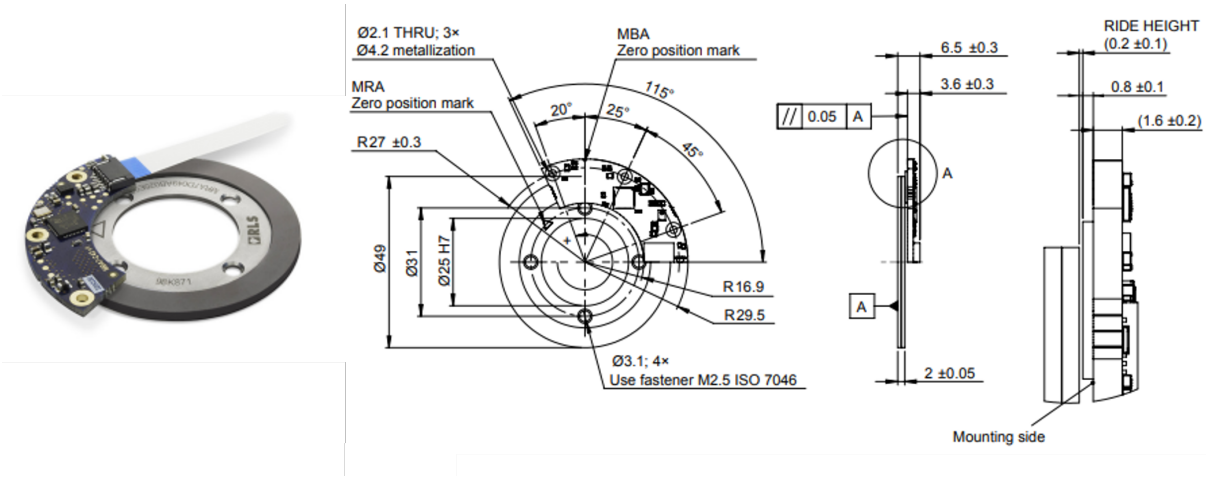

Figure 7.20: Encoder 3D view and technical drawing.

In the table 7.6 some of the encoders' properties can be seen.

Table 7.6: Encoder main properties.

Resolution	Supply Voltage	Current	Power	Mass
15 bits	4V	Max 150mA	0.6W	17.9g

7.5 Solenoid

To save as much energy as possible the solenoid must have a low power consumption, and, at the same time, low mass, a short activation time and a stroke greater that the clutch teeth height (2.5mm). Based on these constrains, a *Geeplus* Small Push-Pull Solenoid (size 141) with a stroke of 3mm was chosen [14]. The solenoid was desired to provide some force near the end of the stroke. So, a 25% duty cycle fits the application, having a power consumption of 5.33W, an input voltage of 6V (figure 7.22) and a response time of 9ms (figure 7.23).

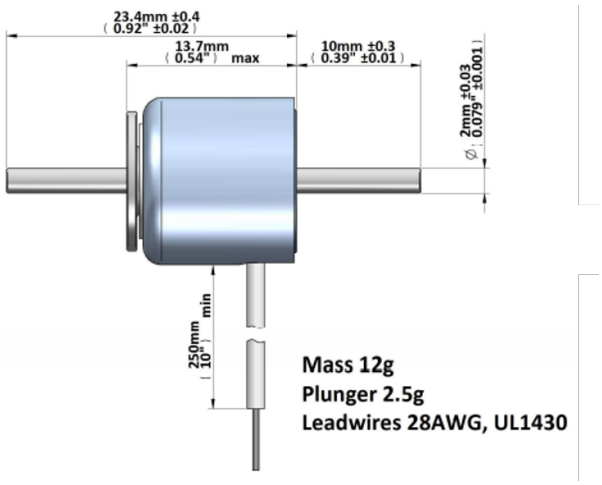

Figure 7.21: Solenoid draw indicating some relevant measures.

Data at 20°C , without heatsink

duty cycle = "on" time / "on" time + "off" time x 100%			100% cont.	50% or less	25% or less	10% or less
Max. "on" time in seconds			∞	100	36	7
watts at 20°C			1,33	2,66	5,32	13,3
ampere-turns at 20°			133	189	267	422
type no.	resistance Ω±10% (at 20°C)	number of turns	volts DC			
M141C-3V F141C-3V	6,5	330	3,0	4,2	6,0	9,5
M141C-6V F141C-6V	30	700	6,0	8,5	12	19
M141C-12V F141C-12V	97	1200	12	17	24	38
M141C-24V F141C-24V	468	2600	24	34	48	76

Figure 7.22: Solenoid electrical specifications.

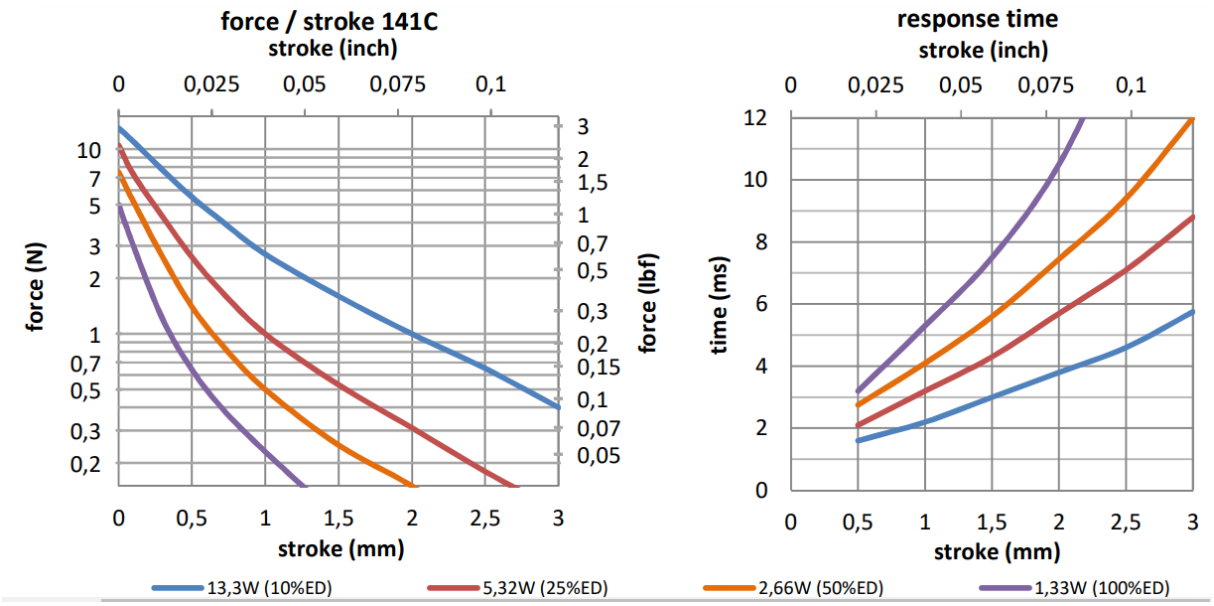

Figure 7.23: Solenoid Force and Response curves with respect to the moving distance and the Duty Cycle.

Table 7.7: Solenoid main properties.

Stroke	Supply Voltage	Power consumption	Activation Current	Mass
3mm	6V	5.3W	0.83A	14,5g

7.6 Battery

The battery must provide 6V and approximately 1A to activate the solenoid. So, a *lipo* battery with the characteristics given in table 7.8 was selected. [41]

Table 7.8: Battery main properties.

Voltage	Capacity	Discharge Rate	Mass	Dimensions
7.4V	450mAh	75c	28g	45*24*15mm

7.7 Microcontroller and electronic circuit

In relation to the microcontroller, an Arduino Nano®can be a first choice due to its small size, easiness to program and low power consumption. However, considering a future industrial application, other microcontroller should be selected, having more robust

connections and higher precision in real-time read/write functions, but still taking into account its power consumption.

This component is responsible to control the solenoid by receiving information from the encoder. The electric circuit is presented in figure 7.24, and includes the Arduino Nano®, the battery, the encoder, the solenoid, and additional electronic components. The blocks *VR 6* and *VR 4* represent DC voltage regulators of 6V and 4V, respectively. The *relay 1* is responsible for (de)activating the *relay 2* block [37], which switches its status every time it is activated, inverting the current direction in the solenoid, either from +6V to -6V or vice-versa. Consequently, the solenoid leads the clutch to engage or disengage. The diodes are a safety mechanism to protect the solenoid when the power is off, and hold 1A [8] which is higher than the 0.8A needed to activate the solenoid[14].

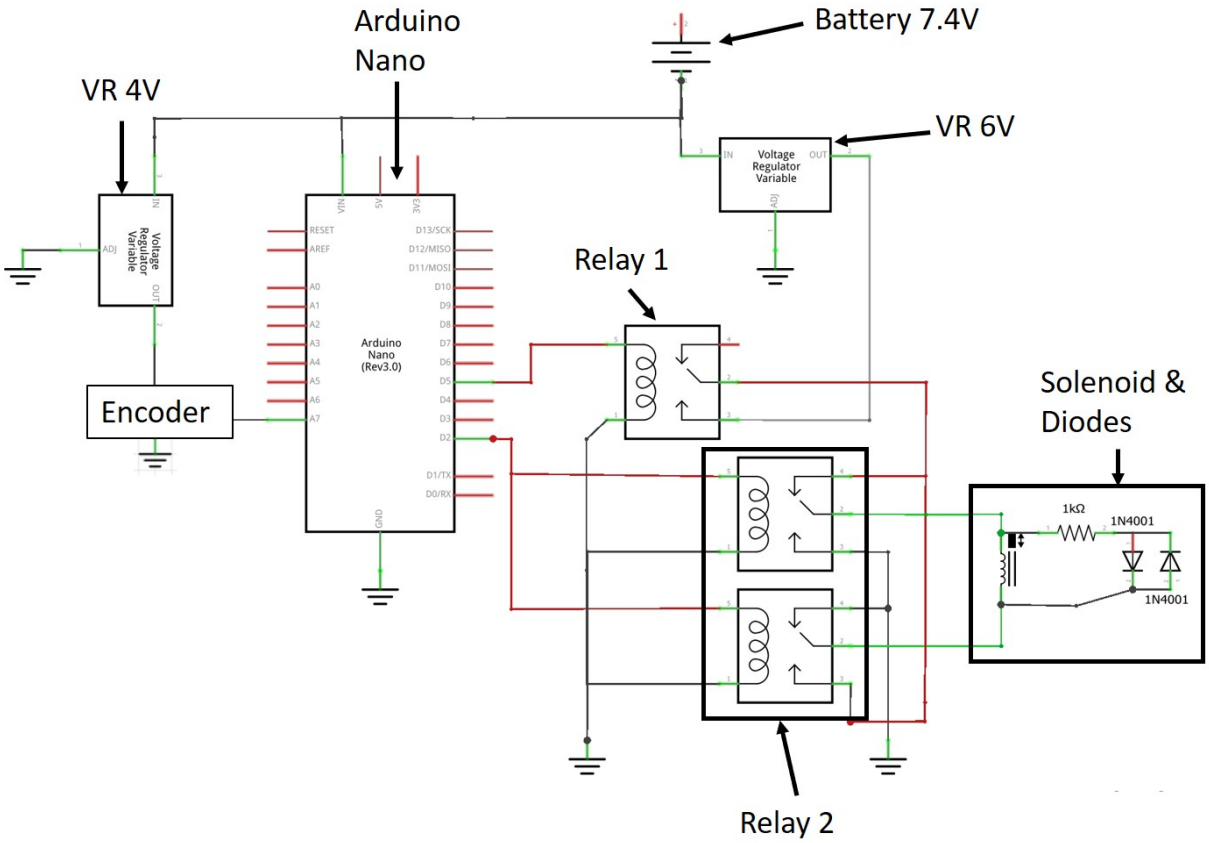

Figure 7.24: Electric circuit schema.

The maximum power drained from the battery accounts for the encoder (0.6W), solenoid (5.3W) and the relays (0.9W), giving a total of 6.8W.

7.8 State Machine

For the solenoid to be activated in the right moment, the information from the encoder is critical. In addition, an algorithm is also required that transforms the encoder data into a phase of the gait cycle. This transformation was done through a state machine. Only the algorithm is going to be explained, the actual implementation and real life test of this machine were not performed, although a simple simulation was done, which proved the desired behavior of such program.

The states are numbered from 0 to 6, being 0 the initial state, 1 the peak knee angle during loading phase, 2 the heel off, 3 the peak knee flection, 4 the solenoid firing, 5 the heel strike and 6 the solenoid power off. The connection between each state and their changing conditions (represented by letters from A to H), are shown in figure 7.25 and table 7.9, respectively.

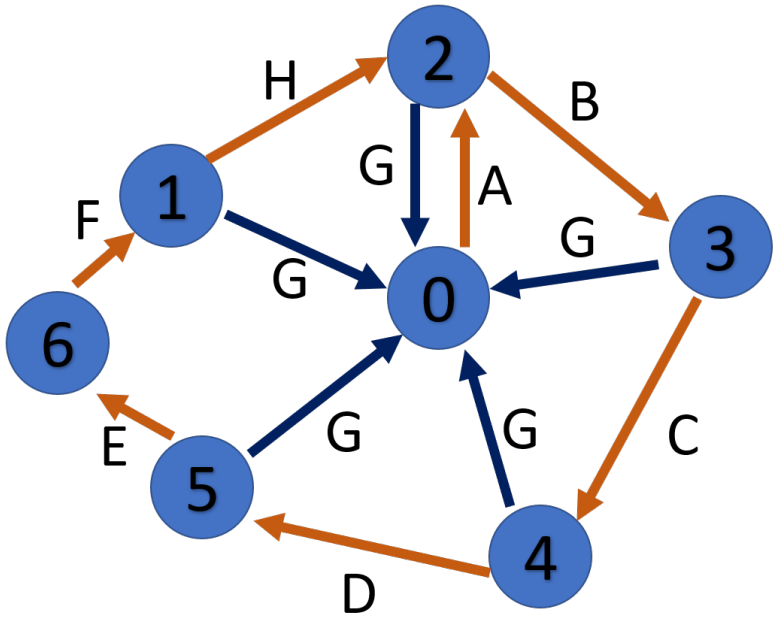

Figure 7.25: State machine indicating the connections (A to H) between the states (0 to 6).

Table 7.9: State transitions.

A	$\dot{\theta_{enc}} > 0$ AND $\theta_{enc} > \theta_{MAX}$
B	$\dot{\theta_{enc}} < 0$
C	$t_{act} < t_{cross}$
D	$\dot{\theta_{enc}} > 0$
E	$[\theta_k - \theta(t_{cross})] > Clutch_{Resolution}$
F	$\dot{\theta_{enc}} < 0$
G	$t_{state} > 1$
H	$\dot{\theta_{enc}} > 0$

$\dot{\theta_{enc}}$ and θ_{enc} represent, respectively, the angular velocity and the angle read from the encoder. θ_{MAX} is a threshold angle used to transit from the initial state to the state 2. t_{act} and t_{state} refer, respectively, to the activation time of the solenoid, 9 milliseconds, and the maximum time one state can be activated, serving as an exit condition of the system, and resetting it into the state zero. The t_{cross} is also an important function as it dictates the timing for the solenoid activation. Finally, θ_k and $Clutch_{Resolution}$ are, respectively, the knee angle at time sample, k, and the angular resolution of the clutch, 2°.

Following this, the state machine was implemented in *Matlab*® and a periodic generated knee pattern was fed into the algorithm in order to test if it was able to identify each phase correctly. The knee pattern generator results from a Fourier sum of 10 harmonics, using 10 *sin* and 10 *cosine* functions, whose amplitudes and frequencies are velocity dependent.

$$\theta(t) = \mu + \sum_{i=1}^{10} \left[\alpha_i * cos\left(\frac{2\pi i * t}{T}\right) + \beta_i * sin\left(\frac{2\pi i * t}{T}\right) \right] \tag{7.12}$$

Each of the parameters α_i, β_i, μ and T are related to the walking velocity through a linear regression, whose slope and interception for all 10 harmonics, i, can be seen in [29], giving a total of 44 coefficients. In the end, the walking velocity is the only parameter to chose as all the others are then automatically defined.

The angle pattern was sampled with a frequency of 1000Hz and then analyzed point by point from the beginning until the end. At each instance, k, a window of 5 points, going from time $k-4$ to k, is used to perform a linear regression between these five values. Although one is dealing with a continuous signal, in reality, not only noise might affect the data but also the output quantization from the encoder. The linearization tries to compensate this irregularities and also provides the slope of the regression, that can be

interpreted as the velocity in the instant k. This information was found useful to predict the solenoid activation time, that has to be made before the heel strike event, so that the engagement is faster and easier. Before the heel strike, extension is still on going, so, activating the solenoid will bring the teeth together but they will not engage as the direction of rotation is not appropriate. However, as flexion starts the teeth will rotate in the locking direction and eventually activate the damper. Thus, one can compensate the finite angular resolution and the possible problems of fail engagement at higher speeds. To do so, the calculated linear regression coefficients are used to compute the time at which that line intercepts the knee angle at heel strike. Firstly, such angle is assumed to be zero, but as the algorithm proceeds, it saves the angle from the transition 4 to 5 (heel strike). That calculated time is compared with the activation solenoid time, 9ms, and if lower, this element is fired.

A knee pattern based on a walking speed of 1m/s was generated and repeated 3 times, representing 3 steps. The resultant signal served as input to the state machine. The results are presented in figures 7.26 and 7.27

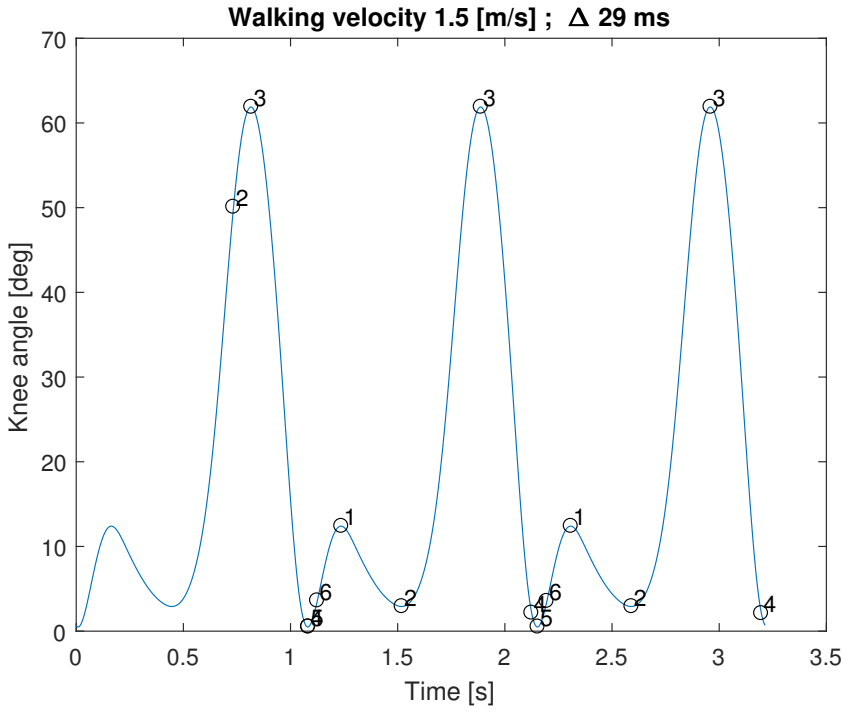

Figure 7.26: State machine result for the 3 gait cycles; Δ represents the time interval between the predicted heel strike and the actual event after the first step.

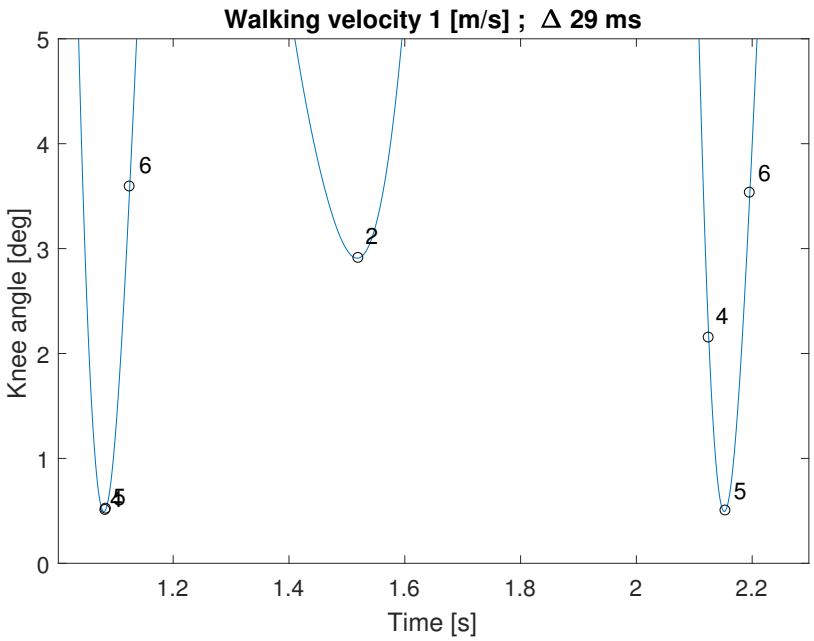

Figure 7.27: Zoom in of the previous figure in the region near the first and second heel strike.

As one can see, all the state transitions are identified by their respective number, except for the initial state (0). In the figure 7.27, it is visible the effect of the solenoid timing adjustment during the gait. At the first heel strike, θ_{cross} is zero, resulting in the almost coincidence between 4 and 5. However, after saving the actual angle at heel strike, the machine uses it as the new θ_{cross}, ending in a 29ms time delay between the same states. This delay is explicit in the second heel strike.

Still, 29ms is more than double the solenoid activation time, which should be the desired Δ value. Such a difference might be explained due to the parabolic behavior of the knee angle in late swing.[9]

Next, to test the reset condition, two gait cycles are separated by a zero angle that lasts 1.5 seconds, representing a stop in the gait - see figure 7.28.

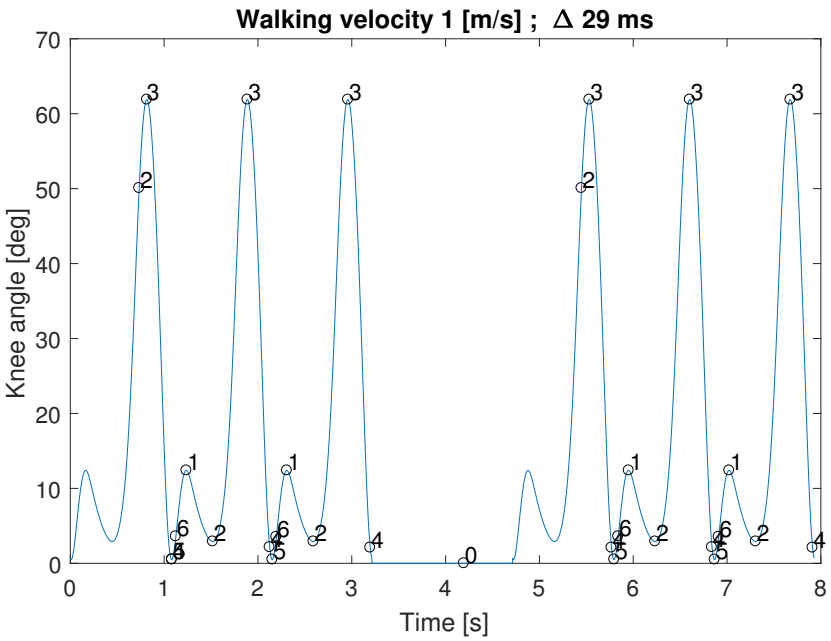

Figure 7.28: Interrupted gait cycle with the stages identified by the state machine.

The algorithm has correctly identified inactivity of the gait and reset the system.

Although the results are positive, the machine here presented should be improved in robustness. A real-time experiment must be made in order to properly verify the feasibility of the algorithm. Any significant disturbance or irregularity in the gait cycle could lead to states that do not correspond to the actual gait phase. Having this said, more robust, adaptive solutions exist in the state of the art, such as adaptive oscillators [22], although more computationally expensive.

7.9 Return Spring

7.9.1 Constant Damping Coefficient approximation

The spring must return the damper to its original position right before the next usage time. To do that, it is necessary to know the damping coefficient and then solve a simple differential equation where it only accounts for the the Damping coefficient and Spring stiffness, ignoring the inertial term as this is unknown. So, the system can thus be described by a first order differential equation, whose solution is a negative exponential function. K_{damp} must assume a value high enough to return the damper to its neutral position in a suited time interval.

The first order differential equations (ODE) is stated as follows:

$$J\ddot{\theta} + C_{ret}\dot{\theta} + K_{damp}\theta = T_{ext} \tag{7.13}$$

$$Letting \quad J \quad and \quad T_{ext} \quad be \quad zero \tag{7.14}$$

$$C\dot{\theta} + K_{damp}\theta = 0 \tag{7.15}$$

The solution for such ODE for an initial rotation of $(\theta(0))$ is:

$$\theta(t) = \theta(0) * e^{\left(\frac{-K_{damp} * t}{C_{ret}}\right)} \tag{7.16}$$

An artificial knee pattern generated through a fourier series [29], like the one performed in section 7.8 is used to obtain important information to solve equation 7.16. By setting a stride period of 810 milliseconds, that corresponds to a walking velocity of 1.5 m/s, is is observed a knee amplitude of 20° and a K1's duration time of 130 milliseconds. Leading to conclude that the reset time (T_{reset}), from the ending of K1 until the next heel strike, is:

$$T_{reset} = 810 - 130 = 680ms \tag{7.17}$$

The angle amplitude in the K1 area is about 20° so the damper must rotate that amount in the opposite direction within the reset time. To overestimate the spring rate, 25° will be used instead of the 20. As the time response of the first order system is asymptotic (to zero degrees) one will consider that the final position is 5 percent of the initial displacement. In other words, instead of the damper rotate 25° to its initial position, only $0.95 * 25°$ will be required. This 95% rotation takes exactly 3 constants of time, **T** which is defined as

$$T = \frac{C_{ret}}{K_{damp}} \tag{7.18}$$

One knows $3 * T$ must be equal to 680 ms and C_{ret} from the damper analysis, is equal to $4.4Nm.s/rad$. Such value is obtained by averaging the experimental data in the passive direction for zero tuns in the adjustment screw. The damper spring stiffness is then defined as:

$$K_{damp} = \frac{3 * C_{ret}}{680 * 10^{-3}} = 19.2567(Nm/rad) = 336.1(Nmm/^{\circ}) \tag{7.19}$$

The maximum torsional moment, T_{TorMax}, withstand by the spring, whose rate is $336Nmm/^{\circ}$, can be defined as:

$$T_{TorMax} = 0.336 * 25 = 8.4(Nm) \tag{7.20}$$

7.9.2 Solving the exact differential equation numerically

The proper evolution of the damping coefficient is an exponential type (section 7.2.1) in the form:

$$C = a * exp^{b*\theta} + c * exp^{d*\theta} \tag{7.21}$$

Thus the differential equation stated in 7.13 changes to:

$$(a * exp^{b*\dot{\theta}} + c * exp^{d*\dot{\theta}}) * \dot{\theta} + K_{damp}\theta = 0 \tag{7.22}$$

Such ODE is implicit so, to solve it, the *Matlab*® ode solver *ode15* was used. The solution for an initial displacement of 25° and initial velocity of -49°/*sec* is presented in figure 7.29. As for the initial velocity, *Matlab*® funtion *decic* was used to calculate a feasible value that solves the differential equation at time equals to zero.

The maximum return time of 680 *ms* is also represented, and, as one can see, the 5% of the initial displacement are reached before this time limit, proving that a spring stiffness of $336Nmm/^{\circ}$ is enough.

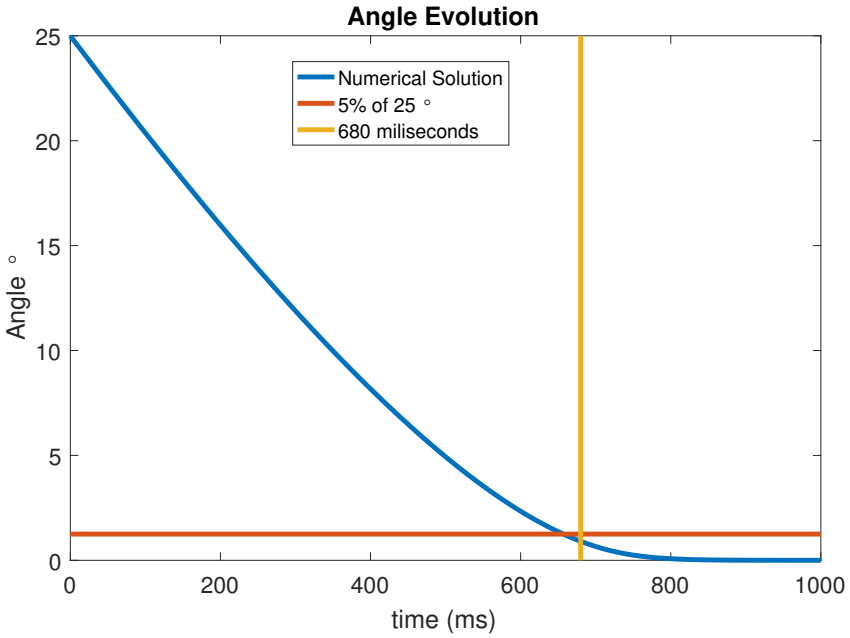

Figure 7.29: Solver solution.It is also marked the time stamp of 680 ms and the final position 1.25°.

7.9.3 Spring Selection

It was not found a commercial spring that fulfills the stiffness and maximum load requirements. So a custom spring solution was adopted and to do it, the following equations were used. [20]

$$K_{damp} = \frac{E_{spr} * d_{spr}^4}{3888 * D_{spr} * N_{tSpr}} \quad (Nm/deg) \tag{7.23}$$

$$S_{bending} = \frac{32 * T_{TorMax} * K_b}{d_{spr}^3 * \pi} \quad (MPa) \tag{7.24}$$

$$k_b = \frac{(4 * C^2 - C - 1)}{(4 * C * (C - 1))} \tag{7.25}$$

$$C = \frac{D_{spr}}{d_{spr}} \tag{7.26}$$

K_b is a stress concentration factor related to bending of curved beams. Other terms like, D_{spr}, d_{spr}, N_{tSpr}, E_{spr}, T_{TorMax}, K_{damp} and $S_{bending}$ represent respectively the spring mean diameter, wire diameter, number of turns, spring young Modulus, maximum torque, spring rate, and maximum bending stress. Setting Music wire (DIN-17223) as the spring material, which possesses an E of $210 GPa$ and, although the yield strength varies ac-

cording to the wire diameter this properties was set to 1700MPa, corresponding to a d_{spr} greater than 6mm. [25]

To restrain one degree of freedom the spring mean diameter, D_{str}, is set to 21mm. Knowing from above that T_{TorMax} is equal to 8.4Nm and R to $336 Nmm/deg$ the following system of equations was solved, to determine d, and N_t:

$$336 - \left(\frac{E * d_{spr}^4}{3888 * D_{spr} * N_t} \right) = 0 \tag{7.27}$$

$$1700 - \left(\frac{32 * T_{TorMax} * K_b}{d_{spr}^3 * \pi} \right) = 0 \tag{7.28}$$

$$k_b = \frac{(4 * C^2 - C - 1)}{(4 * C * (C - 1))} \tag{7.29}$$

$$C = \frac{D_{spr}}{d_{spr}} \tag{7.30}$$

Solving such system results on:

$$d_{spr} = 3.88(mm) \tag{7.31}$$

$$N_t = 1.73(turns) \tag{7.32}$$

As d_{spr} is actually lower than the assumed 6mm, and, knowing that the yield strength increases with the wire diameter reduction, one is actually on the safe side. Regarding the spring pitch, p_{spr}, this must be higher than the wire diameter so 4mm is chosen.

Figure 7.30 and 7.31 illustrate the CAD model of the spring as well the locking nuts used to hold it.

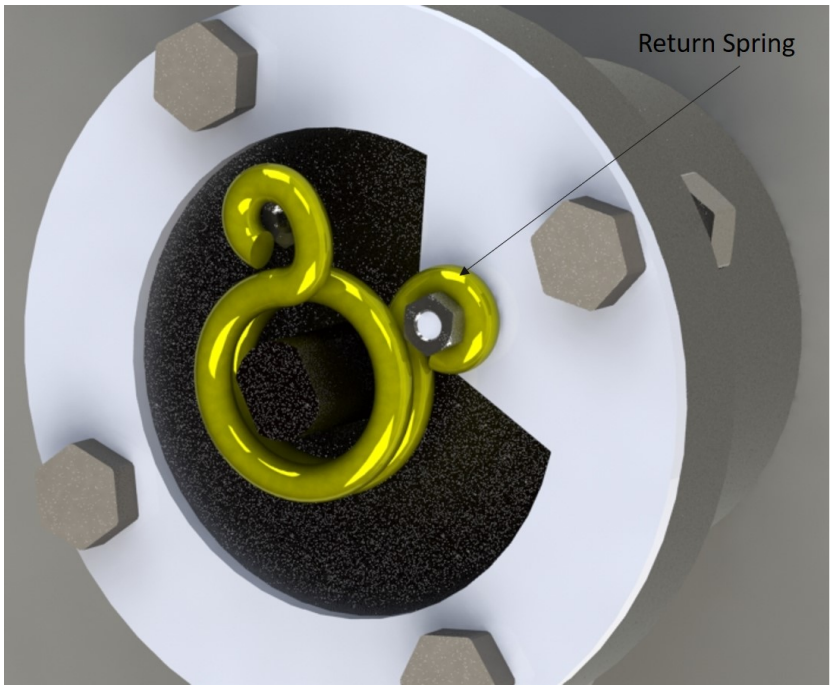

Figure 7.30: Spring geometry.

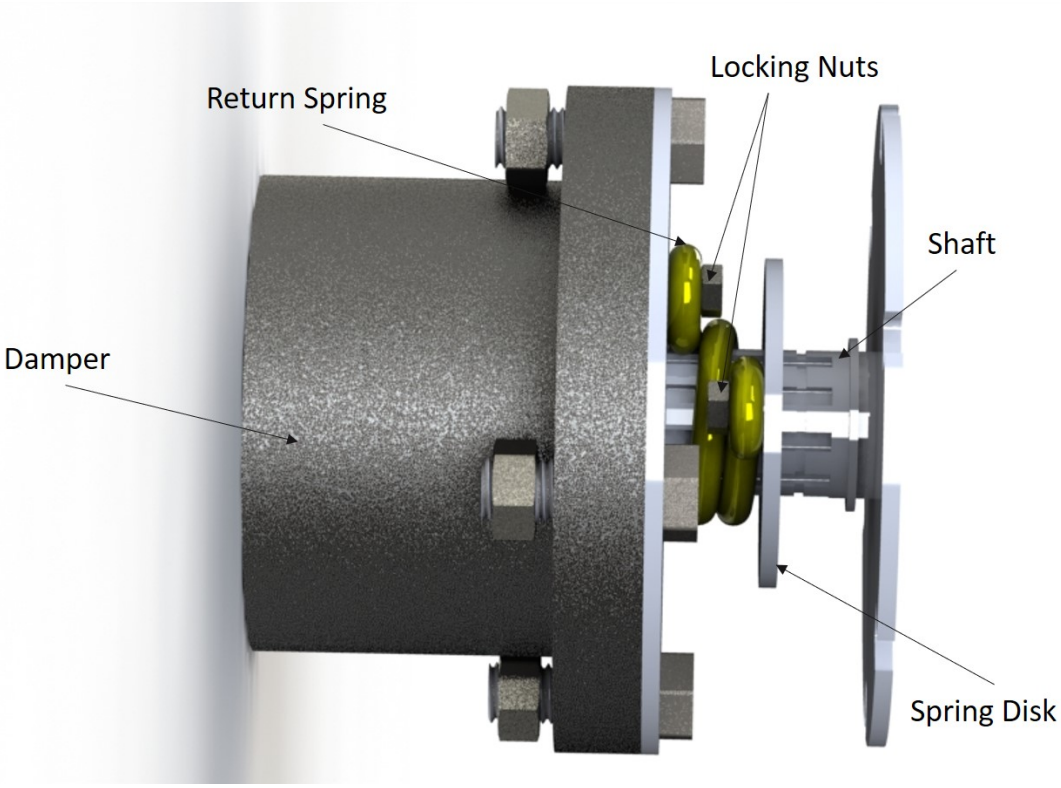

Figure 7.31: Spring locking nuts.

7.9.4 Spring effect

When the clutch is engaged not only the damper will resist motion but also the spring. So, to see the spring impact on the resisting moment, a comparison using only the damper and the damper in parallel with the spring is made (figure 7.32). The methodology used is similar to the one that produced figure 7.12, only now the spring effect are included.

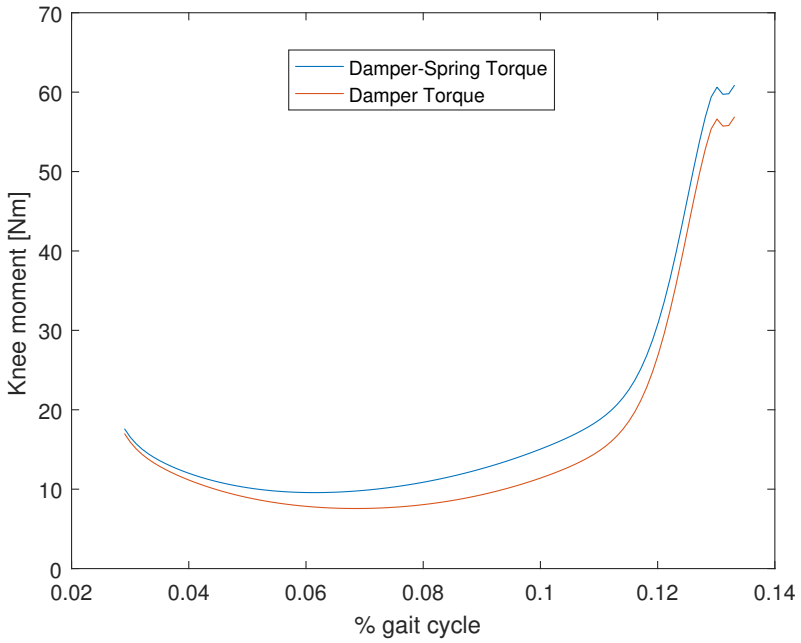

Figure 7.32: Comparison between the damper moment and damper-spring moment at a 1.5 m/s walking speed.

The parallel spring produces some changes into the device resisting moment although they are not drastic, proving that the damper plays the most significant role when dissipating energy.

7.10 Grooved Shaft

Power flows from the clutch mechanism to the damper through a shaft - see figure 7.31. This component must bear the maximum torque, 54 Nm. Regarding the dimensions, the outer diameter must be equal to the bearing inner one, so 17 mm, and the inner diameter is also limited by the damper small shaft, 10 mm, figure 7.30. Some grooves are necessary in order to lock the bearing by using housing rings, figure 7.18, however they are responsible for a torsion, bending and tension stress concentration, although torsion

is the only one that must be evaluated. The stress concentration factor, K_{ts} depends on the fillet radius of the groove,R^*, its depth, t and the outer shaft diameter, $D_{S,Out}$. These parameters are related to K_{ts} through the following equations. [35]

$$K_{ts} = C1 + C2 * \left(\frac{2*t}{D_{S,Out}}\right) + C3 * \left(\frac{2*t}{D_{S,Out}}\right)^2 + C4 * \left(\frac{2*t}{D_{S,Out}}\right)^3 \tag{7.33}$$

$$C1 = 1.089 + 0.924 * \sqrt{\left(\frac{t}{R^*}\right)} + 0.018 * \left(\frac{t}{R^*}\right) \tag{7.34}$$

$$C2 = -1.504 - 2.141 * \sqrt{\left(\frac{t}{R^*}\right)} - 0.047 * \left(\frac{t}{R^*}\right) \tag{7.35}$$

$$C3 = 2.486 + 2.289 * \sqrt{\left(\frac{t}{R^*}\right)} + 0.091 * \left(\frac{t}{R^*}\right) \tag{7.36}$$

$$C4 = -1.056 - 1.104 * \sqrt{\left(\frac{t}{R^*}\right)} - 0.059 * \left(\frac{t}{R^*}\right) \tag{7.37}$$

$$\tag{7.38}$$

The material considered is an aluminum of class 2024-T3, with $\sigma_{y,Al}$ of 345 MPa and a shear strength, $\tau_{y,Al}$ of 285 MPa. A DSH shaft ring (DIN 471) was chosen and its dimensions are shown in figure 7.33.

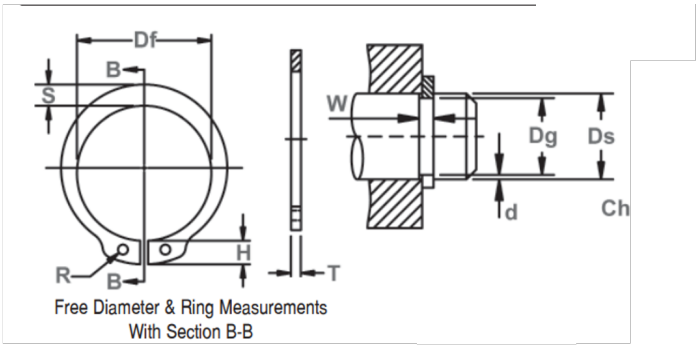

RING NO.	SHAFT DIA. (mm)	GROOVE SIZE				RING SIZE & WEIGHT								SUPPLEMENTARY DATA					
		DIAMETER		WIDTH	DEPTH	THICKNESS ***		FREE DIAMETER		LUG HT.	MAX. SEC.	HOLE DIA.	WEIGHT	EDGE MARGIN	THRUST LOAD Ring	THRUST LOAD Groove	Allow-able Rad/ Cham.	Max. Load w/Ch Max.	RPM Limits
	Ds	Dg	TOL.	W Min.	d	T	Tol.	Df	Tol.	H Max.	S Ref.	R Min.	kg/ 1000	Y Min.	Pr kN	Pg kN	R/Ch Max.	P'r kN	
DSH-16	16	15,2		1,10	0,40	1,00		14,7		3,7	2,2	1,7	0,700	1,2	7,40	3,2	1,0	2,40	45000
DSH-17	17	16,2		1,10	0,40	1,00		15,7		3,8	2,3	1,7	0,820	1,2	8,00	3,4	1,0	2,40	41000
DSH-18	18	17,0		1,30	0,50	1,20		16,5		3,9	2,4	2,0	1,110	1,5	17,00	4,5	1,5	3,75	39000

Figure 7.33: Outer Elastic ring and groove dimensions.

The fillet radius on the loading side must be less than 10 % of the ring thickness

(1mm). [35] In table 7.10 relevant dimensions and the calculated stress factor are presented.

Table 7.10: Relevant dimensions and stress concentration factor.

$D_{S,Out}$	17 [mm]
t	0.4 [mm]
R^*	0.1 [mm]
t/R^*	2
$t/D_{S,Out}$	0.0235
K_{ts}	2.744

The final shear stress and the safety coefficient can then be computed :

$$\tau_{nom} = \frac{16 * T_{max}}{\pi * (D_{S,Out} - 2 * t)^3} = 64.69 \quad [MPa] \tag{7.39}$$

$$\tau_{ins} = K_{ts} * \tau_{nom} = 177.5 \quad [MPa] \tag{7.40}$$

$$S_{f,sh} = \frac{\tau_{ins}}{\sigma_{y,Al}} = 1.6 \tag{7.41}$$

On the shaft there must be a way to transfer the rotational motion to the damper's return spring. Such communication is done by means of axial groves. Again, these groves are responsible for more stress concentrations. Using the same reference [35] equation 7.42 was used, based however, in the grove geometry presented in figure 7.34

$$K_{ts} = 6.083 - 14.775 * 10 * \left(\frac{R^{*2}}{D_{S,Out}}\right) + 18.25 * 10 * \left(\frac{R^{*2}}{D_{S,Out}}\right)^2 \tag{7.42}$$

R^{*2} and $D_{S,Out}$ represent respectively, based on figure 7.34, the parameters r and d.

Using the maximum ration, $\frac{R^{*2}}{D_{S,Out}} = 0.04$, covered by the empirical formula, 7.42, the geometrical parameters and stress values are found to be:

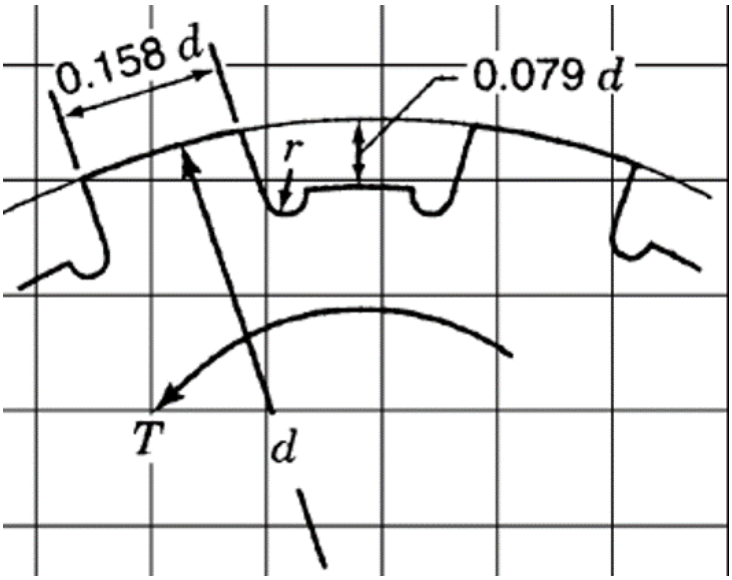

Figure 7.34: Outer Elastic ring and groove dimensions.

$$D_{S,Out} = 17 \ \ [mm] \tag{7.43}$$

$$R^{*2} = 0.68 \ \ [mm] \tag{7.44}$$

$$\tau_{nom} = \frac{16 * T_{max}}{\pi * (D_{S,Out})^3} = 55.96 \ \ [MPa] \tag{7.45}$$

$$K_{ts} = 3.09 \tag{7.46}$$

$$\tau_{ins,Es} = K_{ts} * \tau_{nom} = 173.14 \ \ [MPa] \tag{7.47}$$

$$S_{f,Es} = \frac{\tau_{ins}}{\sigma_{y,Al}} = 1.63 \tag{7.48}$$

Regarding the shaft, all the safety coefficients are around 1.6 so, one is on the safe side.

7.11 Shank connector stress analysis

Figure 7.35 illustrates the disk where one of the clutch's plate is attached to. This disk contains the connections for the shank interface piece (not designed) and so torque will flow through this component. The critical section is 20mm width and 2.5mm thickness. Considering that 54Nm are applied in this section, and the component's material is an aluminum allow of the class 2024-T3, with a $\sigma_{y,Al}$ of 345MPa, the maximum stress σ_{Scon} is calculated as follows:

$$\sigma_{Scon} = \frac{T_{max} * 10}{\frac{2.5 * 20^3}{12}} = 324MPa \tag{7.49}$$

$$Sf_{Scon} = 1.1 \tag{7.50}$$

As the safety coefficient is higher than 1, the component is on the safe side while in operation.

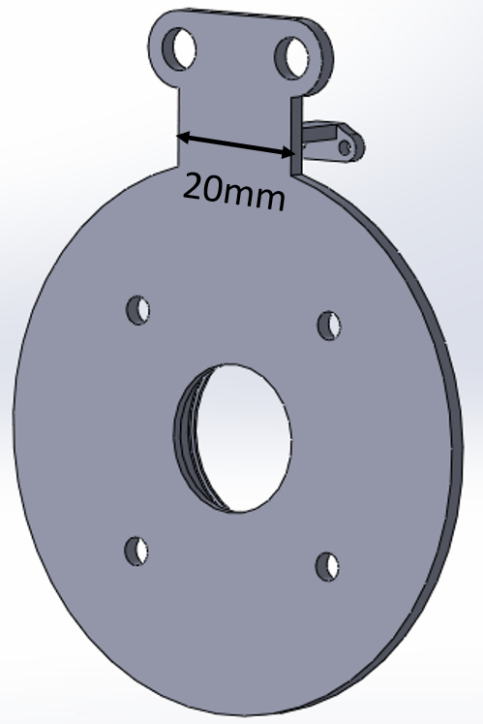

Figure 7.35: Outer Elastic ring and groove dimensions.

7.12 System weight and cost

System weight

As stated in the beginning, mass is an important requirement that must be evaluated. Table 7.11 describes the mass contribution of the several components.

Table 7.11: Weight of total system.

Component	**Mass (g)**
Damper	352
Encoder	17.9
Solenoid	14.5
Bearing	7.5
Nuts and Bolts	56.6
Battery	28
Components in aluminum alloy (AA2011 T3 and , AA2024 T3 2.78 g/cm^3, [1])	32.4
Components in magnesium alloy (AM60B, 1.74g/cm^3, [24])	38.5
Components in Steel (Music Wire, 7.86 g/cm^3, [20])	14.9
Total weight	**576.3**

The materials chosen were aluminum for the shaft and clutch plates, steel for the return spring and the other machined pieces are made in a magnesium alloy in order to reduce as much weight as possible. The magnesium used has a good toughness and machinability along side with a yield strength of 130 MPa. The first property is desirable to withstand impacts and the second one allows an easier manufacturing. [17]

In the end, the total weight of the system surpasses the stipulated limit of 500 grams, by 15%. This is a critical factor, as too much weight might increase the moment of inertia relatively to the hip, to the point where more energy is used to propel the leg forward than the one saved by the device.

System cost

Regarding the device monetary cost, only the electronic and damper parts were considered as it must be evaluated afterwards, if the other components are possible to be manufactured and through which process. Table 7.12 points out the cost of some components.

Table 7.12: Electronic components and damper costs.

Components	Price (€)	Power consumption (W)
Damper [44]	300	–
Solenoid [14]	3	5.3
Encoder [36]	75	0.6
Microcontroller [2]	22	–
Battery [41]	9	–
Relay [37]	1.5	0.9
diode [8]	12	–
Total	422.5	6.8

Note that the total power consumption (6.8W) in fact represents the maximum power drained from the battery and it occurs when the solenoid is activated. During the rest of the gait cycle, only the encoder is being powered, consuming 0.6W only. This last value is in the same order of magnitude than [9], whose power consumption was 0.86W. Regarding the device's price, this is incomplete as the parts production are unknown. Moreover, no reference devices were not found to compare prices, making it difficult to assess, whether the system is cheap or expensive.

7.13 Conclusions

This chapter presents a device that, from the mechanical point of view, is expected to work as proposed to, being the components safely sized and having a weight near the 500 grams limit. The electric components were chosen and an electric circuit was presented to control the solenoid action in the correct timing, although it needs an experimental verification. In terms of the algorithm developed, the state machine gives satisfactory results when tested with an artificial knee pattern, however, this does not exclude the need for a real-life test to tune the algorithm, if necessary. Finally, after performing the damper experiments, it was concluded that its use might change the normal knee pattern. Such conclusion arises because the torque provided by the apparatus is sometimes higher than the one produced by the activated muscles in the knee, during the loading response.

8. Conclusions and future work

This thesis formulates a first prototype for a wearable, damping-based mechanism intended to assist the knee during the loading phase of the human gait cycle. Two different solutions were thought and analyzed: a pneumatic solution, and another based on a commercial damper. Only the last one was further characterized given its higher envisioned potential.

The pneumatic solution was conceived to be adjustable to different walking speeds and body weights, by regulating its dissipation coefficient through a flow-control valve. A through-piston-rod pneumatic actuator with a chamber diameter of 30mm, 100mm stroke and an initial pressure of 6.9bar was selected, after performing some calculations. The system response to a kinematic pattern of the knee was simulated in *Simulink*, and it demonstrated that the concept should work, ideally. As the valve is tightened, the device would provide a moment close to that applied naturally by muscles in the knee, thus, reducing the person's effort. However, in reality, it was later realized that leaks of air could occur, which threaten the viability of such system. In addition, the required components comprising the system result in a heavier structure than desired for a wearable mechanism.

An alternative strategy was tried using a commercial rotary damper, which also affords customization, through a regulator screw that adjusts the damping coefficient. The rotary damper was selected considering its maximum holding torque and its damping coefficient. However, catalogued values of the last characteristics were found incomplete, so, experimental tests had to be performed. Those allowed a mathematical description of the apparatus, with the input being the angular speed and the restrictor turns, and the output, the damper torque. It was then concluded that the damper might modify the normal gait cycle. Nevertheless, experiments must be performed in the future, to assess if such modifications are significant and to measure the benefits (metabolic rate reduction) of using such device. Its success is highly dependent on the damper properties, on the clutch dis/engagement timing and, lastly, on the system weight. With the present work, it was already possible to reach a weight only 15% higher than the desirable limit (stipulated for 500g). Besides the damper study, a state machine was also developed capable of identifying some of the gait cycle events in order to properly de/activate the clutch. The algorithm is supposed to run only with the encoder information, and, although the simulations performed in Matlab were promising, a real-life experiment is crucial, as

noise and gait disturbances might affect the results.

For the future work, some changes in the design must be done, taking into account the manufacturing process and a weight reduction. Also both the shank and thigh interfaces have to be designed, otherwise no real experiments can be performed. Moreover, the concept here developed can be expanded to other regions of the gate cycle, like K3 and K4, however, a damper suitable for all these regions had to be found or custom-made. Most likely the damper characteristic had to be changed automatically throughout the gait, as different damping coefficients are required. Using such a strategy would require changes both in hardware (damper and other mechanical parts) and in software (state machine), whose robustness should be improved by using adaptive oscillator algorithms, for example. Finally, the last step is to have a modular device implemented in the hip, knee and ankle capable of dissipating some of the gait cycle energy, reducing even more the muscle activation and, so, the metabolic rate.

Bibliography

[1] Aalco. Aluminium alloy specifications - aalco. http://www.aalco.co.uk/datasheets/Aalco-Metals-Ltd_Aluminium-Alloy-Specifications_42.pdf.ashx. Accessed: 2018-06-8.

[2] Arduino. Arduino nano. https://store.arduino.cc/usa/arduino-nano. Accessed: 2018-07-15.

[3] Jonas Beil, Gernot Perner, and Tamim Asfour. Design and control of the lower limb exoskeleton kit-exo-1. In *Rehabilitation Robotics (ICORR), 2015 IEEE International Conference on*, pages 119–124. IEEE, 2015.

[4] Richard Gordon Budynas, J Keith Nisbett, et al. *Shigley's mechanical engineering design*, volume 8. McGraw-Hill New York, 2008.

[5] Steven H Collins, M Bruce Wiggin, and Gregory S Sawicki. Reducing the energy cost of human walking using an unpowered exoskeleton. *Nature*, 522(7555):212, 2015.

[6] Aaron M Dollar and Hugh Herr. Lower extremity exoskeletons and active orthoses: challenges and state-of-the-art. *IEEE Transactions on robotics*, 24(1):144–158, 2008.

[7] Native Dynamics. Discharge coefficient for nozzles and orifices. https://neutrium.net/fluid_flow/discharge-coefficient-for-nozzles-and-orifices/. Accessed: 2018-05-10.

[8] Jameco Eletronics. 1000 volt 1 amp silicon rectifier diode. https://www.jameco.com/z/1N4007-Major-Brands-1000-Volt-1-Amp-Silicon-Rectifier-Diode_36011.html. Accessed: 2018-07-15.

[9] Grant Elliott, Andrew Marecki, and Hugh Herr. Design of a clutch–spring knee exoskeleton for running. *Journal of Medical Devices*, 8(3):031002, 2014.

[10] Festo. Round cylinders dsnu/esnu. https://www.festo.com/cat/en-us_us/data/doc_enus/PDF/US/DSNU-ROUND_ENUS.PDF. Accessed: 2018-04-2.

[11] Festo. Threads in pneumatics. https://www.festo.com/wiki/en/Threads_in_pneumatics. Accessed: 2018-05-14.

[12] Festo. Valve festo. https://www.festo.com/net/SupportPortal/Files/17267. Accessed: 2018-07-15.

[13] Futek. Futek model tff400. http://www.futek.com/files/pdf/Product%20Drawings/tff400.pdf. Accessed: 2018-05-8.

[14] Geeplus. Products / push/pull solenoids. https://www.geeplus.biz/push_pull_solenoids.htm. Accessed: 2018-05-13.

[15] Alena M Grabowski and Hugh M Herr. Leg exoskeleton reduces the metabolic cost of human hopping. *Journal of Applied Physiology*, 107(3):670–678, 2009.

[16] Hugh Herr. Exoskeletons and orthoses: classification, design challenges and future directions. *Journal of neuroengineering and rehabilitation*, 6(1):21, 2009.

[17] ASM International. Introduction to magnesium alloys. https://www.asminternational.org/documents/10192/22833166/Z05920L_SampleChapter.pdf/ee7dd6d0-91f9-de44-fb1f-97fe969bf5f5. Accessed: 2018-06-15.

[18] W Knight. The exoskeletons are coming, 2015.

[19] L Lamoreux and M Eng. Uc-bl pneumatic swing-control unit for above-knee prostheses. *Bulletin of Prosthetics Research*, 1968.

[20] Leespring. Torsional springs. http://springipedia.com/torsion-design-theory.asp. Accessed: 2018-06-4.

[21] Jennifer L Lelas, Gregory J Merriman, Patrick O Riley, and D Casey Kerrigan. Predicting peak kinematic and kinetic parameters from gait speed. *Gait & posture*, 17(2):106–112, 2003.

[22] CS Lintzen, J van den Kieboom, R Ronsse, W van Dijk, H van der Kooij, and AJ Ijspeert. *Oscillator-based walking assistance: Optimization & validation Part I: Optimization by simulations*. PhD thesis, Citeseer, 2011.

[23] Bobby Marinov. Types And Classifications of Exoskeletons. https://exoskeletonreport.com/2015/08/types-and-classifications-of-exoskeletons/. Accessed: 2018-02-28.

[24] AZO Materials. Magnesium am60b cast alloy (m10602). https://www.azom.com/article.aspx?ArticleID=9237. Accessed: 2018-06-15.

[25] Matweb. Astm a228 steel (uns k08500). http://www.matweb.com/search/datasheet.aspx?matguid=4bcaab41d4eb43b3824d9de31c2c6849&ckck=1. Accessed: 2018-06-5.

[26] Maxon. Maxon dc motors. https://www.maxonmotor.com/maxon/view/content/Overview-brushless-DC-motors. Accessed: 2018-05-8.

[27] Grzegorz Mikułowski and Rafał Wiszowaty. Pneumatic adaptive absorber: mathematical modelling with experimental verification. *Mathematical Problems in Engineering*, 2016, 2016.

[28] Grzegorz Mikułowski, Rafał Wiszowaty, and Jan Holnicki-Szulc. Characterization of a piezoelectric valve for an adaptive pneumatic shock absorber. *Smart Materials and Structures*, 22(12):125011, 2013.

[29] Vito Monaco, Giuseppe Galardi, Martina Coscia, Dario Martelli, and Silvestro Micera. Design and evaluation of neurobike: a neurorehabilitative platform for bedridden post-stroke patients. *IEEE Transactions on Neural Systems and Rehabilitation Engineering*, 20(6):845–852, 2012.

[30] Vito Monaco and Silvestro Micera. Age-related neuromuscular adaptation does not affect the mechanical efficiency of lower limbs during walking. *Gait & posture*, 36(3):350–355, 2012.

[31] U.S. Department of Defense. *Technology Readiness Assessment (TRA) Guidance.* 2011. https://www.army.mil/e2/c/downloads/404585.pdf.

[32] Ossur. Ct knee braces. https://assets.ossur.com/library/38478/CTi20Brochure.pdf/. Accessed: 2018-07-15.

[33] ottobock. Knee/leg. https://www.ottobock.com.au/orthotics/affected-body-regions/knee-leg/. Accessed: 2018-07-15.

[34] Jacquelin Perry, Jon R Davids, et al. Gait analysis: normal and pathological function. *Journal of Pediatric Orthopaedics*, 12(6):815, 1992.

[35] Walter D Pilkey and Deborah F Pilkey. *Peterson's stress concentration factors*. John Wiley & Sons, 2008.

[36] RLS. Absolute rotary encoder. https://www.rls.si/en/products/rotary-magnetic-encoders/aksim-rotary-absolute-encoder-module. Accessed: 2018-07-15.

[37] RS. Omron spdt non-latching relay pcb mount, 3v dc coil, 2 a. https://uk.rs-online.com/web/p/non-latching-relays/6839258/. Accessed: 2018-07-15.

[38] Joseph Edward Shigley. *Shigley's mechanical engineering design*. Tata McGraw-Hill Education, 2011.

[39] SKF. Skf rolling bear. http://www.skf.com/binary/77-121486/SKF-rolling-bearings-catalogue.pdf. Accessed: 2018-05-20.

[40] Streifeneder. The eight phases of human gait cycle. https://www.streifeneder.com/downloads/o.p./400w43_e_poster_gangphasen_druck.pdf. Accessed: 2018-04-10.

[41] Tattu. Tattu 450mah 2s1p 75c 7.4v lipo battery pack. http://www.gensace.de/tattu-450mah-2s-75c-lipo-battery-pack.html. Accessed: 2018-05-30.

[42] Andrew Valiente. Design of a quasi-passive parallel leg exoskeleton to augment load carrying for walking. Technical report, MASSACHUSETTS INST OF TECH CAMBRIDGE MEDIA LAB, 2005.

[43] Wietse van Dijk and Herman Van der Kooij. Xped2: A passive exoskeleton with artificial tendons. *IEEE robotics & automation magazine*, 21(4):56–61, 2014.

[44] Weforma. Rotary dampers with high torque range. http://www.weforma.com/fileadmin/pdf/Datenblaetter/2015/Rotationsdaempfer/Weforma_WRD-H-02_en.pdf. Accessed: 2018-04-29.

[45] Bruce Wiggin, Steven H Collins, and Gregory S Sawicki. A passive-elastic ankle exoskeleton using controlled energy storage and release. *American Society of Biomechanics*, 2010.

[46] M Bruce Wiggin, Gregory S Sawicki, and Steven H Collins. An exoskeleton using controlled energy storage and release to aid ankle propulsion. In *Rehabilitation Robotics (ICORR), 2011 IEEE International Conference on*, pages 1–5. IEEE, 2011.

[47] David A Winter. Biomechanical motor patterns in normal walking. *Journal of motor behavior*, 15(4):302–330, 1983.

[48] David A Winter. *Biomechanics and motor control of human movement*. John Wiley & Sons, 1990. https://isbweb.org/data/, Accessed: 2018-03-2.

9. Appendix A

Table 9.1: Results for the damping test with a quarter turn on the restrictor. V_{out}, T_{sens}, C_{damp} are respectively the motor output velocity, the torque obtained by the sensor, and the computed damping coefficient for each output velocity.

Target Speed $[^\circ/s]$	$N_t = 1/4$					
	Active Direction			Free Direction		
	V_{out} $[^\circ/s]$	T_{sens} $[Nm]$	C_{damp} $\left[\frac{Nm*s}{rad}\right]$	V_{out} $[^\circ/s]$	T_{sens} $[Nm]$	C_{damp} $\left[\frac{Nm*s}{rad}\right]$
10	9.73	7.71	43.99	9.91	1.47	8.38
20	19.93	11.26	32.46	19.94	2.37	6.99
30	30.94	13.34	25.23	30.02	3.00	5.87
50	51.04	16.51	19.07	51.00	3.98	4.85
75	74.76	20.15	15.14	74.32	5.08	3.91
100	99.00	21.25	12.30	100,09	6.29	3.60
150	149.42	25.96	9.96	149.84	7.57	2.90
200	202.43	25.73	7.28	203,57	8.35	2.35
300	223.09	32.56	8.36	302.56	10.79	1.93

Table 9.2: Results for the damping test with half a turn on the restrictor. V_{out}, T_{sens}, C_{damp} are respectively the motor output velocity, the torque obtained by the sensor, and the computed damping coefficient for each output velocity.

Target Speed $[°/s]$	$N_t = 1/2$					
	Active Direction			Free Direction		
	V_{out} $[°/s]$	T_{sens} $[Nm]$	C_{damp} $\left[\frac{Nm*s}{rad}\right]$	V_{out} $[°/s]$	T_{sens} $[Nm]$	C_{damp} $\left[\frac{Nm*s}{rad}\right]$
10	9.69	10.60	60.71	9.98	1.50	8.58
20	19.78	15.46	43.63	19.95	2.35	6.84
30	30.21	18.48	35.43	30.02	2.98	5.80
50	51.12	23.88	27.21	50.41	4.10	4.78
75	74.32	28.87	21.78	74.1	5.40	3.85
100	99.30	31.73	18.05	101.04	6.54	3.49
150	147.49	32.78	12.50	149.77	8.19	3.02
200	201.77	30.00	8.17	202,19	9.18	2.62
300	224.48	29.01	7.25	302.45	9.62	1.91

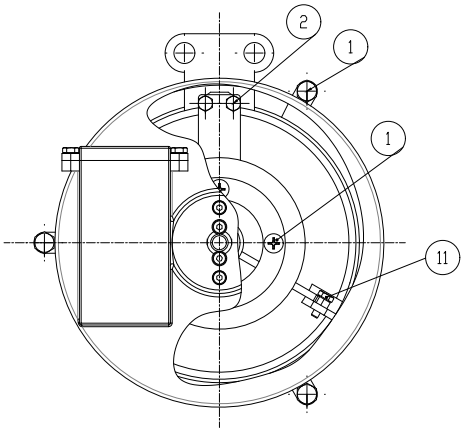

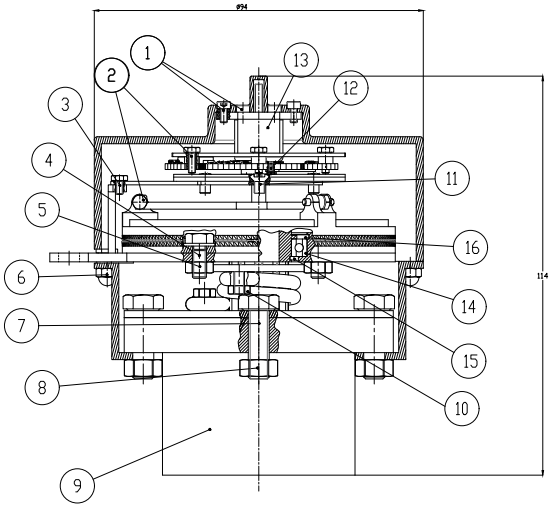

ITEM NO.	PART NUMBER	DESCRIPTION	QTY.
1	Bolt cilindrical head with hex hole	ISO 4762 - M2X4 - 3.6	4
2	Bolt with hex head	ISO 8876 - M2X6 - 3.6	6
3	Bolt with hex head	ISO 8876 - M2X4 - 3.6	2
4	Bolt with hex head	ISO 8876 - M4X10 - 8.8	4
5	Nut with hex head	ISO 4032 - M4-6	4
6	Blind Nut	DIN 1587 - M3 - 6	3
7	Bolt with hex head	ISO 8876 - M6X20 - 3.6	4
8	Nut with hex head	ISO 4032 - M6-6	4
9	Damper		1
10	Nut with hex head	ISO 4032 - M3-6	2
11	Bolt with cilndrical head	ISO 7048 - M3X5 - 3.6 - H	3
12	Bolt with cilndrical head	ISO 7048 - M1.2X3 - 3.6 - H	4
13	Solenoid		1
14	SKF single groove ball bearing	61803	1
15	Inner housing ring	DIN 471	1
16	Exterior housing ring	DIN 472	1
17	Bolt with hex head	ISO 8876 - M3X6 - 3.6	3

Figure 9.1: 2D drawin of the system

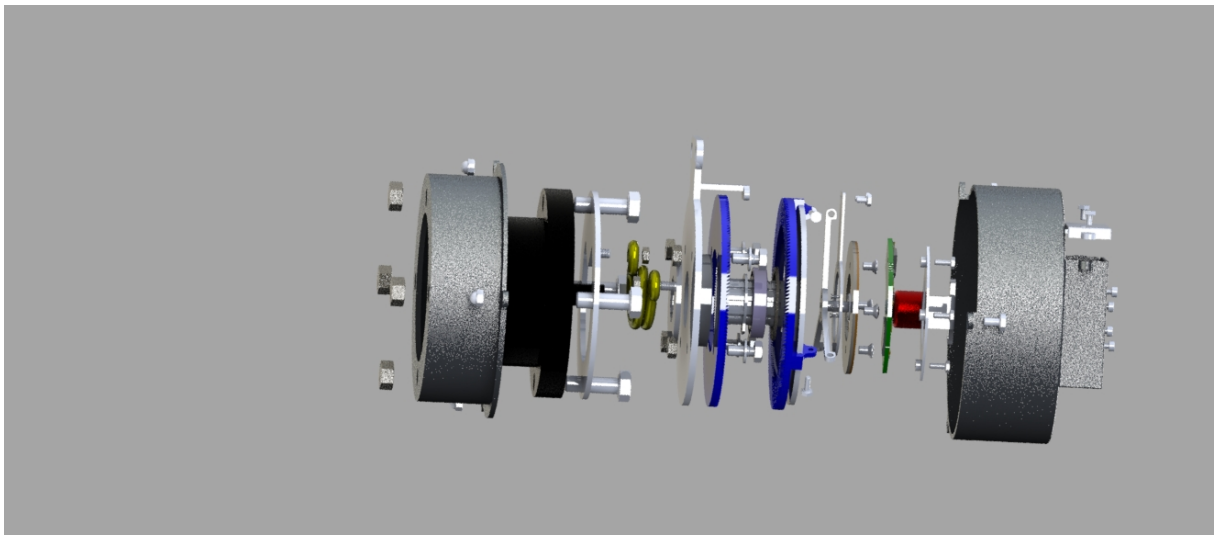

Figure 9.2: Exploded view of the device

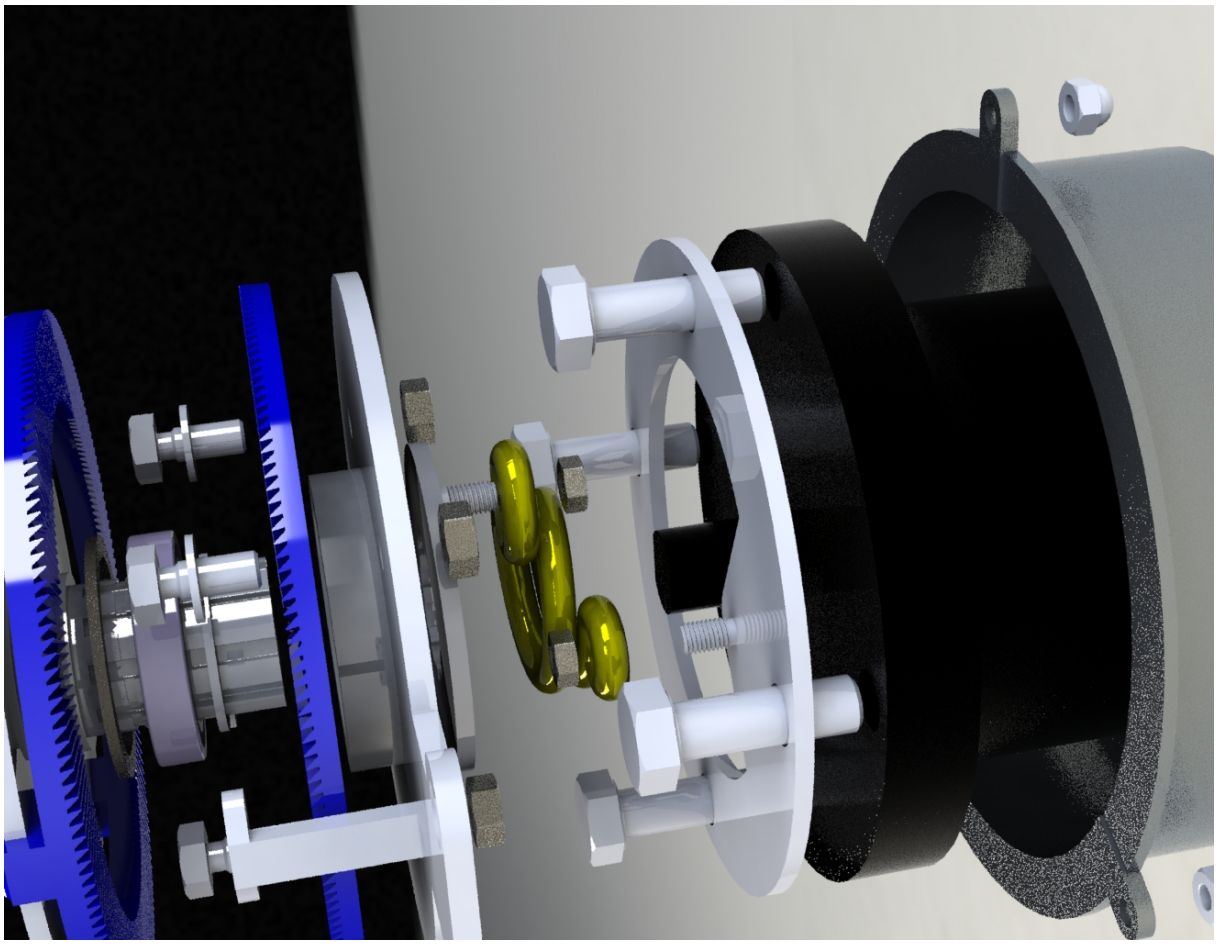

Figure 9.3: Exploded view: closer look to the spring area

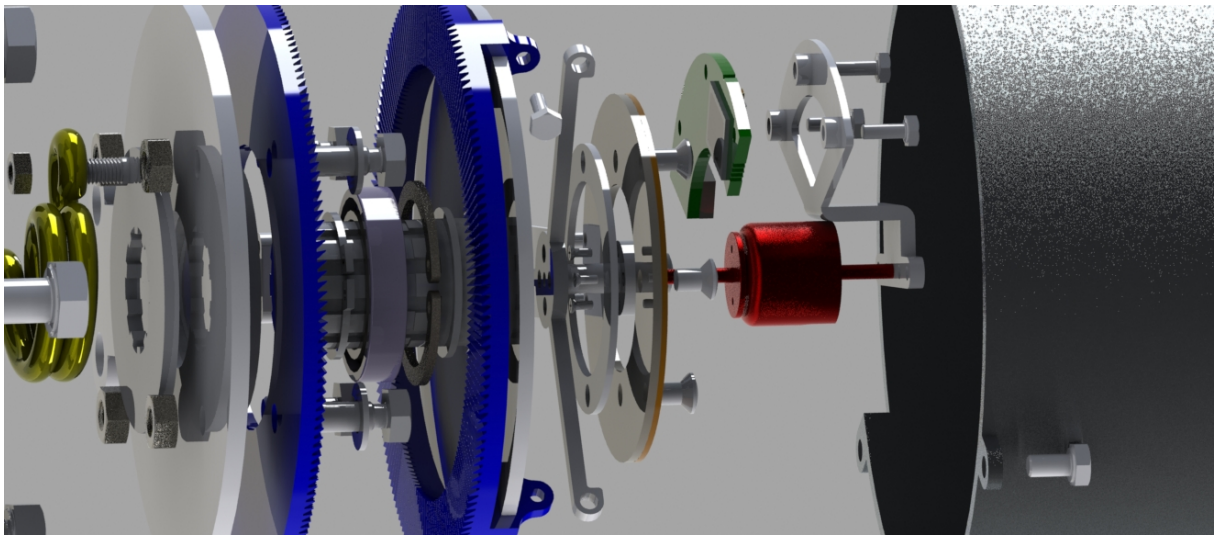

Figure 9.4: Exploded view: closer look to the solenoid area